Analysis and Modeling of Seismic Ground Motions in Heterogeneous Structures in Southern California

Thesis by

Craig W. Scrivner

In Partial Fulfillment of the Requirements

for the Degree of

Doctor of Philosophy

Caltech

Pasadena, California

1998

(Submitted August 4, 1997)

Acknowledgements

I have too many people to acknowledge to mention them all here.

There are a few people in high school and college who had a particularly significant effect on me and the direction of my studies. In high school, Richard McCown, Tom Perkins, and Alice Hahn taught the classes and ran the clubs that I enjoyed, rather than suffered through. At Deep Springs College, Malcolm Watley and Peter Rolnick passed on their enthusiasm for physics and mathematics, when the rest of the curriculum might have turned me to liberal arts forever. Geoff Pope gave me an incredible opportunity to work up in the mountains for a couple summers and he and Iris have put up with my yearly visits to rehash old times and catch up on the school and their lives.

At Caltech, I first thank Don Helmberger for providing his advice throughout my thesis work. He suggested projects and provided help on my research, but he also had the patience to let me make my own way, though it was often slow.

When I arrived at Caltech, I wasn't receiving my stipend but was too confused to know what to do about it. Cheryl Contopulos got my pay started and responded to an untold number of other questions and requests that I have had while in the Seismo Lab. The Caltech bureaucracy isn't too thick to begin with, but it is paper thin when Cheryl is helping out. In addition to all this, she has been a terrific friend with a lot of interest in and knowledge of places to go camping, hiking, backpacking, and (most recently) rafting in the Southwest.

A lot of what I learned and a lot of the fun that I had at Caltech was due to the other students in the Seismo Lab and the Division. Every student I've asked questions of has made time to answer me. I hope I've provided my share of help in return. Inevitably I will fail to mention someone who deserves recognition, but some previous students that I particularly want to thank include Cathy Smither, Doug Dreger, Linda Rowan, Dave Wald, Hong Kie Thio, Paul Tackley, and Sharon Kedar.

iv

Officemates make grad student life fun (or at least interesting), and I've had a number of them. Thanks to Monica Kohler, Kuo Fong Ma, Xiaodong Song, Shingo Watada, Brad Woods, Xi Song, Stacey Kittner, Jascha Polet, Leo Eisner, and Blair Zajac for good conversations and help.

I'd also like to thank my housemates. The Shack was a memorable venue. I'm glad I got out before the termites brought it down on my head or I caught the Hanta virus, but it was fun living with Cathy Smither and Clint the Talkative Cat. The new house doesn't have as much "character", but Liz and John Holt are fun to hang out with, and John's ever-expanding garden is a wonder in its own right. The amazing power of compost.

In the past few years I got back into running a lot of miles, and want to thank my running partners Wohjer Lee, Doug Yule, and Tim 'Dirt' Melbourne for keeping me at it. Wohjer got me back into running, Doug suggested I join Team Blarney, and Tim complained that his calves hurt whenever he ran on pavement.

Finally, I thank my family for their support throughout my education. They didn't necessarily know what I was doing or why, and most likely my parents cringed when I set aside my engineering degree to pursue seismology, but they have always provided their support. It has been terrific to be so close to them while at Caltech. Thanks Susan, Robin, Aldo, Jennifer, Nicholas, and Jacqueline, and, of course, Mom and Dad.

Abstract

This thesis contains studies of seismic data from the 1995-1996 Ridgecrest earthquake sequence, an aftershock of the 1987 Whittier Narrows earthquake and the 1991 Sierra Madre mainshock, and aftershocks of the 1994 Northridge earthquake. The Ridgecrest data set spans southern California, including stations in the Los Angeles area basins. The Whittier Narrows/Sierra Madre and Northridge data sets consist of stations in the Los Angeles and San Fernando Valleys, respectively, and record earthquakes occurring directly adjacent to these sedimentary basins. The studies examine the variability of ground motions in the crust and details of seismic propagation from the crust into sedimentary basins. In the Ridgecrest study, amplitudes of synthetic waveforms from a 1D model are compared with data amplitudes at rock, soil, and basin sites. At rock sites, the data amplitudes are within a factor of 2 of the synthetic amplitudes. At basin and soil sites, the data are within a factor of 3 of the synthetic amplitudes. Stations beyond the trailing edge of sedimentary basins are affected by leaked basin surface waves. In the Whittier Narrows/Sierra Madre study, waveform phases generated by the edge of the Los Angeles basin are identified and modeled with a 2D structure. In the data, multiples of the direct shear wave, reflected from the surface and turned by the basin edge, are up to two times the amplitude of the direct arrival. A simple, smooth, 2D basin edge model produces the correct timing and relative amplitude of basin-trapped phases. In the Northridge study, we contrast waveforms from a shallow and a deep event. The waveforms from the shallow event include basin-generated surface waves in the basin, and a phase-shift in the direct shear wave outside the basin. A model with a strong velocity contrast at about 1 km depth in the upper basin, a depth for the entire basin just above the shallow source depth, and a gradient beneath the basin produces synthetic waveforms that match the distinctive features in the data set.

Contents

List of Figures

List of Tables

Chapter 1
Introduction

1.1 General Introduction

Sediment-filled vallies, hereafter referred to as sedimentary basins, or just basins, play a significant role in the seismic hazard of a number of cities worldwide. Examples of earthquakes in which basin response caused damage include the 1985 Michoacan earthquake, which caused catastrophic damage in Mexico City, the 1989 Loma Prieta earthquake, which caused extensive damage in the Marina District of San Francisco, the 1994 Northridge earthquake which caused damage in the San Fernando and Los Angeles Valleys of Los Angeles, and the 1995 Hyogo Ken Nanbu earthquake which caused heavy damage and fires in the densely populated city of Kobe. In the first two examples, the earthquakes were many kilometers from the damage sites mentioned. In the latter two examples, the earthquakes were next to or under the basin.

Sedimentary basins trap seismic energy and focus it within the basin. Often the basins are capped by soft, unconsolidated soils of varying thickness. As a result, basins cause increased ground motion amplitudes and prolong shaking, but the effect is quite variable from point to point in a basin, and from basin to basin.

The seismic response of basins can be broken down into the effects of the background crust, of the deep basin, of micro-basins near the surface, and of soil site response. As the size of models increases to incorporate sets of basins and the crustal path from more distant sources, the interplay of the background crustal structure with the basins becomes more important. And as higher frequencies are calculated in simulations, the basin structures and shallow soils characteristics must be known in more detail.

If an earthquake is relatively far from a basin, then the crustal structure will affect

the energy that strikes the basin and affect the basin response. At sufficiently large distances, critical reflections off of the Moho (S_mS) are larger than the direct shear wave and slow the attenuation of peak amplitudes (Somerville *et al.*, 1994). As a result, S_mS may generate a large response in a basin where the direct shear phase would not. For example, Graves (1993) modeled the response of the San Francisco Marina District in the 1989 Loma Prieta earthquake as a shallow basin response to the Moho reflection.

The upper crust is significant because of its effect on the amplitude and frequency content of surface waves. Crustal surface waves can generate secondary surface waves in a basin that amplify and greatly extend the duration of strong shaking. In a simulation of ground motions in the Los Angeles basin from an earthquake on the San Bernardino segment of the San Andreas fault, Olsen *et al.* (1995) find that surface waves are amplified up to 10 times relative to sites outside the basin and that shaking is prolonged by 60 seconds. Wen and Helmberger (1997) compare the influence of surface waves in the upper crust and the Moho reflection on ground motions in the Los Angeles basin from the 1992 Landers earthquake. In this case, the surface waves are the dominant effect.

The background crustal structure also controls the impedance contrast between sedimentary basins and the crust. Wald and Graves (1997) compare synthetic waveforms from three 3D models of Los Angeles area basins with data from the 1992 Landers data. In their comparison of the models, they note that, in addition to differences in the basin seismic structure, the background structure varies among the models. This results in different effective basin depths that are reflected in quite different synthetic waveforms.

Sedimentary basins generate large amplitude multiples and surface waves closer to the source than occur in 1D structures. This is due to the basin edge. The effect of the basin edge is to weaken the direct phase and to enhance the reflected phases (Figure 1.1). The ray for the direct phase intersects the bottom of the basin obliquely where the interface is flat. As a result, the transmission coefficient for this ray into the basin is very small. In comparison, the ray for the reflected phases is nearly normally

Effects of the Edge of a Basin

Almost normally
incident. T ~ 1

Because of the lateral velocity
variation across the dipping layers,
rays can turn above the source.
$\theta \geq \theta_c$, so R = 1.

Obliquely incident,
so T is small
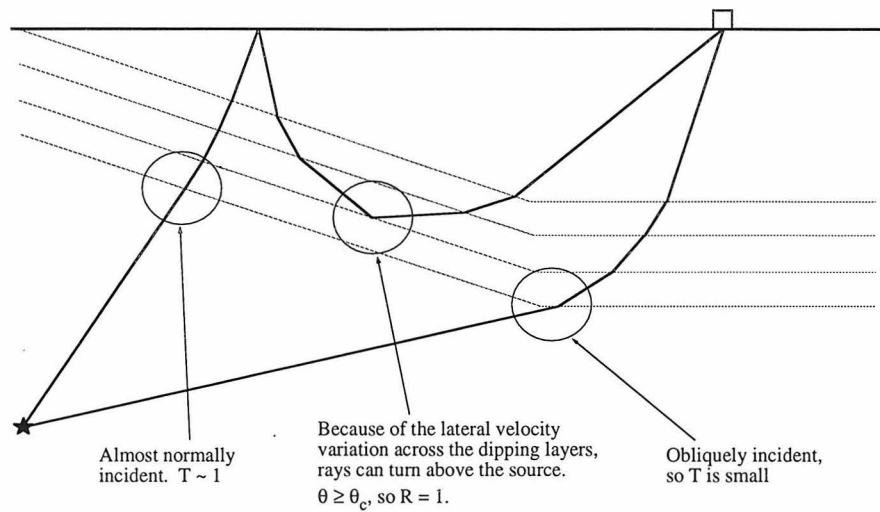
Figure 1.1: A cartoon indicating the effect, in terms of ray theory, of the edge of a sedimentary basin on propagating seismic energy. The solid star at the left is the seismic source, and the box at upper right is the receiver. The dashed lines are interfaces between velocity layers.

incident on the dipping edge of the basin. This ray has a transmission coefficient closer to 1 than does the direct ray. In addition, the lateral velocity gradient at the edge of the basin turns the ray of the multiple shallowly within the basin edge at greater than critical angle. Therefore, all of the transmitted energy gets trapped by the shallow structure and is channelled into the multiple phases and surface waves.

For the same reasons that the leading edge of the basin tends to trap energy, the trailing edge tends to leak energy. Vidale and Helmberger (1988) noted this at the south side of the San Fernando basin in their simulation of the 1971 Sylmar earthquake. In some cases, where the trailing basin edge is steep, it reflects surface waves back into the basin. Frankel (1993, 1994) reported such behavior in simulations and recordings of ground motions in the San Bernardino basin.

Site-specific ground motion features can be attributed to shallow, soft basins in the top few tens or hundreds of meters. The soil characteristics to these depths are found from borehole measurements, cone-penetration tests, or extrapolation of

surface geology. This site information is applied in the development of attenuation relationships for different site conditions (e.g., Boore *et al.*, 1997). It is also used to define a one-dimensional stack of velocities through which a reference ground motion is propagated. This introduces amplifications at resonant frequencies of the soil velocity structure.

Another approach is to consider the geometry of the shallow soil deposits and include lateral propagation effects. To date this has been applied in an ad hoc fashion (as micro-basins). In most cases, details of the soil deposits are too poorly known to constrain deposit velocities, depths, and shapes. When micro-basins are included, another set of basin generated waves is added to those generated by the deep basin. Kawase and Aki (1989) included a micro-basin into their model of the Mexico City lake sediments to explain the long duration of strong ground motions from the 1985 Michoacan, Mexico, earthquake. Saikia (1994) and Graves (1995) included them in models of the Los Angeles basin to explain rapid variations in ground motion duration and amplitude.

1.2 Summary of Chapters

This thesis includes an examination of the variability of propagation in the southern California crust and sedimentary basins, and detailed studies of phases generated in sedimentary basins by local earthquakes. Each chapter is an independent unit, with separate abstract and conclusions, but the thesis as a whole is concerned with ground motions in sedimentary basins and the contrast with propagation in the surrounding crust.

In Chapter 2, data from 1995 Ridgecrest, California, earthquake sequence is analyzed. This sequence was recorded by both the digital broadband TERRAscope network and the first strong motion stations in the installation of the TriNet digital seismic network. This collection of stations includes rock, soil, and basin sites. The sources are far enough from the Los Angeles area that surface waves are fully developed before they reach the sedimentary basins around Los Angeles. Comparison

of waveforms from adjacent rock and basin sites show clear secondary surface waves generated by the basins. Sites outside the basins, but behind the trailing edge, are also contaminated by the basin surface waves.

We also compare peak amplitudes recorded in different site conditions. In order to compare stations over wide distance and azimuth ranges, amplitudes from 1D synthetic waveforms are used as a measuring stick. At each site, the ratio of data to synthetic amplitude is found in three frequency bands from 0.1 to 1 Hz. Ratios at sites near source nodes are very large, indicating the data is somewhat insensitive to the nodes. Applying a 50% water level to the radiation pattern of the synthetics removes most of this instability. For all site conditions, the radial component has the most scatter. Data at most rock sites have amplitudes within a factor of 2 of the synthetic waveform amplitudes. Most basin sites have amplitudes within a factor of 3 of the 1D synthetic amplitudes.

In Chapters 3 and 4, earthquakes at the edges of the Los Angeles and San Fernando basins are modeled in detail. Three-component synthetic waveforms are calculated from 2D models of the basin using finite difference (Vidale *et al.*, 1985; Helmberger and Vidale, 1988). A forward modeling approach is taken to fitting the data. Much of the modeling effort is focused on the tangential component because, in both data sets, this component has the clearest basin-generated phases with the cleanest form.

Stations over the deepest portions of the Los Angeles basin recorded large shear wave multiples in the October 4, 1987 Whittier Narrows aftershock and the June 28, 1991 Sierra Madre mainshock (Chapter 3). The distance to these stations is less than 25 km and the most distinctive multiple is recorded at 16 km. At such distances horizontal velocity variations are required to produce multiples as large or larger than the direct phase. A model based the geologic cross-section of Davis *et al.* (1989), with a rough, blocky basin edge, traps energy in the basin, but does not focus it into the clear phases seen in the data. A smooth model of the basin edge is more effective. The Sierra Madre mainshock is 25 km NE of the edge of the Los Angeles basin. The structure from the Whittier Narrows modeling is extended to include the Sierra Madre source region and the intervening San Gabriel basin. Shear wave multiples at

sites in the Los Angeles basin from the Sierra Madre earthquake are still controlled by the edge of the Los Angeles basin. Phases generated in the San Gabriel basin propagate more slowly and arrive later in the records.

Waveforms from two aftershocks of the January 17, 1994 Northridge earthquake are modeled in Chapter 4. The records are from sites that extend across the San Fernando Valley from the NE corner to the central Santa Monica Mountains. The two events are in a similar location, but one is just beneath the basin and the other is deeper, at 16 km depth. Distinctive features in the records from the shallow source include large amplitude surface waves and extended coda at a cluster of stations about 8 km into basin, and a phase shift of the direct S at stations just beyond the basin. An array analysis for back azimuth and slowness (Frankel *et al.*, 1991) was done on the cluster of stations that recorded the large surface waves in the shallow event. This analysis confirms that the surface waves are coming from the direction of the source and can be modeled with a 2D structure. The final model is a simple model with a strong gradient in the upper basin, a total depth of the basin of 3 km, and a significant gradient below the basin at 5.5 km. Perturbations are made to the model to examine the sensitivity of the data to changes in different portions of the model. This model is compared to other 2D and 3D models of the San Fernando basin that have been used in waveform studies and simulations.

Chapter 2

Variability of Ground Motions in Southern California – Data from the 1995 Ridgecrest Sequence

2.1 Abstract

Data from the 1995-1996 Ridgecrest, California earthquake sequence, recorded by the TriNet digital seismic network, provides high quality waveforms from sites throughout southern California, including sites in markedly heterogeneous areas like the Los Angeles area sedimentary basins. Synthetic waveforms generated with 1D models are used as a baseline to measure the variability of data amplitudes throughout southern California. Three frequency bands are examined: 0.1 to 0.2 Hz, 0.2 to 0.4 Hz, and 0.4 to 0.8 Hz. Sites are characterized as rock, soil, or basin. Rayleigh waves on the radial component vary in amplitude more than surface waves on other components. Our initial 1D model under predicts the amplitude of the radial component at all types of sites. A 3 km thick slow layer improves the fit of the synthetic waveform amplitudes, particularly at higher frequencies, but the radial component still shows the most scatter. There is greater variability in the amplitudes from basin site records than from rock sites records. Rock, soil, and basin sites are all rather insensitive to nodes in the horizontal radiation pattern. This complicates the analysis because the nodes create singularity points in the distribution of ratios of observed and synthetic amplitudes. In particular, a Love wave node runs through the Los Angeles basin area for all three events. When data near nodes are removed, the data at most rock sites have amplitudes within a factor of 2 of synthetic waveform amplitudes. Data from

a few stations vary more (up to 3 times the synthetic amplitudes). Soil and basin stations are more variable relative to the synthetic waveforms, with the bulk of the distribution of data/synthetic amplitude ratios less than 3 and a few outliers greater than 5. These outliers occur at the higher frequency bands. Soil and basin sites are also more often larger than the synthetics (higher median values). Most outliers can be explained by applying a water level of 50% to the radiation pattern. This reduces the scatter in the distributions to about the same extent as removing data within 10° of nodes. Thus, most of the outliers are sites that are insensitive to the nodes, not sites that are larger than the overall data distribution. Of the remaining outliers, that are not explained by insensitivity to nodes, some are in the southern Los Angeles, Santa Barbara, and Ventura basins. Others are south of the Los Angeles and Imperial Valley basins. These sites indicate that basin-generated surface waves are propagating through the trailing edge of these basins.

2.2   Introduction

Earthquakes north of Ridgecrest, California were the first sequence of moderate events to be recorded by the strong motion component of the TriNet digital network. The earthquakes span the period from mid-August 1995 to early-January 1996 (Table 2.1). The data set is unusual in that it includes records of surface waves from a moderate earthquake as they pass through the Los Angeles basins (Los Angeles, San Fernando, San Gabriel and San Bernardino). The events are small enough that the source can be taken as point sources. The events are far enough away from the basins that surface waves have already developed in the wavefield before it hits the basins. This allows us to compare surface waves on records at stations inside and outside the basin (Figure 2.1).

This paper examines surface waves in sedimentary basins, but the variability of surface wave amplitudes at hard rock sites outside the basins is also considered. There are a number of 1D models for localized portions of the southern California crust. (see Qu *et al.*, 1994, for a list of models for the Los Angeles region). A 1D model
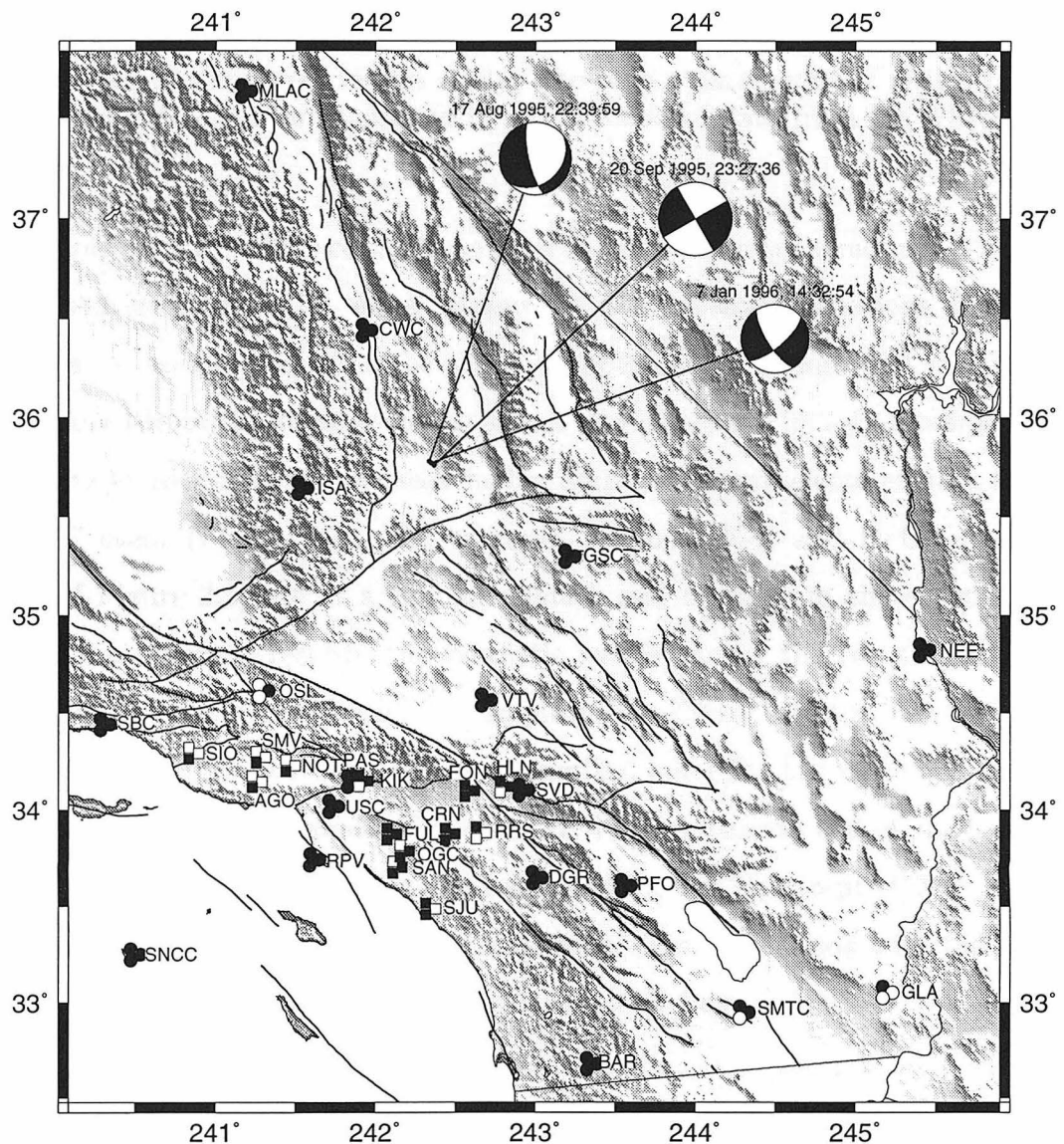
Figure 2.1: Events examined in this study and the stations at which records are available. Circles indicate TERRAscope very broadband velocity receivers. Squares indicate K2 force balance accelerometers. Three symbols are shown for each station, one for each event. A black (white) symbol indicates the event was (not) recorded by that station. The thick black line is the California coast and border. The thin black lines are some significant faults in southern California. The grey lines are highways.

Date	Time	Strike	Rake	Dip	Moment	Depth
17 August 1995	22:39:59	50	330	30	1.6×10^{24}	11
20 September 1995	23:27:36	60	0	90	2.2×10^{24}	14
7 January 1996	14:32:54	50	340	70	5.6×10^{23}	8

Table 2.1: Events analyzed in this study. The source parameters of strike, rake, dip, moment, and depth were calculated in an inversion of data from the TERRAscope portion of TriNet.

for the entire region will necessarily be a model of the average structure. The scatter around that average can be seen in amplitude, and waveform variations. The level of amplification seen in basins can be compared against this background variability.

The data from the three events is shown in Figures 2.2 to 2.4. Examples of the variability at rock sites can be seen in the horizontal components of data from the 95/08/17 event (Figure 2.2). For example, stations DGR and PFO (upper right corner of Figure 2.2) are at a similar azimuth and range from the event. For the tangential component records, the synthetic waveforms for the two stations predict very similar amplitudes, but the data amplitudes differ by a factor of two. The long period shape of these waveforms are very similar, but PFO has twice the amplitude at periods from 2 to 4 seconds. The same kind of comparison can be made between stations BAR and SMTC (center right side of Figure 2.2), except that in this case, SMTC is dominated by a large coda, most likely from interaction with the Imperial Valley, and it is significantly larger than BAR at all frequencies.

Figure 2.2: (next page) Displacement records of the 95/08/17 Ridgecrest earthquake, organized by site characteristics. Source parameters for synthetics are from an inversion of the complete data set for the event. For each station, the three waveforms are: standard model synthetic (top), data (middle), and variant model synthetic (bottom). The data are aligned by the time of the first geometric shear wave arrival for the standard model (vertical lines). For each station, the data and synthetics are plotted from the same reference time, then the shift from the inversion (in seconds, in parathesese at left end of the synthetic) is applied to the synthetic used in the inversion (postive to the right). The data are plotted in absolute amplitude scaled by a range factor, $r^{0.5}$. The range (in km) is at the left end of the data trace. For each station, the three traces are plotted on the same scale; the peak amplitude (in cm) of the data is shown on the right end of the trace.

China Lake 95/08/17 22:39:59
Displacement
Rock Sites
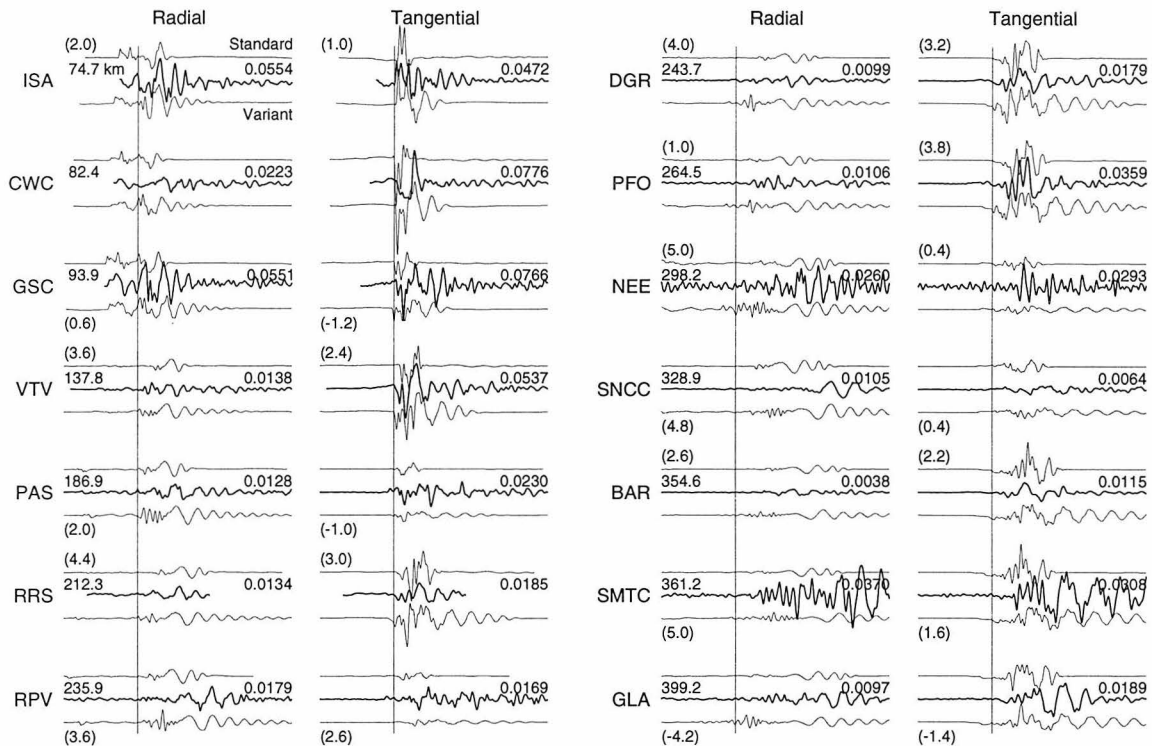
Soil Sites
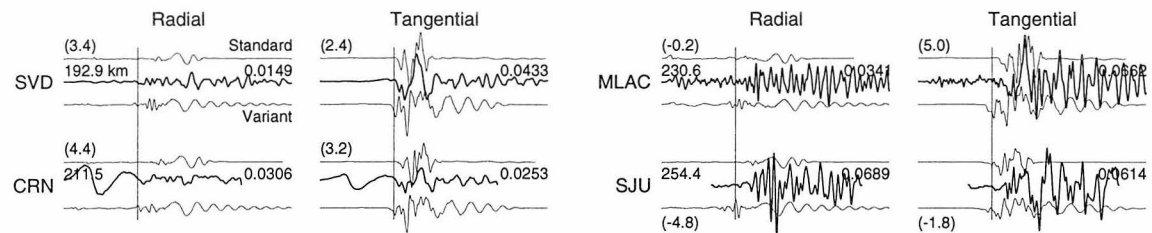
Basin Sites
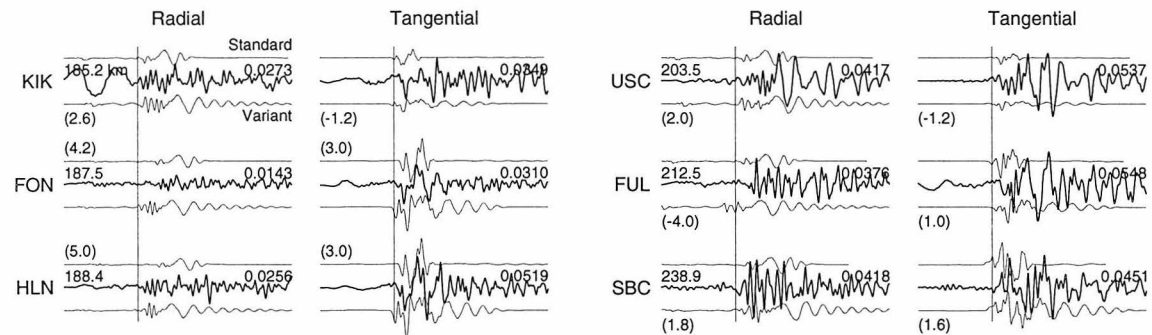
40 seconds

In another comparison of data from the 95/08/17 event, a Love wave node falls near stations RPV and PAS, while DGR should have large amplitude Love waves. Instead, the data amplitudes for all three stations are very similar. In this case, high frequencies are not strong at any of the stations. In contrast, NEE is expected to be affected by a node, but tangential data amplitudes are as high as those at PFO. NEE is particularly noisy at high frequencies. This level of variability between sites outside the basins should be kept in mind when comparing them to basin sites.

Body waves approaching the edge of a basin are more readily refracted into and trapped near the surface than when propagating through a laterally homogeneous media. Surface waves can be generated by a basin much closer to the source than occurs in 1D media. Because large amplitudes and long durations can be generated near the source in this way, the conversion of body waves to surface waves at basin edges has been studied extensively in 2D and 3D (early examples being Bard and Bouchon, 1980a,b; Frankel and Vidale, 1992). In the basin stations in Ridgecrest data set, we find incident surface waves generating secondary surface waves in the basin. For example, in Figure 2.5, tangential components of records from the 95/08/17 event at the rock site PAS and the nearby basin station KIK are shown to be quite similar for 10-15 seconds after the first shear wave motion. At the point where a large second phase arrives at PAS, the same phase arrives at KIK and coda begins that is not seen at PAS. Similar basin-generated waves are seen in the comparison of records from the soil station CRN and basin stations FUL, OGC, and SAN in Figure 2.6.

The 1992 Landers earthquake and its aftershock sequence provided an extensive data set to study the interaction of surface waves with sedimentary basins. Frankel (1994) deployed small arrays in the San Bernardino basin and tracked surface waves reflecting off the edges of the basin. Qu *et al.* (1994) used a Gaussian beam method to model focusing of surface waves in the Los Angeles area by lateral heterogeneity in


Figure 2.3: (next page) Displacement records of the 95/09/20 Ridgecrest earthquake, organized by site characteristics. The plotting and scaling conventions are the same as those used in Figure 2.2.

China Lake 95/09/20 22:27:36
Displacement
Rock Sites
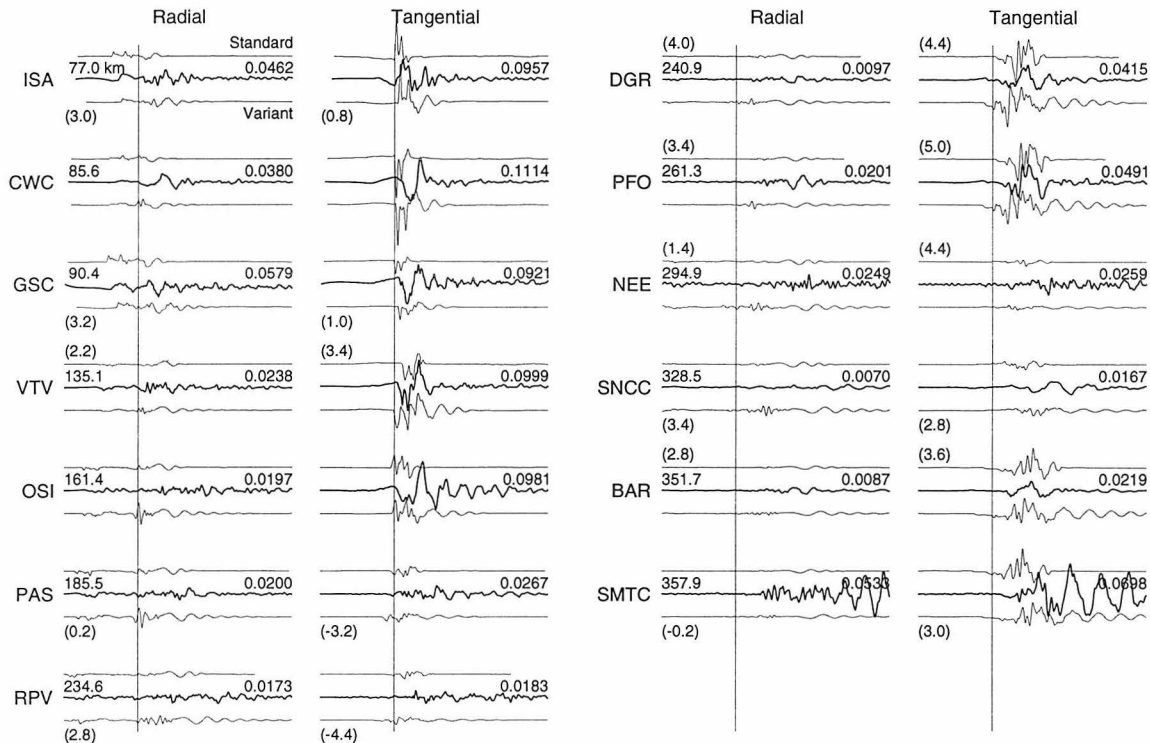
Soil Sites
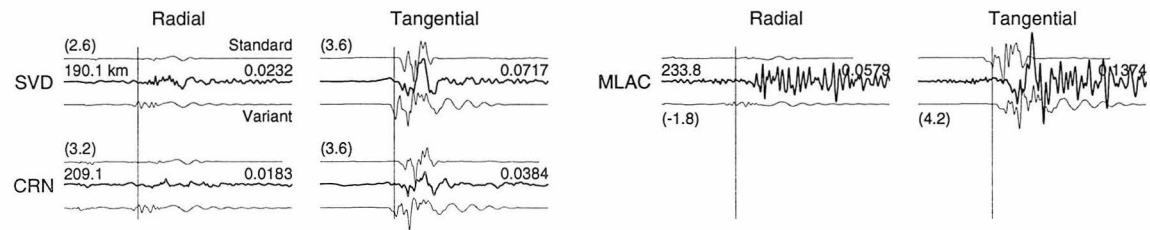
Basin Sites
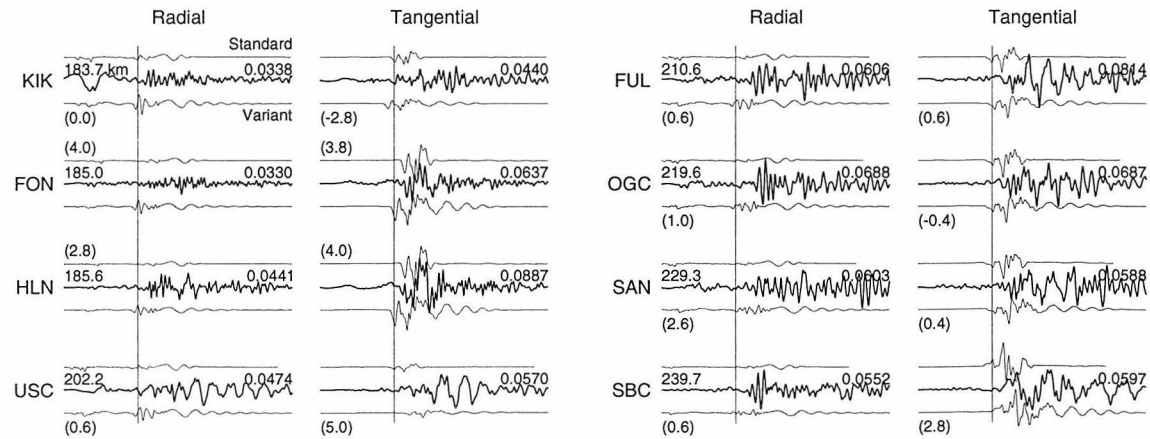
40 seconds

the crust. Wald and Graves (1997) tested the ability of current 3D seismic models of the Los Angeles, San Fernando, and San Gabriel basins to produce accurate ground motions.

Surface waves in basins are of engineering interest because they are often the largest arrivals at a site, they are of long duration, and the frequency content of the shaking is similar to the resonance frequencies of tall buildings, bridges, and other large, flexible structures. In southern California, the San Andreas fault has the potential to generate the largest earthquakes, and is far enough away from the Los Angeles area that surface wave amplification by the basins is an important concern. Olsen *et al.* (1995) have simulated a M 7.75 earthquake on the San Bernardino segment of the San Andreas fault and the subsequent propagation of energy into the Los Angeles and San Fernando basins. Their simulation produces much larger spectral amplitudes in the basins than at surrounding sites (up to 10 times higher at 4-5 seconds period). Teng and Qu (1996) simulated long period ground motions and strain distribution from M 8.25 earthquake on the Mojave segment of the San Andreas fault. They find peak amplitudes up to 3 m at 3-10 seconds period, and localized strains of $10^{-2} - 10^{-3}$.

These simulations suggest that surface waves at 60-100 km distance from the source can produce ground motions large enough to be of great engineering concern. Our confidence in these simulations and their applicability to engineering design will increase as they are grounded in data and an understanding of the variability in recorded ground motions.

Figure 2.4: (next page) Displacement records of the 96/01/07 Ridgecrest earthquake, organized by site characteristics. The plotting and scaling conventions are the same as those used in Figure 2.2.

China Lake 96/01/07 14:32:54
Displacement
Rock Sites
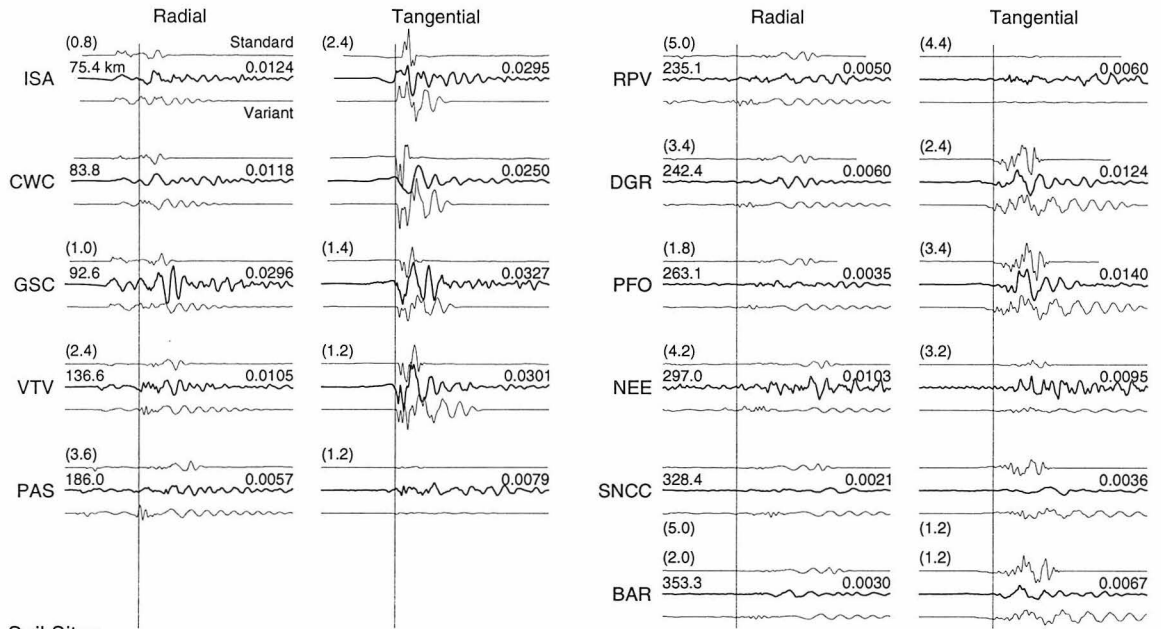
Soil Sites
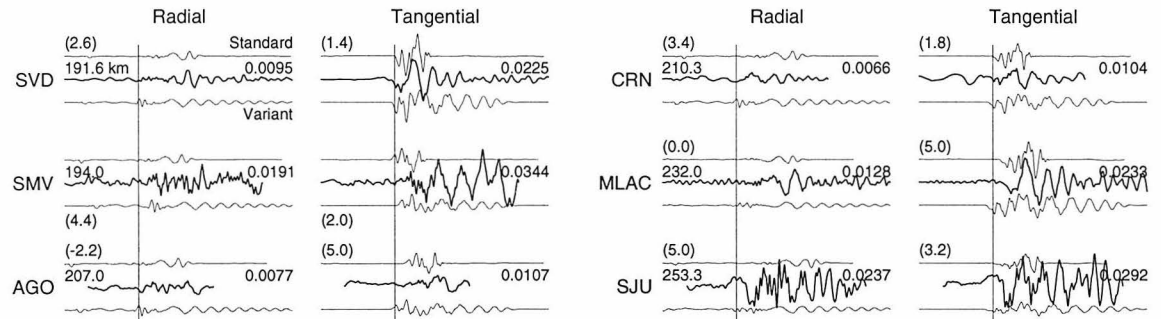
Basin Sites
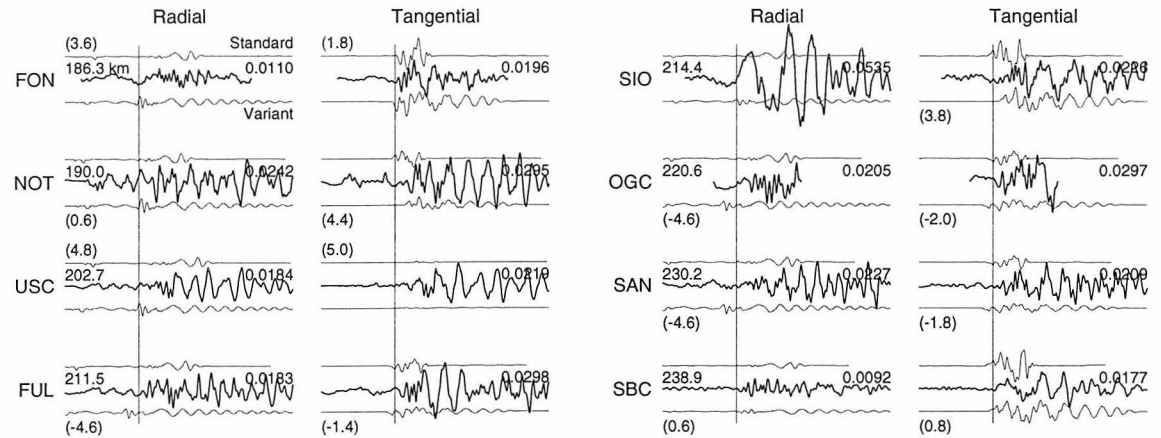
40 seconds

95/08/17 Tangential
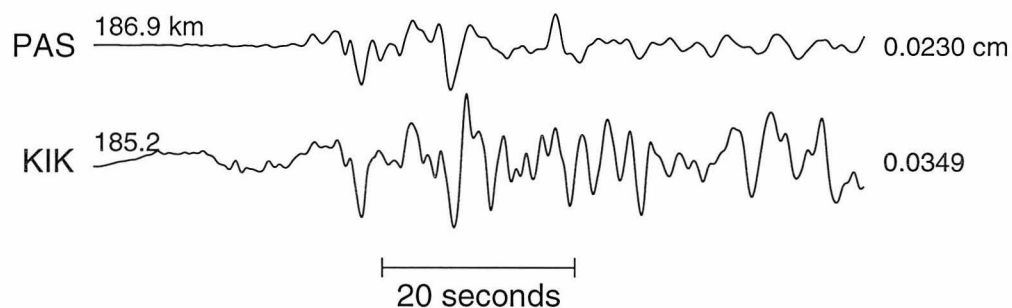
Figure 2.5: Tangential component records from stations PAS and KIK for the 95/08/17 event. The waveforms are plotted on the same amplitude scale and with absolute timing. The range and peak amplitude are indicated at the left and right ends of each trace, respectively.

95/09/20 Tangential
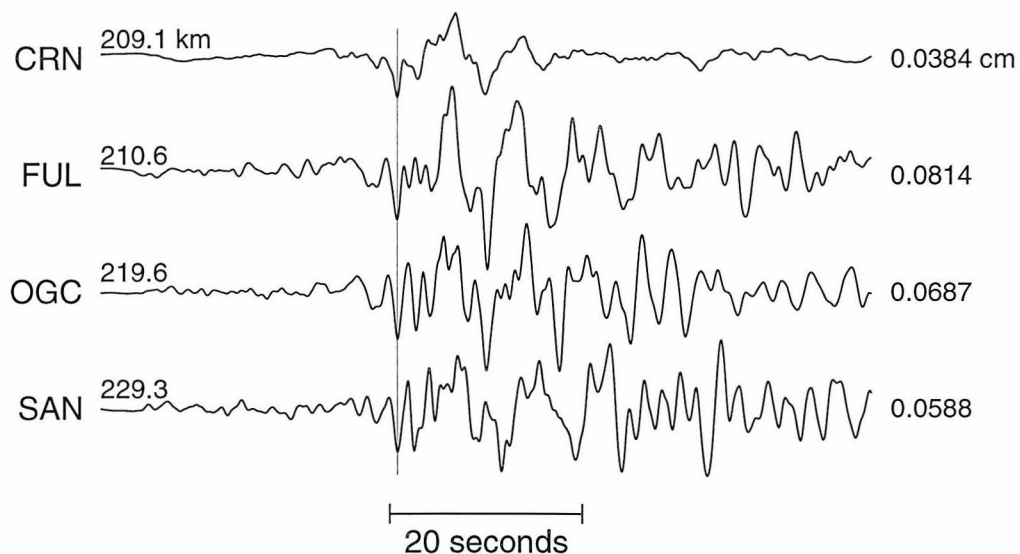
Figure 2.6: Tangential component records from stations CRN, FUL, OGC, and SAN for the 95/09/20 event. The waveforms are plotted on the same amplitude scale and aligned on the phase indicated by the vertical line. The range and peak amplitude are indicated at the left and right ends of each trace, respectively.

2.3 Data

The first two months of the Ridgecrest sequence were described by Hauksson *et al.*
(1995a). The first two events analyzed in the current paper are the two main events
discussed in the Hauksson *et al.* paper. They are moderate size events, but the first
event may have had some rupture complexity. Source parameters determined from
surface waves indicate a source with more strike-slip component than the first-motion
source determination. This suggests that the faulting style changed during rupture.
Our inversions (described below) using both P_{nl} and surface waves find a solution
similar to the first motion source determinations. The third event discussed in our
paper occurred after the period studied by Hauksson *et al.* (1995a).

The data analyzed in this paper is from the digital TriNet seismic array in southern
California. The array consists of three subnets with a small number of very-broadband
receivers, many broadband receivers, and a number of strong motion accelerometers.
At the time of the Ridgecrest sequence, data was available from the TERRAscope
and K2 subnets (Table 2.2).

TERRAscope is the very broadband subset of the complete array. There are 20
sites consisting of a Strekeisen STS-1 or STS-2 velocity sensor and a 24-bit Quanterra
data logger. The data are sampled at 20 samples/second. The response is flat in
velocity from 100 seconds (300 seconds for STS-1 sensors) to 7 Hz.

K2 is the strong motion subset of the complete array. The instrument package
consists of a Kinemetrics 3-component FBA and 19-bit data logger. The data is sam-
pled at 100 samples/second. The response is flat in acceleration up to 25 Hz. At the
time of the Ridgecrest events, the strong motion subnet was still under installation,
with about 10 stations, and the handling of the data was not completely automated.
As a result, the particular stations available for each event changes and in some cases
the available waveform ends before the coda is complete. Some records from stations
CRN and KIK have large long period noise in the P_{nl} portions of the waveform. This
portion of the records was clipped before finding peak amplitudes.

Site conditions for stations are defined as either rock, soil, or basin (Table 2.2).

	TERRAscope		K2	
Rock	BAR	Barrett	RRS	Riverside
	CWC	Cottonwood Creek		
	DGR	Domenigoni Valley		
	GLA	Glamis		
	GSC	Goldstone		
	ISA	Lake Isabella		
	NEE	Needles		
	OSI	Osito Canyon		
	PAS	Pasadena		
	PFO	Pinon Flat		
	RPV	Rancho Palos Verdes		
	SMTC	Superstition Mountain		
	SNCC	San Nikolas Island		
	VTV	Victorville		
Soil	MLAC	Mammoth Lakes	AGO	Agoura
	SVD	Seven Oaks Dam	CRN	Corona
			SJU	San Juan Capistrano
			SMV	Simi Valley
Basin	SBC	Santa Barbara	FON	Fontana
	USC	University Southern California	FUL	Fullerton
			HLN	Highland
			KIK	Kinemetrics
			NOT	Northridge
			OGC	Orange
			SAN	Santa Ana
			SIO	Ventura County

Table 2.2: Site characterization of TERRAscope and K2 stations

Basin sites were designated by a combination of surface geology and current 3D models of the Los Angeles, San Fernando, and San Bernardino basins. The classification of basin sites is not a differentiation included in strong ground motion attenuation relationships (e.g., Boore *et al.*, 1997). Normally soil sites are distinguished by the characteristics of the top few 10's of meters beneath the surface. Here we are concerned with the difference between deep (greater than 1 km) basins and the surrounding crust.

The TERRAscope data was highpass filtered with a corner at 0.05 Hz, and integrated to displacement. The K2 data was handled in the same way, except that an additional step of integration was required going from acceleration to displacement. For the 95/08/17 and 95/09/20 events, a K2 station was maintained at the same site as the Pasadena TERRAscope site. Figure 2.7 compares the traces for the two instrument packages after the processing described above. The K2 traces are shorter than their TERRAscope counterparts as mentioned above, and contain long period noise. Otherwise, the waveshapes are identical. The waveforms are all plotted on the same scale. The K2 records have somewhat lower peak amplitudes than the TERRAscope records (except the tangential component of event 95/09/20). This variation is within 10% of the amplitude of the TERRAscope tangential and radial traces, and within 25% of the amplitude of the TERRAscope vertical traces.

Examining the data set as a whole (Figures 2.2 to 2.4, there is a strong contrast between the duration of shaking at rock sites and basin sites. Shaking at most rock site is relatively short (10-20 seconds). The tangential component is typically dominated by the fundamental mode Love wave. Stations with nodes on the tangential component (e.g., PAS and RPV) are emergent, with the peak amplitude 10-15 seconds behind the direct shear wave. The radial component is more variable in amplitude and waveform than the tangential component. In most cases, the Rayleigh waves dominate the records, but at some stations (for example, VTV) high frequency S_{nl} waves are also strong.

Basin sites have longer durations than rock sites. Typically, the long period surface waves extend 40 seconds or more after the fundamental surface waves. Coda on the
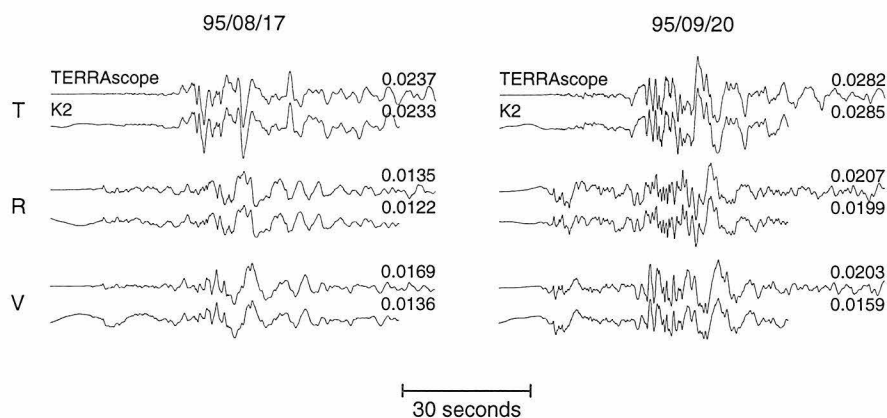
95/08/17   95/09/20

Figure 2.7: TERRAscope and K2 waveforms from the Pasadena site for the 95/08/17 and 95/09/20 events. The waveforms are all plotted on the same amplitude scale. The peak amplitude is indicated at the right end of each trace.

radial component tends to have higher frequency content than coda on the tangential component. Coda amplitudes on both components are often as large as the main surface waves. Records from soil sites vary greatly. They tend to mimic one of the two extremes, rock or basin.

Typically, the tangential component at basin stations is emergent. The largest amplitude in the surface waves arrives 10-20 seconds later than the peak on soil or rock sites. When compared to timing on radial component records, the largest arrivals on the tangential component appear to be multipathed Rayleigh waves. The amplitude of these waves on the tangential component are comparable to the amplitudes on the radial and vertical components.

Particularly notable waveforms are those from SMTC, SJU, FON, HLN, and SIO. Both SMTC and SJU show signs of the wavefield's interaction with neighboring basins. SMTC is just southwest of the Imperial Valley. The long duration of large, long period surface waves at SMTC is in sharp contrast to the records at surrounding sites PFO, BAR, and GLA, all of which skirt the Imperial Valley. Ho-Liu and Helmberger (1989) and Helmberger *et al.* (1992) modeled waveforms from earthquakes in and around the Imperial Valley and recorded at Pasadena. They found that surface waves developed in the Imperial Valley passed into the surrounding crust and

persisted to large distances as strong coda. Our data indicates that the reciprocal path is just as effective in trapping surface waves. The entire path consists of surface waves striking the basin, the generation of secondary surface waves in the basin, and the entire package of surface waves propagating from the basin to the down-range site of SMTC. SJU is south of the Los Angeles basin on Tertiary marine sedimentary rock. The period of the coda at this station is similar to that seen in southern Los Angeles basin stations FUL and SAN. The coda also seems to have similar duration and amplitude of coda as the basin stations, but unfortunately the records at SJU are cut off before the coda ends. These two sites indicate that surface waves generated in basins can propagate, with little apparent diminution, to sites beyond the trailing edge of the basin.

FON and HLN show relatively little basin effect. The San Bernardino basin and the alluvium deposits around Fontana are shallower than the San Fernando and Los Angeles basins and may not be deep enough to cause effective trapping of the 5-10 second surface waves that dominate records from the rock and soil sites around it (VTV and SVD).

SIO has an anomalously large radial component. Unfortunately, it only recorded the third event and the ground motion can't be compared for different events. This station is at the edge of the deep Ventura basin, and edge effects might explain the large amplitudes.

2.4 Analysis

We use hard rock sites from the TERRAscope subarray of TriNet as the background wavefield against which to compare basin stations. The comparison is indirect, using the amplitude of synthetic waveforms from 1D velocity models as a measuring stick. This allows comparison of data from stations at a range of distances and azimuths from the sources.

The velocity models used in the analysis are a generic model of the southern California crust and a variant with a slow surface layer (Figure 2.8). The generic

model, that we refer to as the standard model, was used in inversions of TERRAscope data by Zhu and Helmberger (1996) for earthquake source parameters throughout southern California. In our inversions for source parameters and our comparisons of data from hard rock, soft rock, and basin sites, we apply both the standard model and the variant with a slow surface layer. Synthetic waveforms are calculated for these models by the reflectivity method (Saikia, 1994). The top layer in the variant model has $Q_p = 100$ and $Q_s = 50$. Synthetic waveforms were also calculated with this layer set to $Q_p = 600$ and $Q_s = 300$. The change in peak amplitude with attenuation was negligible.

The inversion technique is a grid-search over the parameter space. The P_{nl} and surface wave segments of the waveforms are handled separately in the inversion. Each segment is allowed small, independent shifts in timing. Absolute amplitudes are kept in the inversion, with a weighting scheme to evenly emphasize data from different ranges (Zhao and Helmberger, 1994; Zhu and Helmberger, 1996). The inversion with absolute amplitudes is sensitive to nodes in the data.

For each event, three inversions were done for source mechanism parameters strike, rake, dip, moment, and depth (Figure 2.9). In the first inversion, waveforms from only the rock TERRAscope sites were used. The parameters found are very similar to the inversion done by Zhu and Helmberger (1996). The second inversion was in fact a series of single-station inversions with each solution parameter constrained to within $\pm 10°$ of the parameter value from the first inversion. The single-station inversion was run for both the standard and variant models, and the model with the lower error was selected as the preferred model for that station. Some stations had high errors for both models and were dropped from the final inversion The final inversion was based on all the data, with each station fitting its preferred model. The synthetics, including time shifts, for this solution are shown in Figures 2.2 to 2.4. For each event, this final source solution was very similar to the first inversion solution (row 1 of Figure 2.9). Most of the data added in the final inversion is from stations in the Los Angeles area, clustered around a Love wave node in the original inversion solution. The similarity of the final inversion to the original inversion increases our confidence
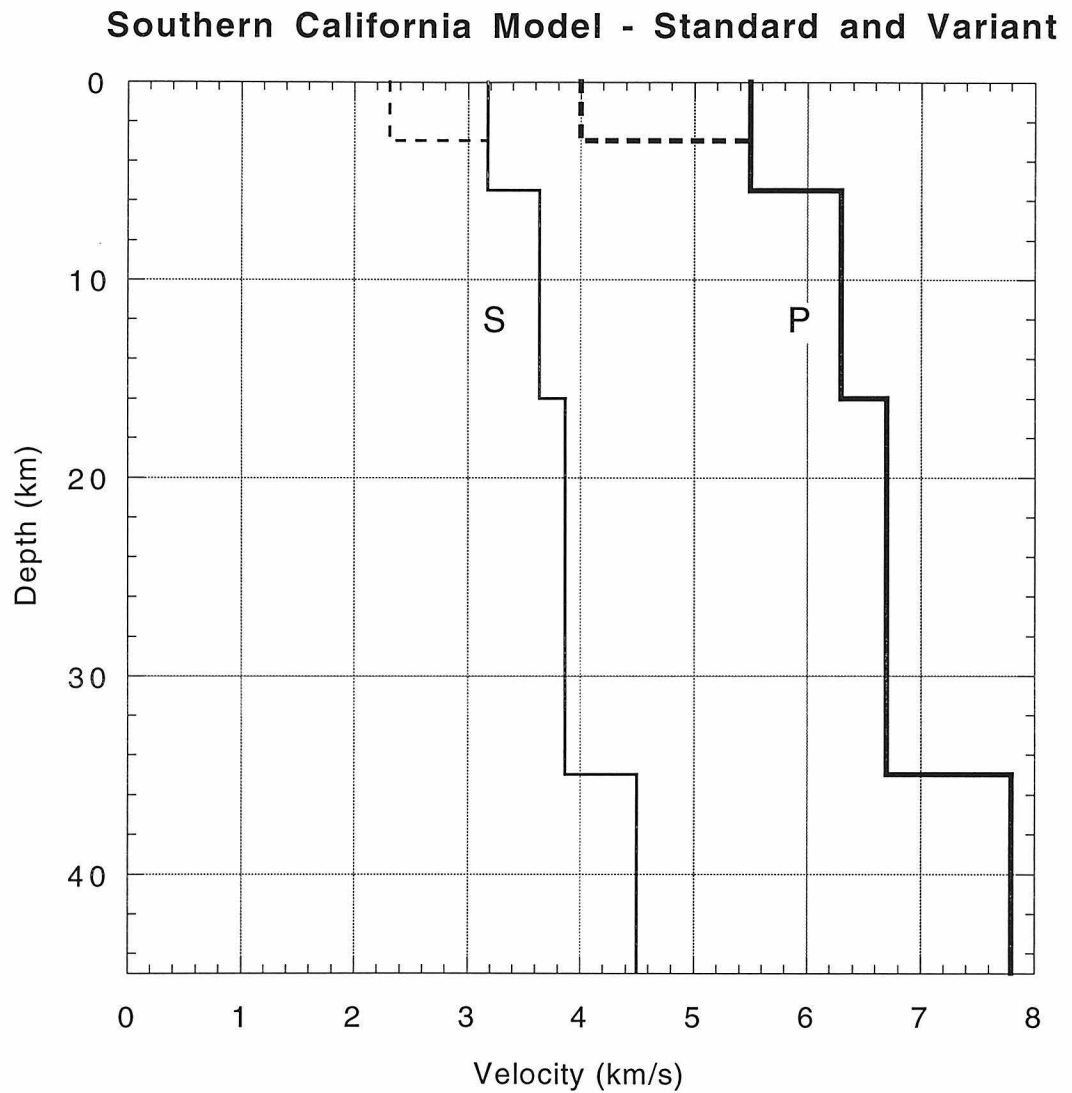
Figure 2.8: 1D models for the southern California crust. The solid lines are a standard model. The dashed lines indicate a variant slow top layer. Values of Q_p and Q_s are 600 and 300 throughout the standard model. The surface layer in the variant model has Q_p and Q_s of 100 and 50.
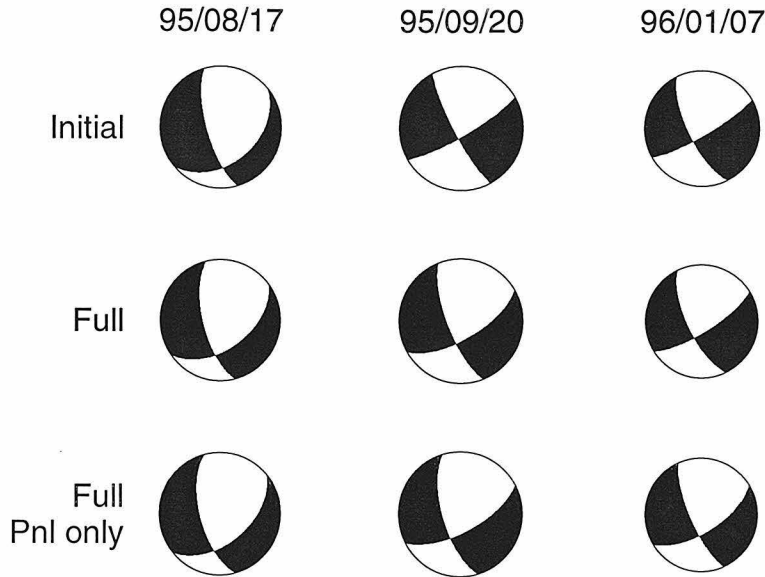
Figure 2.9: Lower-hemisphere focal mechanisms for the three China Lake events in this study. For each event results are shown from an initial inversion with a subset of the data, a final inversion with all stations, and an inversion with all stations but including only the P_{nl} segment of the waveforms. The size of the mechanism is scaled by the magnitude found in the inversion. See text for details of these inversions.

that the inversion is accurate, including the location of nodes in the radiation pattern.

In these inversions, the moment is controlled by the peak amplitudes of the waveform segments. Thus surface wave amplitudes will be fit by synthetics with the moment from the inversion. Because of variations in amplitude from site to site, however, there is scatter around this average fit. An error in the source depth estimate would change the moment returned by the inversion and affect the relative amplitude of the P_{nl} and surface wave segments of the synthetic waveforms. Since we are focusing on surface waves, and looking at ratios of data to synthetic, our results are insensitive to these effects. Nonetheless, to check the depth estimate of the full inversion, another inversion was run using only the P_{nl} portion of the waveforms (row 3 of Figure 2.9). This inversion returned very similar focal mechanism parameters, including depth and moment, for all three events.

We compare amplitudes of the waveforms from the hard rock, soft rock, and basin

sites in 3 pass bands: 0.1 - 0.2 Hz, 0.2 - 0.4 Hz, and 0.4 - 0.8 Hz.

In Figures 2.10 and 2.11, the peak amplitudes of surface waves recorded 185-253 km from the 95/09/20 event are compared to the amplitudes of the synthetic waveforms at 220 km for the two crustal models. The data are differentiated by site type and frequency bandpass. The range of the data examined here is limited to the region directly around the Los Angeles basin region. The 95/09/20 event has a pure strike-slip mechanism, with a tangential node among the stations in this distance range, so the contrast between the synthetic and data amplitudes at the node can be clearly examined. The variation in peak amplitude expected across this range, from the synthetic waveforms, is about 0.01 cm, which is much less than the scatter in the data amplitudes on the horizontal components, so the comparison of the data with synthetic waveforms calculated at one range is reasonable for this discussion. Later we will use synthetics for each specific site to compare amplitudes over the whole data set.

On the horizontal components, the peak amplitudes of the basin stations, in all three frequency bands, are larger than those of the rock and soil sites. On the radial component, the high frequency pass band has particularly large peak amplitudes. The vertical component has less variation between types of sites and across the frequency pass bands.

In general the synthetic amplitudes from the standard model (Figure 2.10) are comparable to the data amplitudes, even at basin stations. On the tangential component, data from the rock and soil sites east of the node (160°-180°) are smaller than the synthetic predicts. Around the node, data from the basin sites are larger than predicted by the synthetics, though the amplifications are slightly depressed at the node. There is no clear frequency dependency for this insensitivity of the data to the node. On the radial component, the rock and soil site amplitudes are fit well, but the basin sites are 2-4 times higher (and even more at higher frequencies). Only a few stations are near nodes on the radial and vertical components, but from this data it appears that data on the vertical component follows the nodes more closely than data on the radial component.
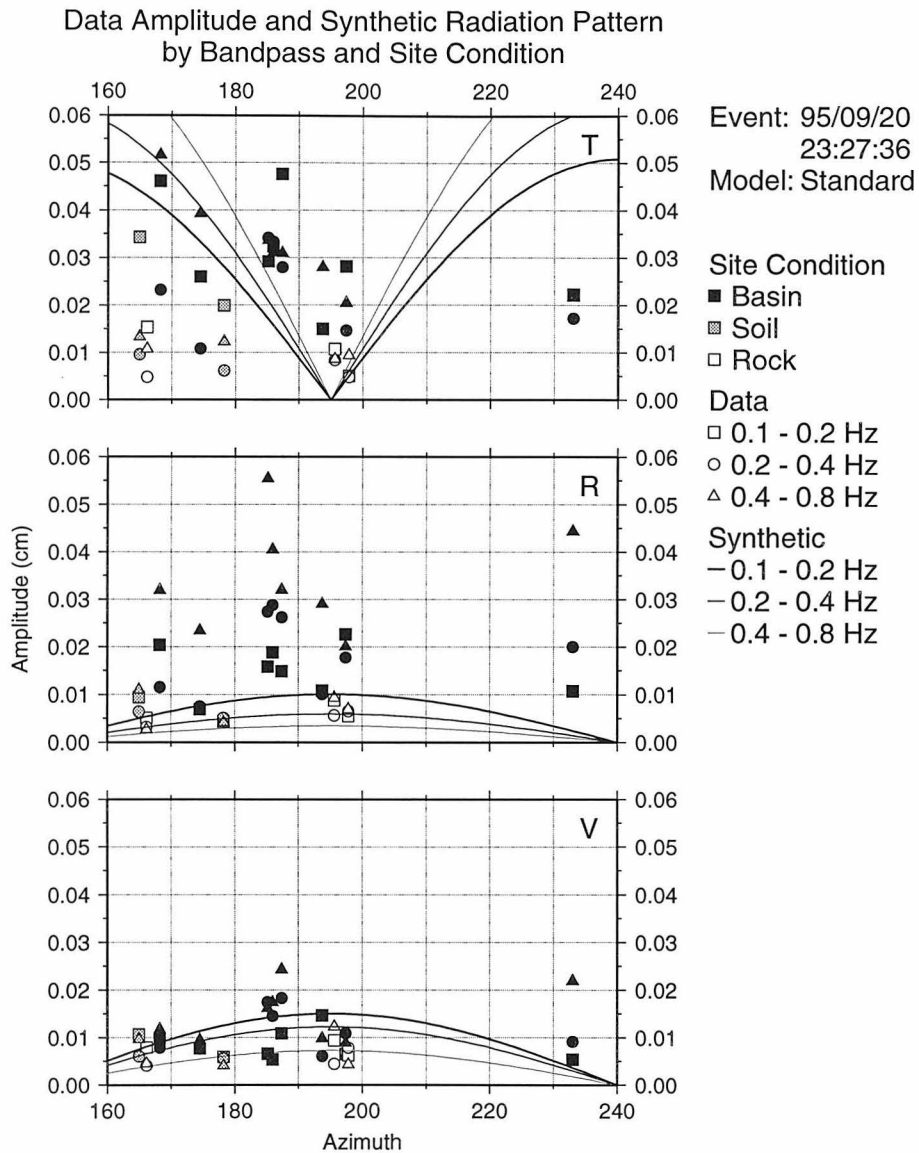
Figure 2.10: Maximum amplitudes of a subset of data from the 95/09/20 event and synthetic waveforms from the standard model. Station distances range from 185 km to 253 km. The synthetic waveforms were calculated for 220 km distance. Data are discrete points, synthetics are curves. Amplitudes are shown for three different bandpasses of the waveforms, with the square/circle/triangle symbol indicating a bandpass of 0.1-0.2/0.2-0.4/0.4-0.8 Hz, respectively. Shading of black/grey/white indicates a basin/soil/rock site condition, respectively. The top plot is the tangential component, the center plot is the radial component and the bottom plot is the vertical component.

Figure 2.11: Same as Figure 2.10, but synthetic waveform amplitudes are generated with the variant model.

Application of the variant model with the slow upper layer (Figure 2.11) improves the fit to the amplitudes of the horizontal components, but has little effect on the vertical component. On the tangential component, the main effect of the variant model is to reduce the amplitude of the synthetics in the long period pass band. On the radial component the change in the synthetic amplitudes is more significant. The amplitude in the 0.4-0.8 Hz pass band is about 5 times higher and the amplitude in the 0.2-0.4 Hz pass band is about 3 times higher. These match the data points on the radial component more closely, and in particular the relative amplitudes of the different pass bands are better modeled.

These are qualitative comparisons of a subset of the data from one event. In order to include the entire data set, with ranges from 75 km (station ISA) to 400 km (station GLA) and a wider range of azimuths, we take the ratio of the peak amplitude of the data and the synthetic waveform for the appropriate azimuth and range. Because the moment in the synthetics is based on the inversion, the ratio of the maximum amplitude of the data and the synthetics should be about 1. However, the inversion is done with the long period end of the data (greater than 5 sec) so there will be shifts away from 1 in the higher frequency pass bands used in the ratios.

Figures 2.12 and 2.13 are ratios relative to the standard model and the variant model, respectively, for all the data from event 95/09/20. On the tangential component, the ratios for the standard model cluster around and below 1, except around the node at 194°. Using synthetics for the variant model has little effect, but does bring some ratios up toward 1. On the radial component, the scatter of ratios is large for the standard model, but use of the variant model brings ratios down to 2 or below (away from nodes). On the vertical component, the scatter in ratios for the standard model occurs in the higher frequency bandpasses for a few basin stations. Use of the variant model reduces this scatter slightly.

To summarize the comparison of data and synthetic amplitude ratios for all three events as a single data set, the distributions of ratios are presented as boxplots (Devore, 1987). Each component and pass band is handled as a separate data set. In boxplots (Figure 2.14), the thick horizontal line in the box is the median of the data.
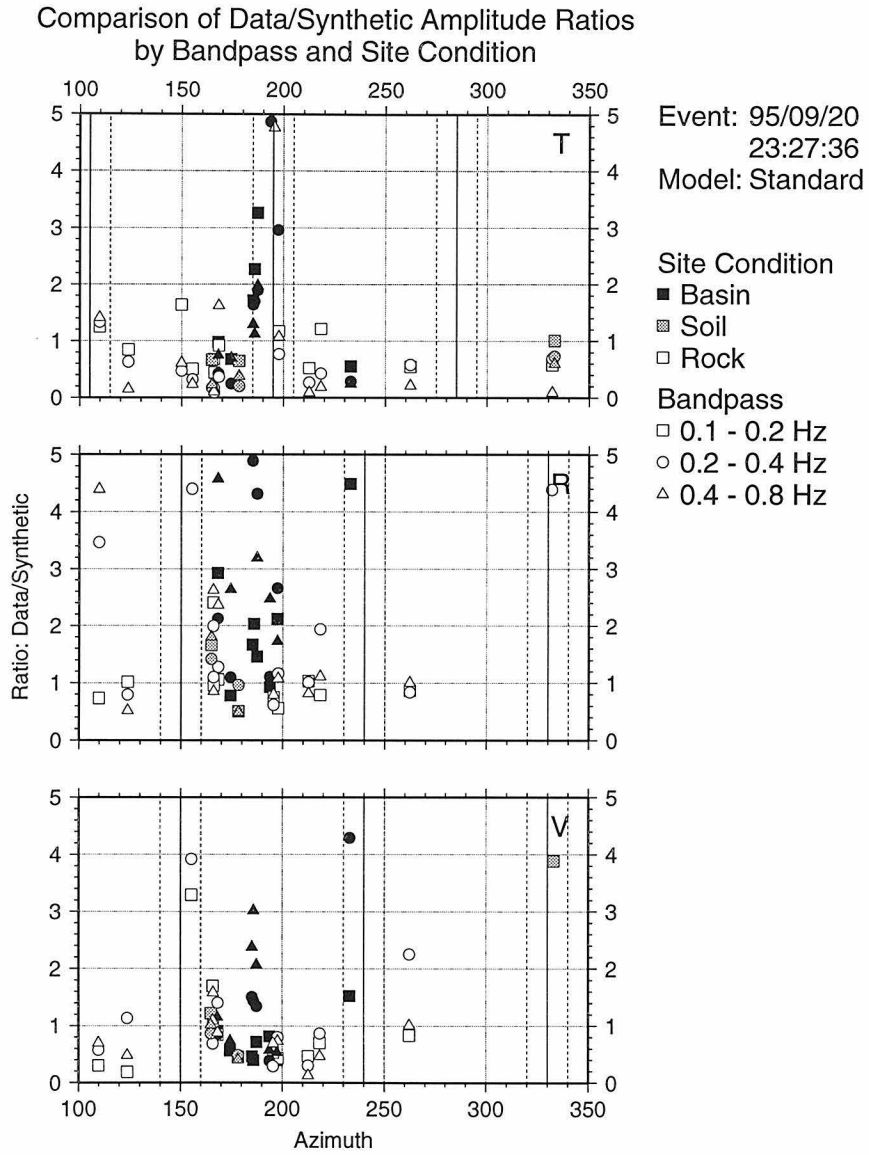
Figure 2.12: Ratio of data and synthetic maximum amplitude for the 95/09/20 event. Standard model used for synthetic waveforms at all sites. Basin/soil/rock sites indicated by black/grey/white symbols. Bandpass of 0.1-0.2/0.2-0.4/0.4-0.8 Hz indicated by square/circle/triangle symbol. Love and Rayleigh wave nodes in the source mechanism indicated by solid vertical lines ±10° from nodes indicated by dashed lines. The top plot is the tangential component, the center plot is the radial component, and the bottom plot is the vertical component.

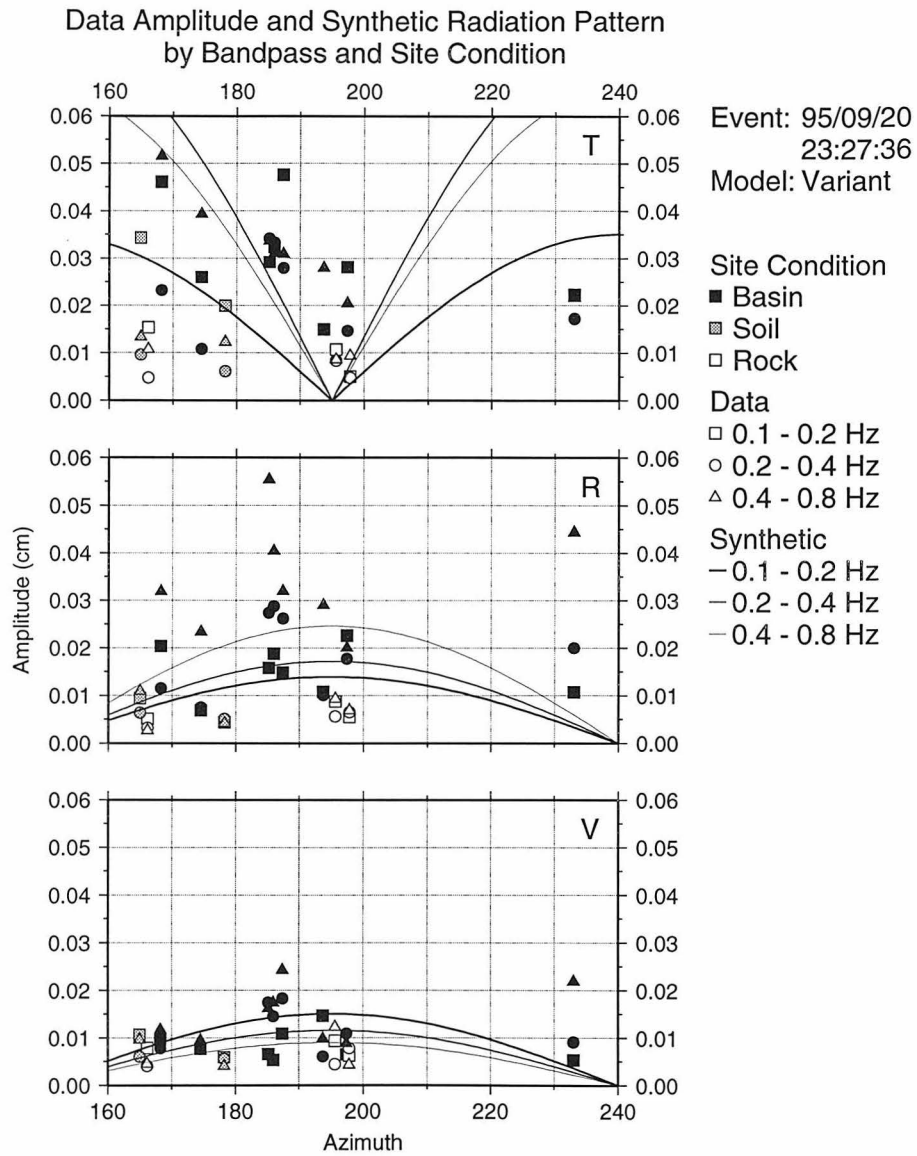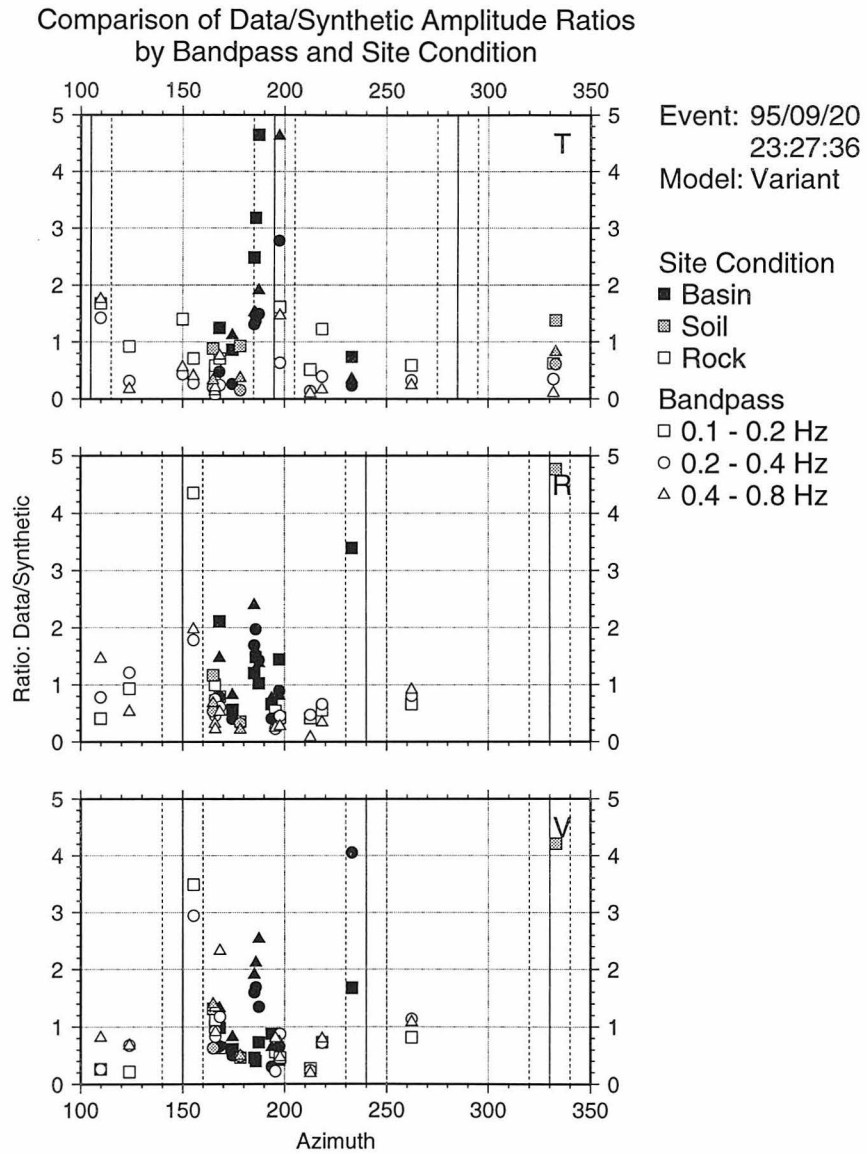Figure 2.13: Same as Figure 2.12, but synthetic waveform amplitudes are generated with the variant model.
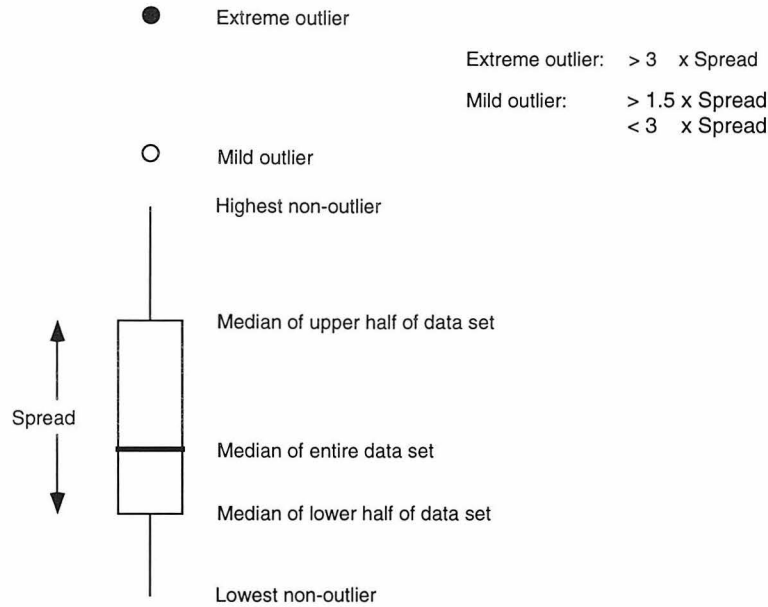
Figure 2.14: Boxplot construction and parameters. See text for detailed description.

The top and bottom of the box are the medians of the upper and lower halves of the data, respectively. The length of the box is the *spread* of the data, and it is used to define outliers in the data. A *mild* outlier is further than $1.5 \times spread$ from the top or bottom of the box. An *extreme* outlier is further than $3 \times spread$ from the top or bottom of the box. The vertical lines protruding from the box end are the highest and lowest non-outlier values. Mild outliers are indicated by open circles, extreme outliers by filled circles. The boxplot format was chosen because it presents the entire data set while indicating statistical features and the shape of the distribution. For the ratios of data/synthetic amplitude, the ratios tend to be skew and using mean and standard deviation as statistical measure obscures this. Also, the outliers are an important portion of the data for engineering applications. We label outliers and discuss them later in the paper.

Figure 2.15 shows the data from all three site conditions combined into one data set. When the standard model is used to calculate synthetic waveforms, the bulk of the distribution is down around 1, except the higher frequencies on the radial component. The scatter is large on the tangential and radial components. Use of

32
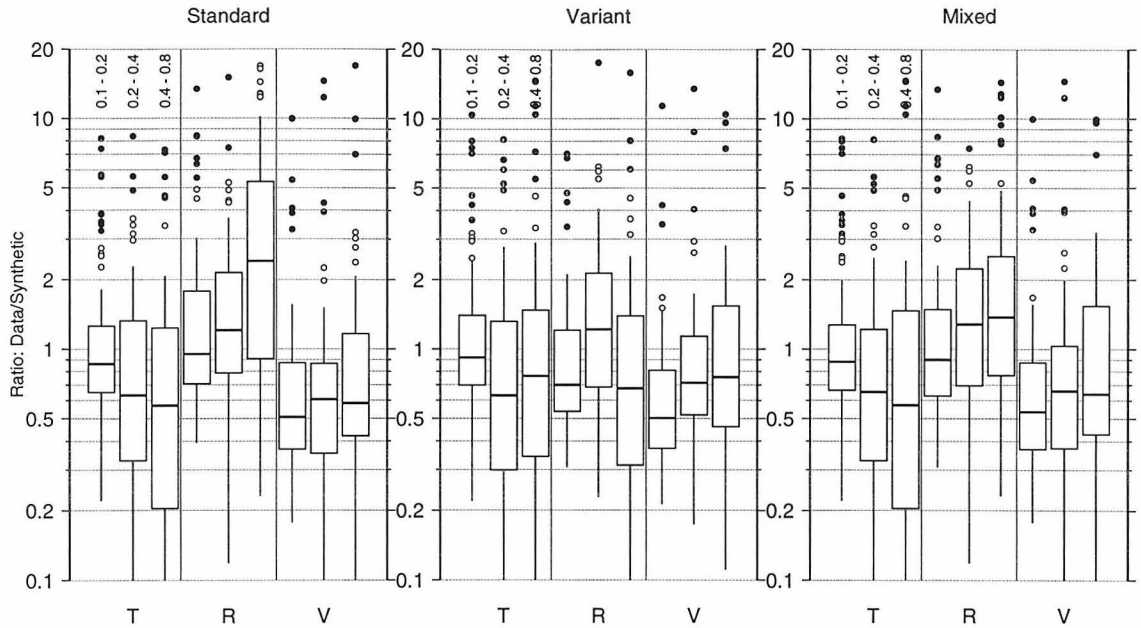
Figure 2.15: Boxplots of data/synthetic ratios for all data, at all sites which recorded the 95/08/17, 95/09/20, and 96/01/07 events. Separate statistics are shown for the 0.1-0.2, 0.2-0.4, and 0.4-0.8 Hz frequency bands. In the plot on the left, synthetic waveforms are generated with the standard model. In the plot in the center, synthetic waveforms are generated with the variant model. In the plot on the right, the standard model is used to generate synthetics for the rock and soil sites, and the variant model is used to generate synthetics for the basin sites.

the variant model synthetics in the ratios brings the median of the distributions on the radial component down around 1, but the scatter is not reduced much. It might seem that the variant model, with a 3 km thick top slow layer, should only be applied to the basin data. With this approach, the radial component ratio distributions are wider, with more outliers, than when the variant model is used for all the sites. This suggests that the variant model is preferable for all three site conditions.

In Figure 2.13, it is evident that ratios near nodes in the surface wave radiation pattern are unstable. Of course, amplitudes in synthetic waveforms may fall all the way to zero at nodes. The theoretical minima are less extreme when the radiation pattern has an oblique component. The correspondence of data with theoretical nodes depends on path complexities and multipathing.

When the sites near nodes are removed from the amplitude ratio data set (Figure2.16),
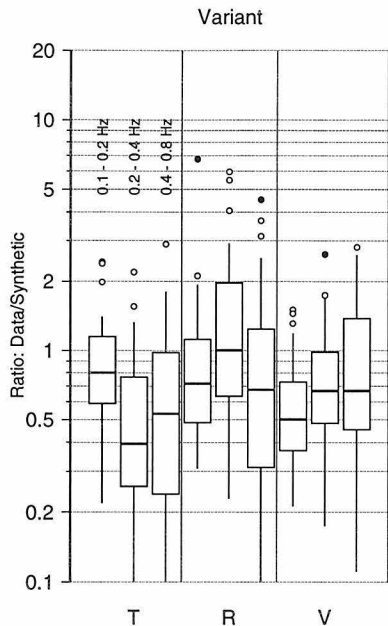
Figure 2.16: Same as Figure 2.15 except that data from sites within ±10° of source radiation nodes are removed. Outliers > 3 are labeled. The number after the station label is event the outlier corresponds to: (1) 95/08/17, (2) 95/09/20, (3) 96/01/07.

the number of outliers is significantly reduced. This is particularly true on the tangential component, which has a node in the Los Angeles basin area for all three sources. On this component, the spread of the distribution is also reduced. This implies that, away from nodes, the bulk of the data at all site conditions can be explained to within a factor of 2 by a 1D model. However, there are individual sites where the data amplitudes are more than 3 times greater than predicted by the synthetic waveforms.

If the majority of the outliers in the complete data set (Figure 2.15) can be explained by the insensitivity of the data to source nodes because of weak multipathing effects, then adding a "water level" to the source radiation pattern should have a similar effect on the distribution of ratios as removing sites near nodes. Adding a water level simply means forcing the synthetic amplitude used in the data/synthetic ratio to be at or above a percentage of the overall maximum amplitude of the synthetic waveform at all azimuths. A water level of 50% (Figure 2.17) has an effect similar to removing data within 10° of the nodes (Figure 2.16). Outliers exist on all three components and at almost all of the frequency bands examined, however, and this
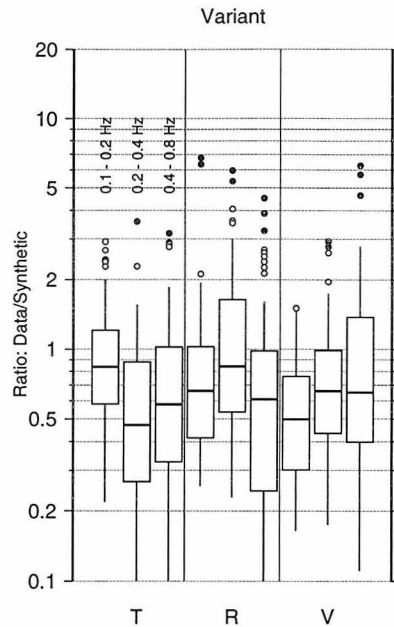
Figure 2.17: Same as Figure 2.15 except that a "water level" of 50% is applied to the radiation pattern of the synthetic waveforms. Outliers are labeled as in Figure 2.16.

suggests that there are sites where moderate amounts of multipathing cannot explain the data amplitude.

Next, we re-examine the data/synthetic ratios for each site condition independently to isolate amplifications at non-rock sites. Ratios from rock sites are shown in Figure 2.18. The distribution of the data/synthetic amplitude ratios is fairly compact. On the tangential and vertical components, the bulk of the ratios is at or below 1, with a few extreme outliers. There is more scatter on the radial component, particularly in the 0.4-0.8 Hz bandpass. Using the variant model in the ratios has the greatest effect on the radial component, reducing both the number of outliers and the spread of the distribution. On the tangential and vertical components, use of the variant model tends to spread out the distributions slightly. Removing data within 10° of source nodes (Figure 2.18b) reduces the number of outliers, in particular extreme outliers. The largest ratio of data to synthetic amplitude is less than 3. Applying a water level of 50% to the source radiation pattern (Figure 2.18c) has a similar effect to removing data around nodes, but there are extreme outliers at station SMTC.

Compared to the rock sites, the ratios of data/synthetic at the soil sites (Figure 2.19) have fewer outliers. The ratios for the radial component have wider distributions, particularly the 0.4-0.8 Hz bandpass, with higher median values. Use of the variant model synthetics in the ratios considerably narrows the distribution for the 0.4-0.8 Hz bandpass and reduces the median. It has little effect otherwise. It is worth noting that there is less data from soil sites than the rock and basin sites. There are 38 points, in each frequency bandpass, from rock sites, 13 points from soil sites, and 22 points from basin sites. This has the effect of reducing the number of outliers in the distribution, as defined for the boxplot, while having wide distributions. Removing data around nodes or applying a water level to the source radiation pattern (Figures 2.19b and 2.19c) has little effect on the distributions. The number of extreme outliers is reduced, and, when using the water level scheme, some of them are closer to the center of the distribution.

At basin sites (Figure 2.20), the distributions for all three bandpasses are relatively wide. Some of this is due to the location of the Love wave nodes for the three events. They fall on about the same azimuth, through the Los Angeles Basin, and a relatively high percentage of the basin sites are near these azimuths (see, for example, Figure 2.13). As with the rock and soil sites, the ratio distributions for the radial component are wider than for the vertical component, and higher frequency distributions are wider. Use of the variant model for the synthetics has a similar effect on the basin ratios as on the rock and soil sites, reducing the scatter on the radial component but having little effect on the tangential and vertical components. Removing data near nodes or applying a water level to the source radiation pattern (Figures 2.20b and 2.20c) has a significant effect on the results for the tangential component. This reflects the locations of the Love wave nodes. Even with nodes removed or the water level applied, there are still large outliers at SIO, SAN, FUL, and SBC.

Figure 2.18: (next page) The ratio of data to synthetic maximum amplitudes for rock sites. This is a combined dataset from the 95/08/17, 95/09/20, and 96/01/07 events. The plotting conventions are the same as Figures 2.15 to 2.17.
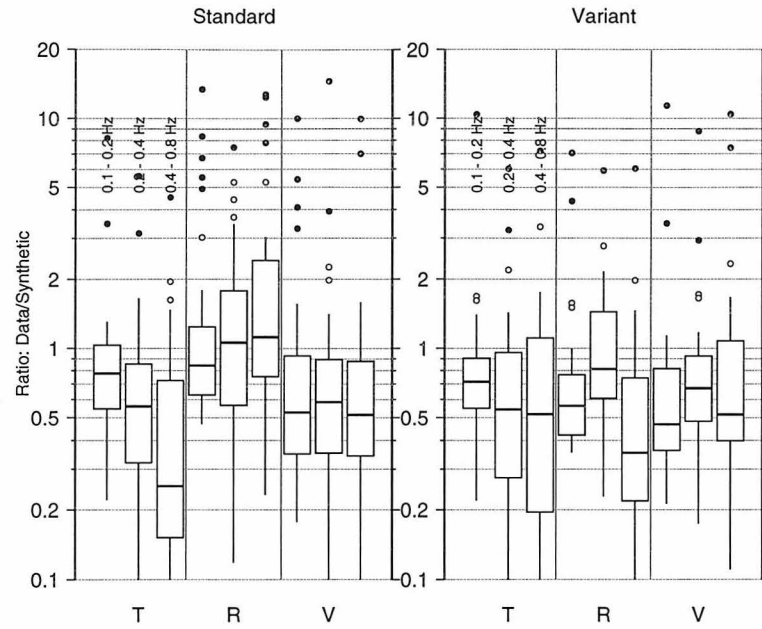
(a) Ratios with synthetics from standard (left) and variant (right) models
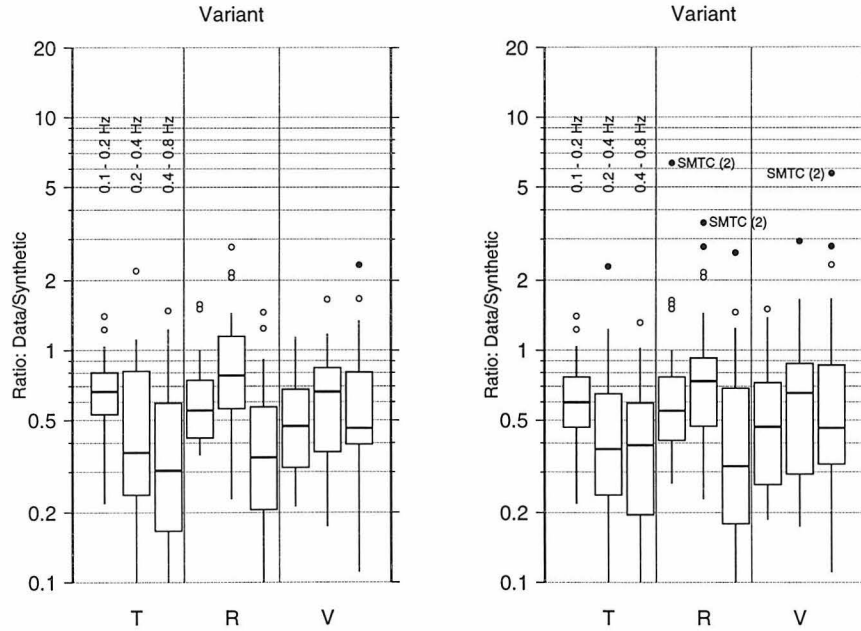
(b) Data removed within ±10° of source nodes

(c) Water level of 50% applied to source radiation pattern
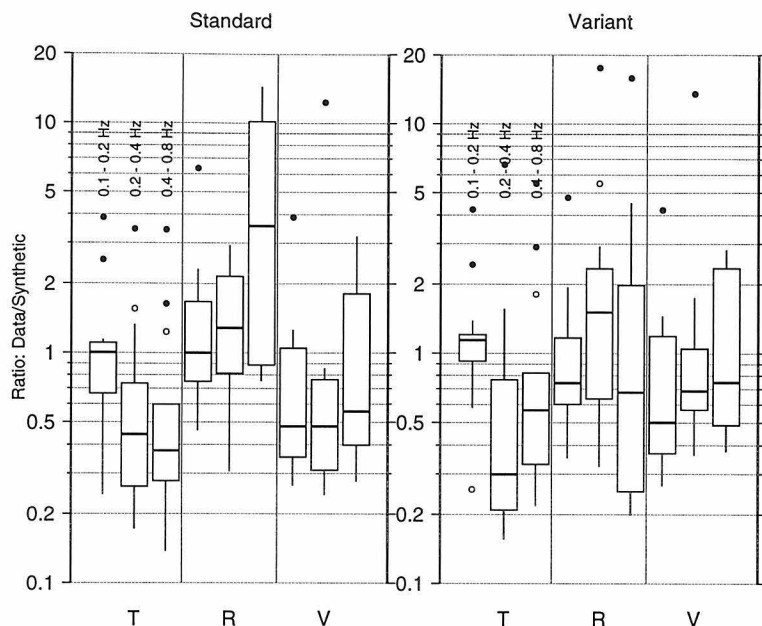
(a) Ratios with synthetics from standard (left) and variant (right) models
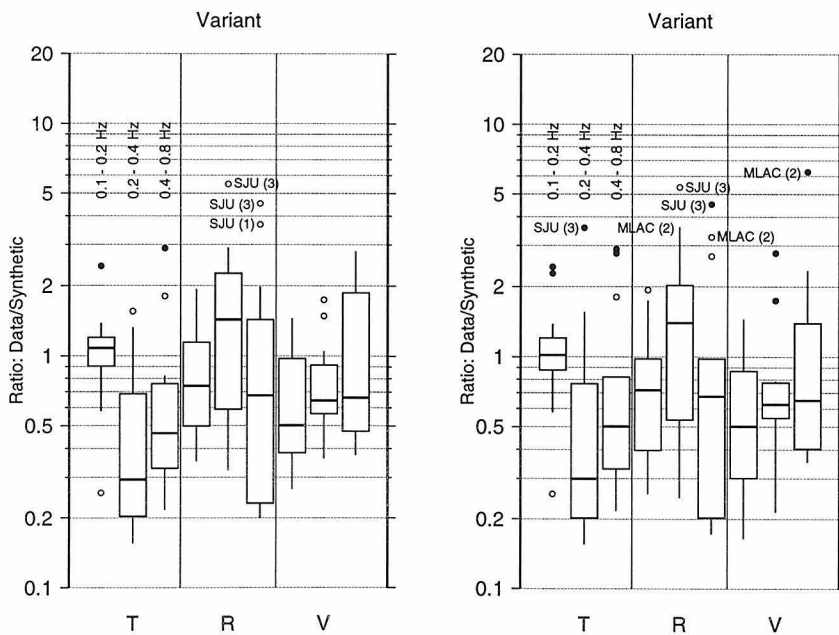
(b) Data removed within ±10° of source nodes

(c) Water level of 50% applied to source radiation pattern

Figure 2.19: Same as Figure 2.18 except that data is from soil sites.
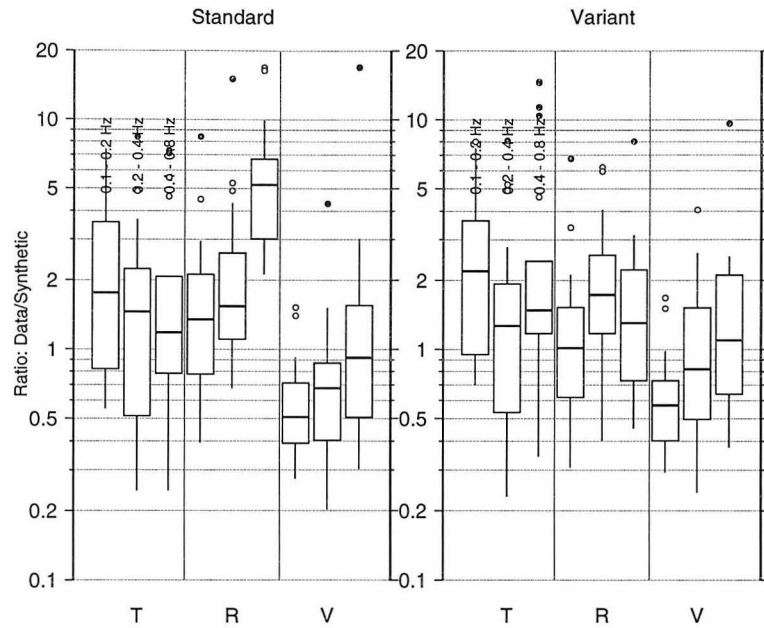
(a) Ratios with synthetics from standard (left) and variant (right) models
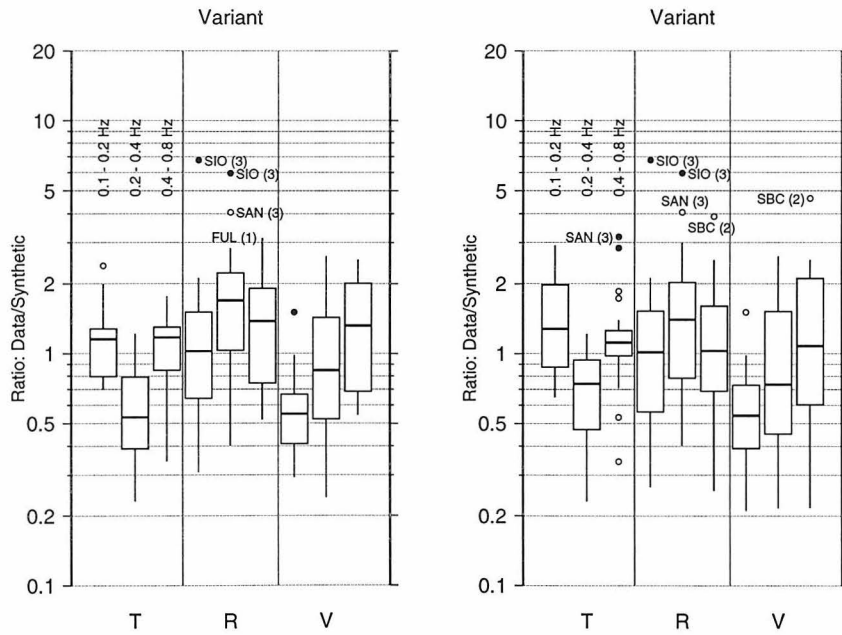
(b) Data removed within ±10° of source nodes

(c) Water level of 50% applied to source radiation pattern

Figure 2.20: Same as Figure 2.18 except that data is from basin sites.

A comparison of the rock and basin sites indicates that the rock sites tend to have lower amplitudes and show less variability than basin sites. With data around nodes removed, rock sites tend to have data/synthetic amplitude ratios at or below 1, in all three frequency bands. The largest outliers are less than 3. In fact, the synthetic amplitudes are often overestimations and ratios approach 0. Ratios at basin sites tend to fall between 1 and 2. With data around nodes removed, only a few outliers are larger than 3. The extreme outliers from SIO are as high as a factor of 9, however.

2.5 Discussion

When examining amplifications, outliers are quite significant, because they suggest that specific sites are so anomalous that they require special engineering concern or that a type of site condition or location is likely to receive stronger ground motions. A well known example is the Tarzana site which recorded high accelerations in the 1994 Northridge mainshock (1.8g). Other stations within 2 km of the site recorded significantly smaller accelerations. Two recent efforts to explain the amplification at Tarzana have argued for resonance of the (fairly subdued) topography of the hill where the instrument is set (Spudich *et al.*, 1996), and energy from a small landslide directly under the station, triggered by the mainshock shaking (Rial, 1996). Rial's model is the more exotic of the two, but Spudich *et al.'s* model creates more potential problems for seismic hazard mapping because it implies that subtle and common focusing effects may have to be taken into account.

In our data set, after nodal points are removed or a 50% water level is applied to the radiation pattern, ratios are greater than 3 at only a few specific stations: SMTC (rock), SJU and MLAC (soil), and SIO, SAN, FUL, and SBC (basin). MLAC is near a Rayleigh wave node, but when the water level is applied it is still anomalous. This site is in the unusual geologic environment of Long Valley Caldera which is likely to produce strong scattering of incoming seismic energy, and to trap seismic energy in slow near-surface materials. SAN, FUL, and SBC are at the surface of large sedimentary basins. SAN and FUL are at the southern end of the Los Angeles basin.

SBC is in the Santa Barbara basin. Earlier it was noted that SAN and FUL have large basin-generated surface waves, by comparison to a nearby soil station (Figure 2.6), but the anomalous amplitudes of the records, generating the outliers, are at high frequencies, rather than due to the longest periods in the surface waves.

Earlier we noted that waveforms at SMTC and SJU had a large, long period coda. Some of the ratios at these stations are also very large. These two stations are located just beyond the Imperial Valley and Los Angeles sedimentary basins, respectively. This suggest the large amplitudes and long codas can be explained as basin-generated surface waves leaking from the trailing edges of the basins. Bard and Bouchon (1980a) noted that basins with low velocity contrast to the background structure are ineffective at reflecting surface waves back into the basin. This appears consistent with the comparison of waveforms from SJU and stations in the southern end of the Los Angeles basin (SAN, OGC, and FUL). The amplitude and duration of the coda at SJU is very similar to that recorded at the basin stations.

We have already commented on the large, long period Rayleigh wave on the radial component at SIO. This record is the most anomalous in this data set because the amplification is long period and there is a large contrast between components at the same station.

Stations tend to have large amplitude ratios for one event but not the others. The only exception to this is station SJU which has outlier points for both event 95/08/17 and 96/01/07. There is the caveat to this, however, that not all stations recorded all three events (Figure 2.1). SJU didn't record 95/09/20, SIO only recorded 96/01/07, SMTC didn't record 96/01/07, and SAN didn't record 95/08/17. The correlation of outlier stations with specific events suggests a source effect in the generation of the large amplitudes. One possibility is that the amplitudes of basin-edge surface waves are relatively sensitive to incident surface waves which are themselves sensitive to source parameters, particularly near nodes. In this regard it is interesting that while FUL and SAN have outliers for different events, SJU has outliers for both those events. Since SJU is receiving leaked basin surface waves generated throughout the Los Angeles basin, the site may be less sensitive to nodes.

Authors	Basins	T (sec)	Ratio	Type
Rogers *et al.* (1985)	LA, SF	> 1	2-7	data spectral ratios
Qu *et al.* (1994)	LA	10	2-3 for 1D, 1-2 for 3D	data/synthetic ratio
Olsen *et al.* (1995)	LA, SF	5-10	up to 10	simulation spectral ratio
Teng and Qu (1996)	LA, SF, SG	3-10	up to 10	simulation peak amplitude
Wald and Graves (1997)	LA, SF, SG	2-17	3 in LA, 2.5 in SF	data basin/rock ratio

Table 2.3: Amplification factors for Los Angeles area basins found by other researchers from data and simulations. Listings are for sources sufficiently far from the basins that surface waves have developed before hitting the basin edge. Basin abbreviations are LA: Los Angeles, SF: San Fernando, SG: San Gabriel, .

Soil and basin amplitudes are generally elevated relative to rock site records, but the majority of soil and basin site amplitudes fall within 50% of the rock site amplitudes. This contrast is similar to values found by studies based on data, but less than those suggested by recent simulations of ground motion in basins (Table 2.3).

Rogers *et al.* (1985) examined spectral ratios of data from NTS nuclear explosions recorded in the Los Angeles and San Fernando basins. Qu *et al.* (1994) and Wald and Graves (1997) compare peak amplitudes in data from the Landers mainshock to ground motion simulations. The amplification factors listed for Qu *et al.* and Wald and Graves are based on only a couple points in each case, but they are consistent with the results we present here.

Spectral ratios found by Rogers *et al.* (1985) are higher than the peak amplitude ratios found by Qu *et al.* (1994), Wald and Graves (1997), and in our study. This reflects the long duration of basin-generated surface waves seen in basin sites. We chose not to work with spectral ratios because many of the basin station waveforms are cut off before the coda ends. Also, we could not use a single data record as the reference for the entire southern California region. As we have seen in this study, amplitudes at rock sites can fluctuate by a factor of 2, and waveform durations vary as well.

The simulations of Olsen *et al.* (1995) and Teng and Qu (1996) produce larger

amplifications in the Los Angeles basin than are seen in the data-based studies. Wald and Graves (1997) comment that instantaneous displacement in the fault slip model used by Olsen *et al.* (1995) may increase amplitudes by a factor of two. Teng and Qu (1996) simulate the 1857 Fort Tejon earthquake using source models with a few discrete asperities. They model only a narrow period band around 10 seconds. The maximum amplitudes occur for a source model with 3 asperities. The timing of the asperity ruptures is not stated, but their large amplitudes may be a result of constructive interference between the rupture timing and the period of the synthetic waveforms. Qu *et al.* (1994) used a similar lumped asperity source to model the Landers mainshock and found that their results were quite sensitive to the interference created by the source model. The largest amplifications seen in the simulations are quite localized, so the significance of comparisons with data from a few sites is uncertain. Our set of data may have missed points of extreme amplification in the wavefield. However, the pattern of amplifications in the simulations may depend on a combination of details of the source and path models that are unique to the simulation.

At some stations we see very clear basin-edge-generated waves (e.g., the comparison of PAS and KIK records for event 95/08/17 in Figure 2.5). In the PAS-KIK comparison,the basin waves appear to have been generated by a strong discrete pulse (visible at PAS) rather than an extended surface wave train. The discrete pulse has whiter spectral content than monochromatic surface waves, and so may excite basin waves where a harmonic wave might not because of mismatch with the basin preferred response frequency.

In the comparison of CRN with FUL, SAN, and OGC (Figure 2.6, a large, relatively long period surface wave generates secondary surface waves in the Los Angeles basin with about the same dominant period. However, in other locations there is little apparent basin response (e.g., HLN in the San Bernardino basin). Frankel (1993, 1994) has examined the response of the San Bernardino basin in 3D simulations and data from Landers aftershocks and found clear basin-generated surface waves. The dominant wave period in his records is about 2 seconds. In the Ridgecrest data, the

incident surface waves, as recorded at VTV and SVD, are about 10 second period waves. The difference between the frequency excited by the basin and the dominant surface wave frequency in Ridgecrest records may explain the lack of basin surface waves at HLN. The San Bernardino basin is a much shallower basin than the Los Angeles basin. Frankel's estimate of the deepest point is 1 km. The Los Angeles basin is up to 10 km deep.

Dispersion curves might be useful for understanding the frequency dependence of surface wave interaction with sedimentary basins and of basin-generated surface waves. Unfortunately, basin records in the data set presented here are too often cut short or affected by long period noise to retrieve clear dispersion relationships at longer periods ($>$ 6 seconds).

2.6 Conclusions

We are using synthetic waveforms generated with 1D models as a measuring standard to examine the variability of data throughout southern California. There is a greater variability in the amplitudes from basin site records than from rock sites records. Rock, soil, and basin sites are all rather insensitive to nodes in the horizontal radiation pattern. This complicates the analysis because the nodes create singularity points in the distribution of ratios of observed and synthetic amplitudes. In particular, a Love wave node runs through the Los Angeles basin area for all three events. When data near nodes are removed, the data at most rock sites have amplitudes within a factor of 2 of synthetic waveform amplitudes. Data from a few stations vary more (up to 3 times the synthetic amplitudes). Soil and basin stations vary more relative to the synthetic waveforms, with the bulk of the distribution at ratios less than 3 and a few outliers greater than 5. Soil and basin sites are also more often larger than the synthetics (higher median values).

In the Ridgecrest data set, most outliers can be explained by applying a water level of 50% to the radiation pattern. This reduces the scatter in the distributions to about the same extent as removing data within 10° of nodes. Thus, most of the

outliers in the data are sites that are insensitive to the nodes, not sites that are simply larger than any other data.

Of the remaining outliers, that are not explained by insensitivity to nodes, some are over the southern Los Angeles, the Santa Barbara, and the Ventura basins. Others are south of the Los Angeles and Imperial Valley basins. These sites indicate that basin-generated surface waves are propagating through the trailing edge of these basins.

Rayleigh waves on the radial component vary in amplitude more than surface waves on other components. Our initial 1D model under predicts the amplitude of the radial component at all types of sites. A 3 km thick slow layer improves the fit of the synthetic waveform amplitudes, particularly at higher frequencies, but the radial component still shows the most scatter.

Chapter 3

Ground Motions in the Los Angeles Basin from a Whittier Narrows Aftershock and the Sierra Madre Mainshock

3.1   Abstract

The proximity of several recent earthquakes to the Los Angeles sedimentary basin provides an opportunity to isolate the effects of the basin on wave propagation. The October 4, 1987 aftershock ($M_L = 5.3$) of the Whittier Narrows sequence and the June 28, 1991 Sierra Madre mainshock ($M_L = 5.8$) are on a similar azimuth to stations overlying the deepest part of the basin. A distinctive feature of records from basin stations recording the October 4th aftershock is the large amplitude of multiple S, SS, etc. The multiples have up to twice the amplitude of the direct S phase on the tangential component. At such a short range, less than 25 km, a horizontal seismic velocity gradient is needed to turn rays rapidly enough for large amplitude multiples to form. A forward modeling approach is employed, using finite difference numerical techniques that produce double couple point source solutions. A model based on a recent geologic cross-section constructed for the east edge of the Los Angeles basin generates more phases than are seen in the seismic records. Simpler models, based on dipping layers with low shear velocities in the top few layers, fit the data better. The seismic velocity, depth, and dip of the layers are varied to fit the timing between the direct P, the direct S, and the first S multiple. The timing and amplitude of the direct and first multiple S pulses is well modeled, though the phase of the first multiple does not match the data. Including a steeply dipping west edge in the basin

model has little effect on the synthetic waveforms except at distances near that basin edge. The amplitude of SS is greatest in the deepest part of the basin, where it is 2 times larger than direct S. The coda duration increases from 8 seconds to more than 20 seconds from the NE to the SW. The Sierra Madre mainshock occurred about 25 km to the NE of the Whittier Narrows sequence. The model for Whittier Narrows was extended to this distance, with a shallow basin between the Whittier and Sierra Madre hypocenters to simulate the San Gabriel sedimentary basin. Phases generated by the edge of the deep basin continue to dominate the synthetic waveforms, but this model generates a lengthy coda. This study shows that specific phases with frequencies up to 1 Hz that have traveled through deep sedimentary basins, and can be explained by two-dimensional seismic velocity models.

3.2   Introduction

Events such as the 1985 Michoacan earthquake have dramatically demonstrated that it is important in seismic hazard analysis to understand the effects of sedimentary basins on the propagation of seismic energy (Anderson *et al.*, 1986; Campillo *et al.*, 1989; Kawase and Aki, 1989). There are a number of other areas in the world, including Los Angeles, where large populations live on or near sedimentary basins. Parts of the Los Angeles sediment-filled basins extend as deeply as 9 km (Yerkes *et al.*, 1965; Davis *et al.*, 1989). The geometry of the Los Angeles basin is shown in Figure 3.1. There is long-standing concern about the effect of this basin on the amplitude and duration of shaking that will be felt in the Los Angeles area as the result of a large earthquake on the San Andreas Fault. In addition, there is concern about damaging events in the Los Angeles area itself. This concern was originally produced by the 1933 Long Beach earthquake on the Newport-Inglewood fault zone, and has been raised again by recent quakes on blind thrusts adjacent to the basin (Hauksson, 1990).

Waveforms recorded in sedimentary basins are affected by the three-dimensional structure of the basin. The effect is minimized for recordings of teleseismic events;
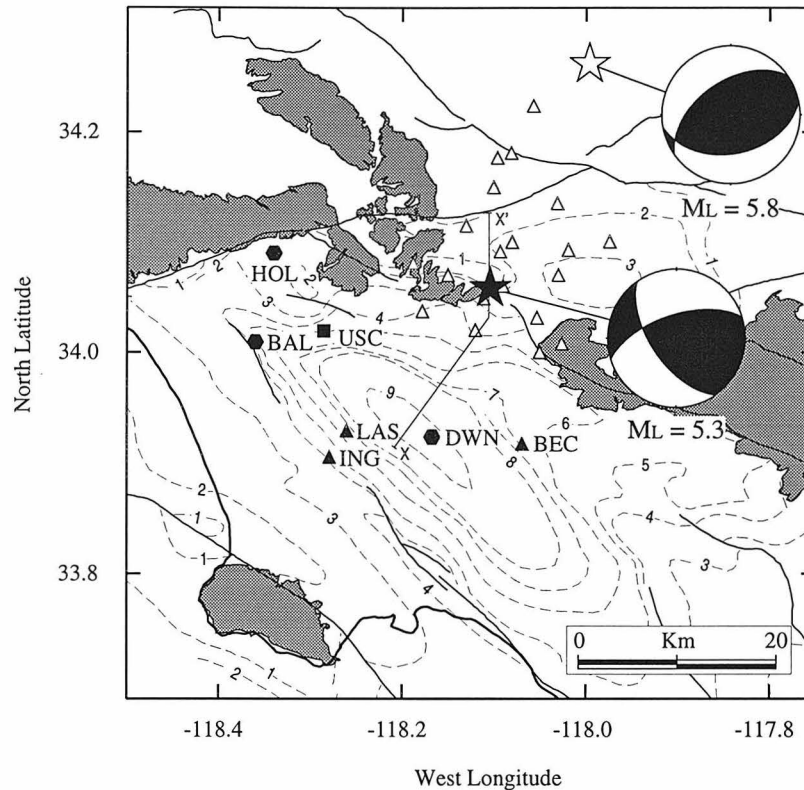
Figure 3.1: Map indicating the epicenters and focal mechanisms of the October 4, 1987 Whittier Narrows aftershock and the June 28, 1991 Sierra Madre mainshock with the surrounding seismic stations. The Whittier Narrows aftershock is the black star and the Sierra Madre mainshock is the white star. The shaded portions of the focal mechanisms are compressional. Triangles, squares and hexagons indicate seismic station locations. The black symbols are for stations that are used in this study. Hexagons indicate records that are available for both events (stations DWN, BAL and HOL). The black triangles indicate stations BEC, LAS and ING for which only Whittier Narrows aftershock records were used in this study. Only a record for Sierra Madre was available from station USC (the square). The stippled regions of the map are the hills surrounding the Los Angeles basin. The solid lines indicate a few of the significant faults in the region. The dashed contours indicate the depth in kilometers (below sea-level) to crystalline rock in the Los Angeles sedimentary basin (from Yerkes *et al.*, 1965). The line X-X' through the Whittier Narrows area is the location of the cross-section in Davis *et al.* (1989) on which the model in Figure 3.5 is based.

body waves arrive with near-vertical incidence through the bottom of the basin, and long-period surface waves average out basin effects with the surrounding structure. Even so, "site response" has a significant effect on these waveforms. Near-field events interact strongly with the basin edge (the interface between basement rocks and compacted sediments). This interface can be curved tightly enough to introduce three-dimensional multipathing effects. In addition, the bottom of the basin is likely to be irregular and stratigraphic units, which may roughly correlate with the seismic velocity structure, may be folded or tilted. Synthetic waveforms based on three-dimensional velocity models of sedimentary basins have been generated (Frankel and Vidale, 1992; Graves and Clayton, 1992), and these results confirm the effectiveness of the basins for trapping seismic energy, increasing peak amplitudes and extending the waveform coda. Comparisons between synthetic waveforms and data in these studies, however, are based on the similarity of the general shape of the envelope of the waveforms, on patterns of peak accelerations for the distribution of stations, or on the similarity of parameters derived from the synthetic waveforms to empirical relationships. Attempts to model specific phases in data have not been made with three-dimensional structures because the number of parameters to vary in the velocity models is immense and the cost of generating synthetic waveforms is prohibitive.

Even with one-dimensional models, it is possible to successfully forward model some phases in seismic data from receivers in sedimentary basins. Modeling the polarity and amplitude of the direct arrivals is an example. Figure 3.2 shows the fit of velocity data and synthetic waveforms for the direct S arrival from the large October 4, 1987 aftershock of the Whittier Narrows sequence on tangential component records at strong motion stations in the San Gabriel and Los Angeles basins. The reversal of polarity of the direct arrival across radiation pattern nodes is clear in the data set. However, the amplitudes of the phases at nodal stations do not fall off to values as low as is theoretically expected. Examples of this are SAG and ELM in the San Gabriel basin. This suggests that multipathing effects of the basin average out amplitude variations at the nodes. The one-dimensional model only predicts the direct phase well. It does not produce multiples like those seen in the data at stations
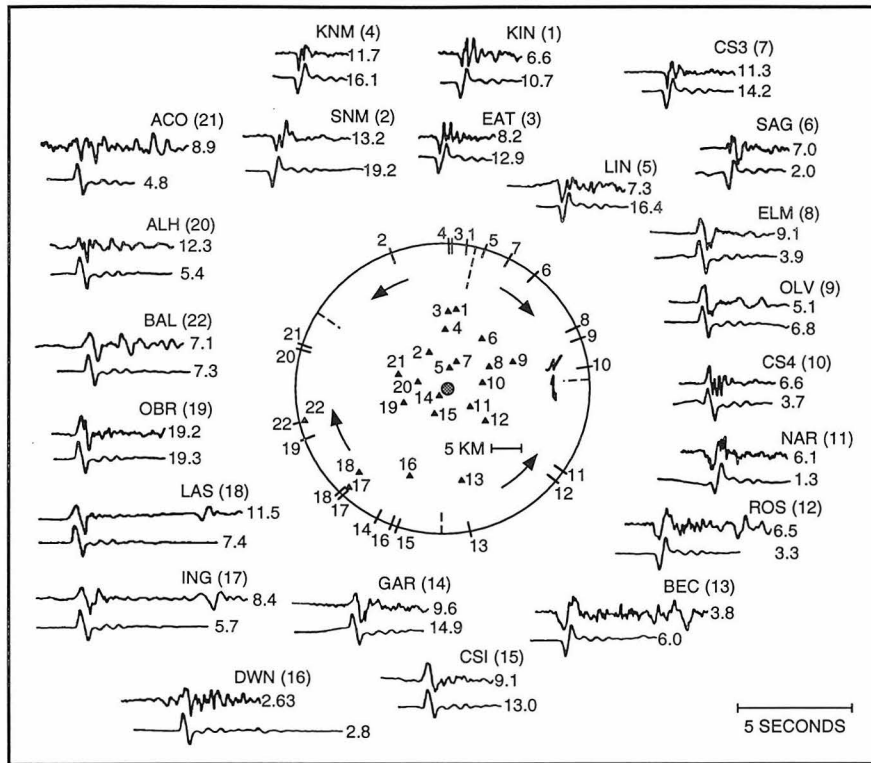
Figure 3.2: Comparison of data and synthetic waveforms generated with a flat layer model. The relative station locations are plotted in the circle and the aftershock epicenter is located at the center of the circle. Dashed lines are approximate nodal planes as indicated by the first motion polarity of the data. While the polarity changes are clear, the peak amplitudes of the data from stations near the nodal planes do not drop to the low values predicted by the synthetic waveforms. The synthetic waveforms were made using the one-dimensional model of Saikia (1993).

LAS, ING and BEC in Figure 3.2.

Since a one-dimensional velocity model can fit the direct S arrival, it is reasonable to expect that some other phases can be fit by the two-dimensional structure along the azimuth between the epicenter and the receiver. One way to assess the appropriateness of a two-dimensional velocity structure is simply to see how cleanly the horizontal components of the seismogram rotate into the radial-tangential orientation. If seismic energy is arriving off-azimuth, then the tangential component will have significant P-wave amplitudes. However, polarization analysis, such as that suggested by Vidale (1986), provides a clearer picture of the directions from which

energy is reaching the receiver when an arrival is separated in time from other arrivals. Vidales method gives quantitative values of the strike (relative to the back azimuth) and dip of the plane of maximum polarization of incoming waves, rather than the more qualitative indications of waveform polarization found in particle motion plots.

A two-dimensional model is only directly applicable to a particular cross-section. If data from multiple stations, situated over a range of azimuths from the source, are to be modeled, then the model will correspond to an average structure across the azimuth range. Also, a two-dimensional model cannot reproduce three-dimensional multipathing effects on the propagation of seismic energy. In counterbalance to these limitations of two-dimensional models, the computation of synthetic waveforms in two dimensions is faster and cheaper than in three dimensions. More iterations can be made to develop a model. A three-dimensional model produces an overall picture of how seismic energy propagates through an area. However, such a model is based on sources of information, such as seismic reflection lines, well data, and geological structural models, that are of limited density and resolution. This may result in a model that overlooks a significant aspect of the seismic energy propagation through the structure. Thus, two-dimensional modeling can be used to fine tune cross-sections through three-dimensional models and help constrain the models as a whole.

3.3   Method

The two earthquakes discussed in this paper are the October 4, 1987 Whittier Narrows aftershock ($M_L = 5.3$) and the June 28, 1991 Sierra Madre mainshock ($M_L = 5.8$). A location map is shown in Figure 3.1. The October 4 event was the largest aftershock in the Whittier Narrows sequence, but it was a much simpler event than the October 1 mainshock. The aftershock was predominately strike-slip; the mainshock was almost pure thrust. The entire sequence took place directly adjacent to the Los Angeles basin and was associated with the Elysian Park Thrust (Hauksson, 1990). This sequence was a clear indication that such blind thrusts need to be considered in seismic hazard assessments for the area. The June 28, 1991 Sierra Madre mainshock was 25 km

further away from the edge of the Los Angeles basin than the Whittier Narrows sequence, and the shallow San Gabriel basin lies in between. It was, however, at about the same azimuth from stations in the Los Angeles basin as the Whittier Narrows sequence. This allows us to extend the model further back from the basin, and look at how the effect of the basin affects waveforms as the source is moved away from the basin's edge.

We first work with data from six stations in the Los Angeles basin area for the Whittier Narrows aftershock (Figure 3.3). All three components of data are available from each of these stations. The stations LAS, ING, DWN, HOL and BAL are California Strong Motion Instrumentation Program, Division of Mines and Geology (CDMG) instruments (Shakal *et al.*, 1987). The sensors record acceleration with free periods of about 0.0395 sec and damping coefficients of around 0.59. The response is flat in acceleration to about 10 Hz. The raw acceleration has been resampled to a rate of 50 samples per second and bandpass filtered with ramps of about 0.3-0.6 Hz and 23.0-25.0 Hz during CDMG processing. The BEC station is a GEOS instrument installed and maintained by the U.S. Geological Survey (USGS). The nominal parameters for this instrument are a free period of 0.02 sec, and a damping coefficient of 0.7 (Mueller *et al.*, 1988). This results in a response that is flat to acceleration out to about 20 Hz. The BEC station is at an azimuth to the southeast of the others, where the basin is about 7 km deep. Both the BEC and DWN stations are at 16 km distance from the epicenter of the October 4 aftershock. Stations HOL and BAL are on the north rim of the basin where sediments are relatively thin. The ING and LAS stations are near the Newport-Inglewood Fault Zone at the west edge of the Los Angeles basin. Only station DWN lies over the deepest Los Angeles basin.

The records from these stations, except for HOL and BAL, contain a very strong phase on the tangential and radial components 5 to 6 seconds after the direct S arrival. Complex polarization analysis (Vidale, 1986), an example of which is given in Figure 3.4, shows that on the records from DWN, BEC, ING and LAS the dip of the polarization plane of this phase is close to 0° and the strike is more than 60° away from the back azimuth. This is consistent with a shear wave arriving on azimuth from

October 4, 1987 Whittier Narrows Aftershock, Velocity Data
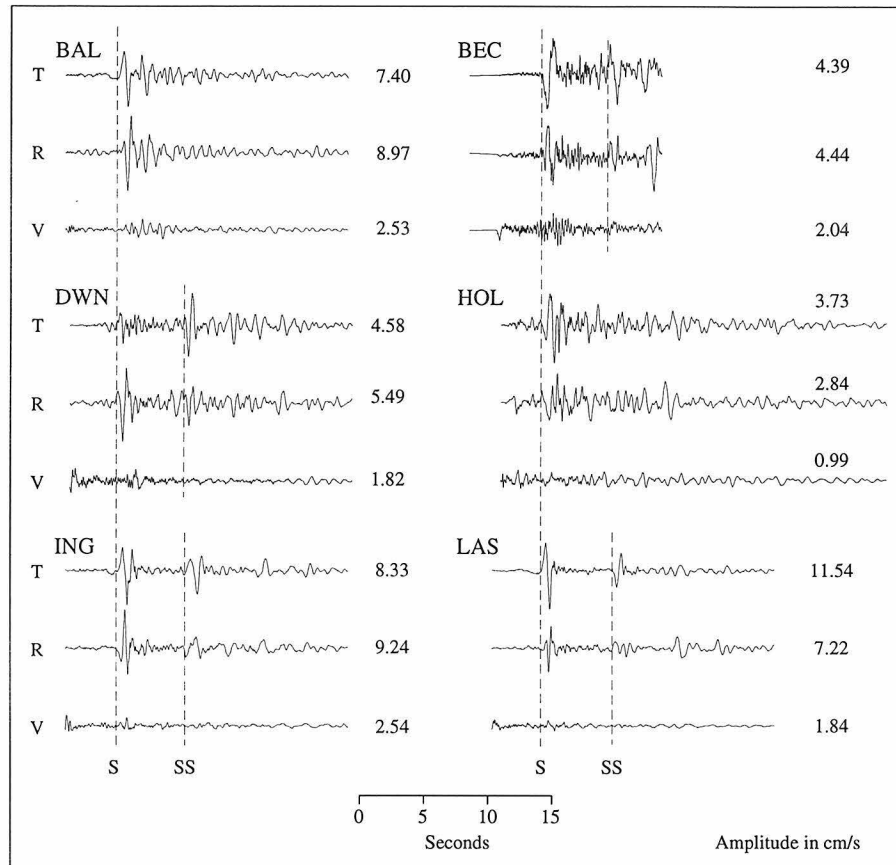
Figure 3.3: Three component velocity records from six stations in the Los Angeles basin for the October 4, 1987 Whittier Narrows aftershock. The strong shear wave multiple is evident in the tangential components at the stations near the central basin. DWN, ING, LAS, BAL and HOL are instruments maintained by the California Division of Mines and Geology (CDMG). BEC is a USGS Geos station. Amplitudes are in centimeters per second.

the source, without heavy contamination by energy refracted from other parts of the basin. On the DWN tangential velocity record this phase is more than two times larger than direct S pulse. We argue that this phase is appropriately modeled as a first multiple (SS) off the bottom of the basin of the direct S ray, that its appearance in the records is dependent on the seismic structure of the edge of the sedimentary basin, and that it therefore can be approximately modeled with a two-dimensional velocity structure.

To work with two-dimensional velocity models, we have generated the synthetic waveforms by a finite-difference formulation described by Vidale *et al.* (1985). In this approach, the SH and P-SV systems are decoupled and solved separately. It is based on using known first-term asymptotic solutions for double-couple sources to introduce pseudo-near-field terms, which produce the appropriate radiation patterns for a point source with two-dimensional codes. These asymptotic approximations break down for long periods because of the neglect of near field terms. Also, the grid used in the finite-difference modeling introduces high frequency dispersion, with the severity of this effect controlled by the size of the grid elements. As a result, the synthetic waveforms produced are inherently band-limited. In this study, the synthetics have been bandpass filtered to minimize the long period and high frequency artifacts. The calculations are appropriate for a line source perpendicular to the two-dimensional cross-section and point source solutions are generated from these by a simple transformation (Helmberger and Vidale, 1988).

One approach to modeling the data is to use a geologic cross-section as a starting point. We have constructed a model directly from the cross-section developed by Davis *et al.* (1989) that passes through the Whittier Narrows area (Figure 3.5). The position of this cross-section is shown as the line X-X' on the map in Figure 3.1. Calculations for this model with the two-dimensional finite difference code with a double-couple source at the depth and location relative to the edge of the basin that are appropriate for October 4th event result in synthetic waveforms that are much more complex than the data. It is apparent that this model needs to be smoothed to fit the data. We start from a simple one-dimensional seismic velocity model and
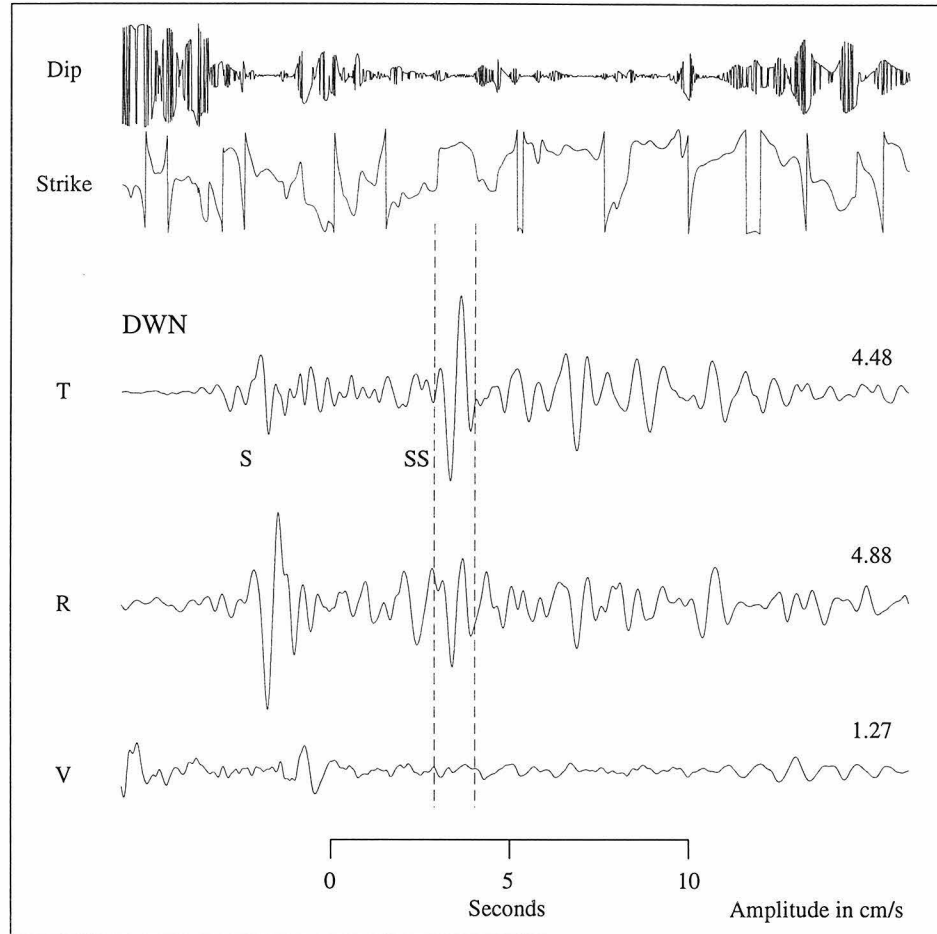
Figure 3.4: An example of complex polarization analysis (Vidale, 1986) discussed in the text. The analysis is for station DWN. The velocity data was lowpass-filtered with a corner at 4 Hz frequency prior to the analysis, in order to smooth the results. The dip and strike relative to the backazimuth of the polarization plane are shown as a function of time and range from $-90°$ to $90°$. A portion of the record around the multiple phase that is being modeled is shown by dashed lines. In this portion of the record the strike of the polarization plane is close to $90°$ and the dip is about $0°$. This is consistent with the arrival at the station of a near-vertical SH ray. The large and rapidly fluctuating values for the dip at the beginning of the time series are artifacts of the low amplitude of the horizontal components prior to direct S.

tried to construct a simple two-dimensional model that satisfies the data. We use a deterministic forward-modeling approach to satisfy the clear signals in the data.

3.4   Results

Our preferred model fits the relative amplitude of the SS and S phases, S- P times for the data, and absolute S and P times (for those stations where they are available). The fit is best for the stations over the deep basin (DWN, BEC and LAS). The modeling was done primarily for the SH system because P-SV waveforms are more expensive to synthesize and more complicated to treat, due to conversions between P and S energy at interfaces. For the best fit model, however, we also calculated radial and vertical synthetic waveforms.

The finite difference code calculates synthetic waveforms for the fundamental fault orientations. For the SH system, this is vertical strike-slip and vertical dip-slip (Figure 3.6). In the corresponding synthetics, the multiple is clearly present for both fault types. However, the strike-slip fault orientation produces a lower amplitude multiple than is needed. The dip-slip synthetics have very strong multiples, and this suggests that the strength of this multiple in records such as DWN is due to the small dip-slip component of the aftershock source mechanism. Synthetic waveforms are compared with the velocity data in Figure 3.7.

An emphasis was placed on fitting the records from station DWN (see Figure 3.8) because DWN is the only station in the data set over the deepest part of the Los Angeles basin and the multiple on the tangential component is particularly strong for this station. Unfortunately, the trigger time was not recorded by the DWN station, so the data and synthetic waveforms are lined up by the direct S arrival on the tangential component. The dashed line indicates this point for all the waveforms. The amplitude scale for the synthetic waveforms is about twice that of the data when a $M_0 = 5 \times 10^{23} dyn - cm$ is used to construct the synthetics. The tangential component has the best fit of synthetic to data among the three components. The relative timing and amplitude of the SS and S arrivals in the data are well matched in the synthetic.
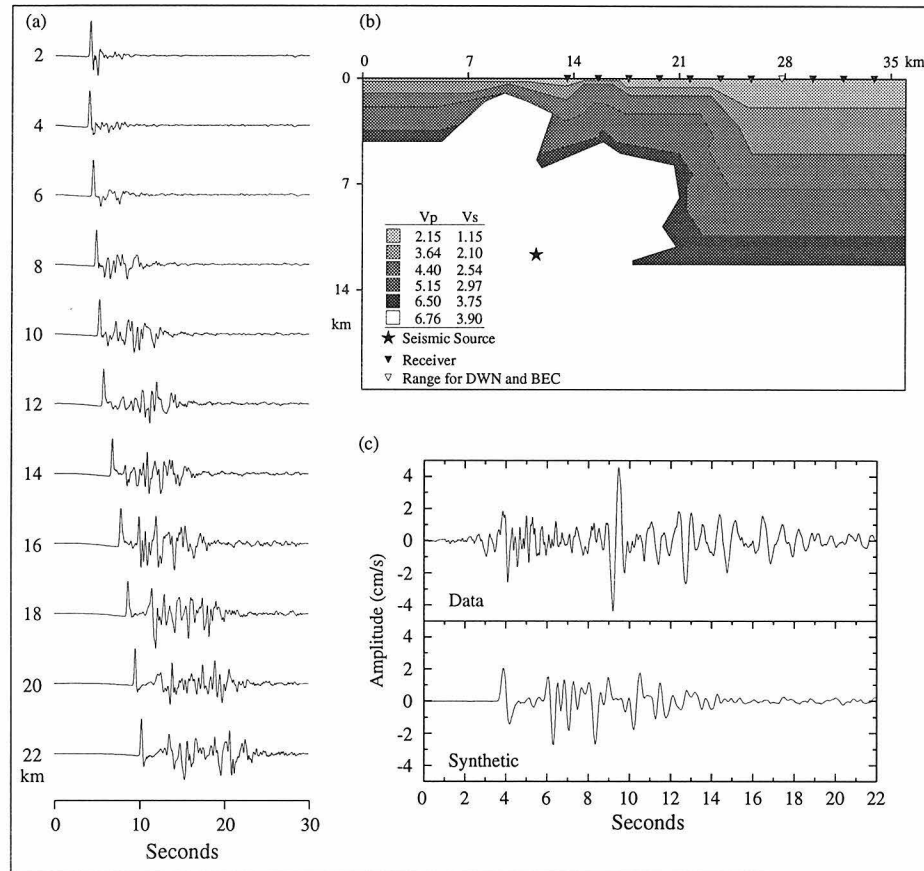
Figure 3.5: (a) Finite-difference synthetics of the tangential displacement component for the October 4, 1987 Whittier Narrows aftershock along the DWN azimuth for distances from 2 to 22 km. The source mechanism used to construct these synthetics is from Saikia (1993). (b) The seismic velocity model used to calculate the synthetics in this figure. The velocity structure is an attempt to directly incorporate the geologic cross-section of Davis *et al.* (1989). Velocities are given in kilometers per second. NE is to the left in this figure. (c) A comparison of the tangential component data from station DWN with the velocity synthetic at the correct range from the source (16 km). The two waveforms are lined up on the direct S phase. A source with $M_0 = 5 \times 10^{23} dyn - cm$ was included in the synthetic waveforms.

There is also a suggestion of an additional multiple 4 seconds after SS in both the data and the synthetic which would correspond to SSS. The radial component of the data has more phases than are found in the synthetic. One reason for this may be that P to S conversions at the edge of the basin are not strongly generated by this model. The P wave velocities in the model are only crudely established, and the homogeneity of the P velocity in the top of the model is certainly not accurate. The SS phase in the data is larger than the multiple in the synthetic, and the additional multiple (at 12-13 seconds) is present in the data but not the synthetic. This suggests that SH energy is being turned onto the radial component by the three-dimensional structure of the basin, but not so strongly that it obscures the two-dimensional propagation of most of the energy. The vertical component is much lower amplitude in both the data and the synthetic. It is interesting to note that the direct S phase is not visible on the vertical component of the data. This indicates that the direct shear wave is arriving with vertical incidence. The dashed line in Figure 3.8 indicates where direct S arrives on the radial and tangential components. The phase coming in 5-6 seconds after the trigger on the vertical component is probably a converted S to P multiple phase. The vertical synthetics have both the direct and the converted phase. This suggests that the shallow shear wave velocities in our model are not slow enough to turn the direct S ray to vertical incidence.

Trigger times are known for three of the six available stations, ING, LAS and BAL. The data and synthetic waveforms for these stations are compared in absolute time in Figure 3.7. The trigger times for stations BEC, DWN and HOL are not known. The data and synthetics for these stations are lined up on the direct S of the tangential component. As mentioned before, the modeling in this study was primarily

Figure 3.6: (next page) Finite difference tangential component synthetics for two fundamental fault mechanisms produced by the basin-edge structure at the top of the figure. NE is to the left in this figure. Seismic velocities are given in kilometers per second. Note the large amplitude multiple in the pure dip-slip synthetics for ranges 14 to 22 km. The slight ringing after the direct S phase is a numerical artifact (grid dispersion) of the finite-difference program.

Vp	Vs
3.00	0.95
3.00	1.35
3.00	1.90
3.81	2.30
4.33	2.60
4.85	2.90
5.20	3.10
6.41	3.70
6.76	3.90

★ Seismic Source
▼ Receiver
▽ Range for DWN and BEC

Strike Slip

Dip Slip

Range (km)

Seconds
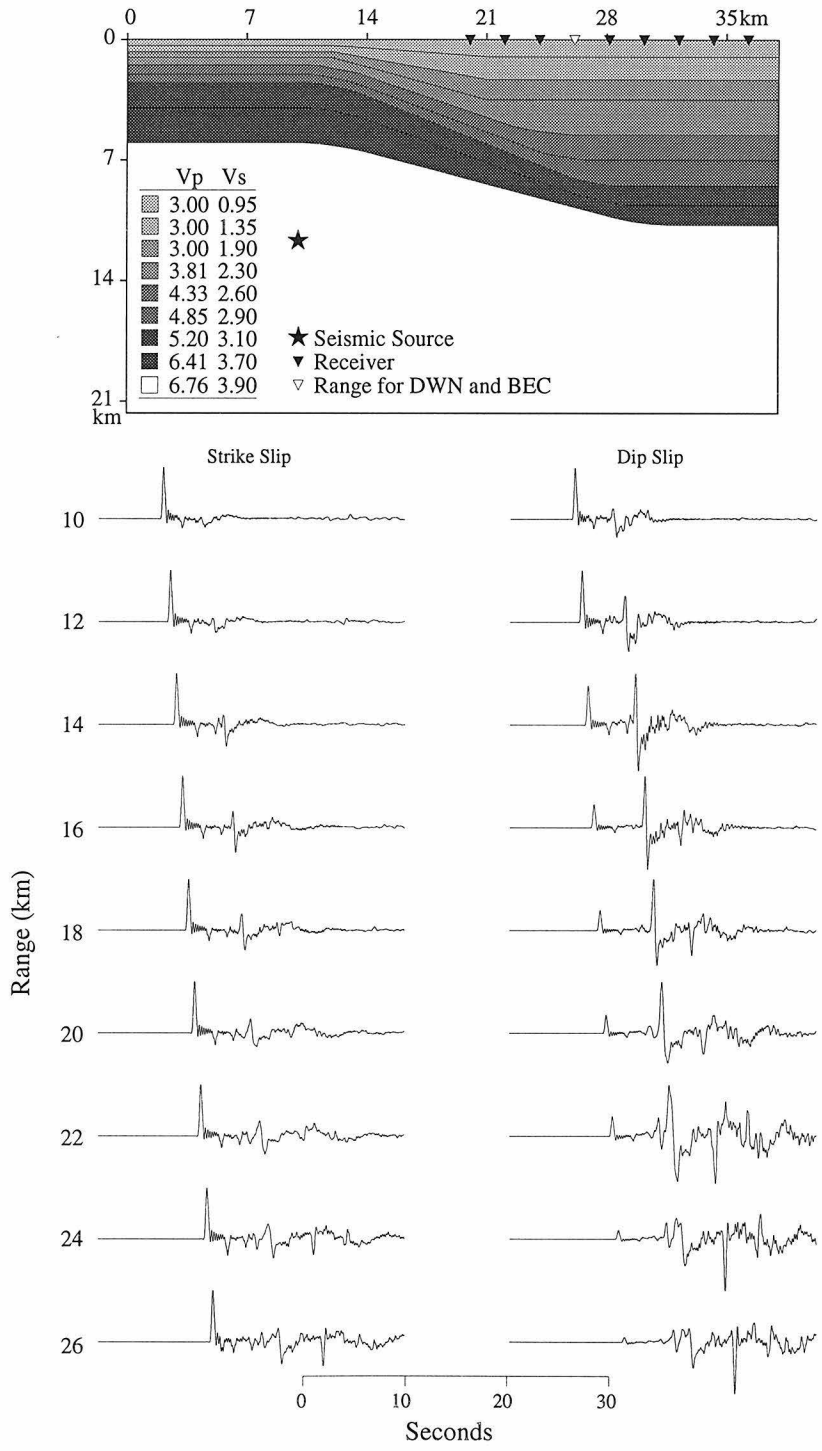
done on the tangential component, to avoid the cost and added complexities of fitting the P-SV system. In addition, the model cannot hope to fit all the data on azimuths from 169° to 279°; the contours of basin depth in Figure 3.1 indicate the differences in the cross-sections from the hypocenter to each station. The stations DWN, ING and LAS are on azimuths for which the propagation path should be similar. The absolute timing of the direct S for ING and LAS are within a second of the data. The relative timing of the SS and the direct S arrivals for stations DWN and LAS are quite good. However, the synthetic for ING does not predict a strong SS arrival, though the data for this station has a clear signal. The absolute amplitude of the whole waveforms and the relative amplitudes of the SS and S arrivals on the synthetics are fit within a factor of 2. The relative phase of the SS arrival to that of the direct S is not well predicted by the synthetic waveforms. The synthetic SS is consistently shifted 90° in phase relative to the direct S, as expected. The data for stations DWN and LAS suggest that the multiple is 180° out of phase with the direct S arrival. The SS arrival in the data at station ING, however, seems not to be phase-shifted at all relative to the direct S. Stations BEC, BAL and HOL are on azimuths from the hypocenter that do not cross the deepest portion of the basin. Of the three, BEC is over the deepest sedimentary layer, and there is a large amplitude multiple on the data for this station while there is not for the other two. However, the synthetic waveforms for these azimuths do not predict large multiples, so it is unclear whether such multiples are missing from the data because of the shallow basin structure or because of the

---

Figure 3.7: (next page) Comparison of velocity synthetics, produced by the preferred model shown in Figure 3.6, with October 4, 1987 Whittier Narrows aftershock data. Both data and synthetics have been bandpass filtered between 0.1 and 3 Hz. A source with $M_0 = 5 \times 10^{23} dyn - cm$ was included in the synthetic waveforms. (a) Comparison for all the stations in the Los Angeles basin used in this study. Both data and synthetic waveforms are plotted at the same amplitude scale. The stations are shown in order of increasing angle of azimuth. The records of ING, LAS and BAL are shown in absolute time starting 5 seconds after the earthquake origin time. The trigger times of BEC, DWN and HOL are not available; the data and synthetics for these stations are aligned by the direct S on the tangential component.

Whittier Narrows Aftershock: October 4, 1987

	Vertical	Radial	Tangential

BEC: Δ = 16.2 km, ϕ = 169°, trigger unknown

0.98   3.51   3.88

Data

1.95   4.34   5.16

Synthetic

DWN: Δ = 16.2 km, ϕ = 201°, trigger unknown

1.17   4.67   4.56

3.08   7.78   8.53

ING: Δ = 23.6 km, ϕ = 223°

1.84   8.00   7.09

1.83   5.70   4.49

LAS: Δ = 20.5 km, ϕ = 225°

1.28   5.43   11.12

2.46   7.40   6.32

BAL: Δ = 24.4 km, ϕ = 257°

2.10   8.00   7.29

2.42   6.02   5.15

HOL: Δ = 22.0 km, ϕ = 279°, trigger unknown

0.80   2.13   3.55

5.44   7.08   2.22

15 Seconds   Amplitude in cm/s
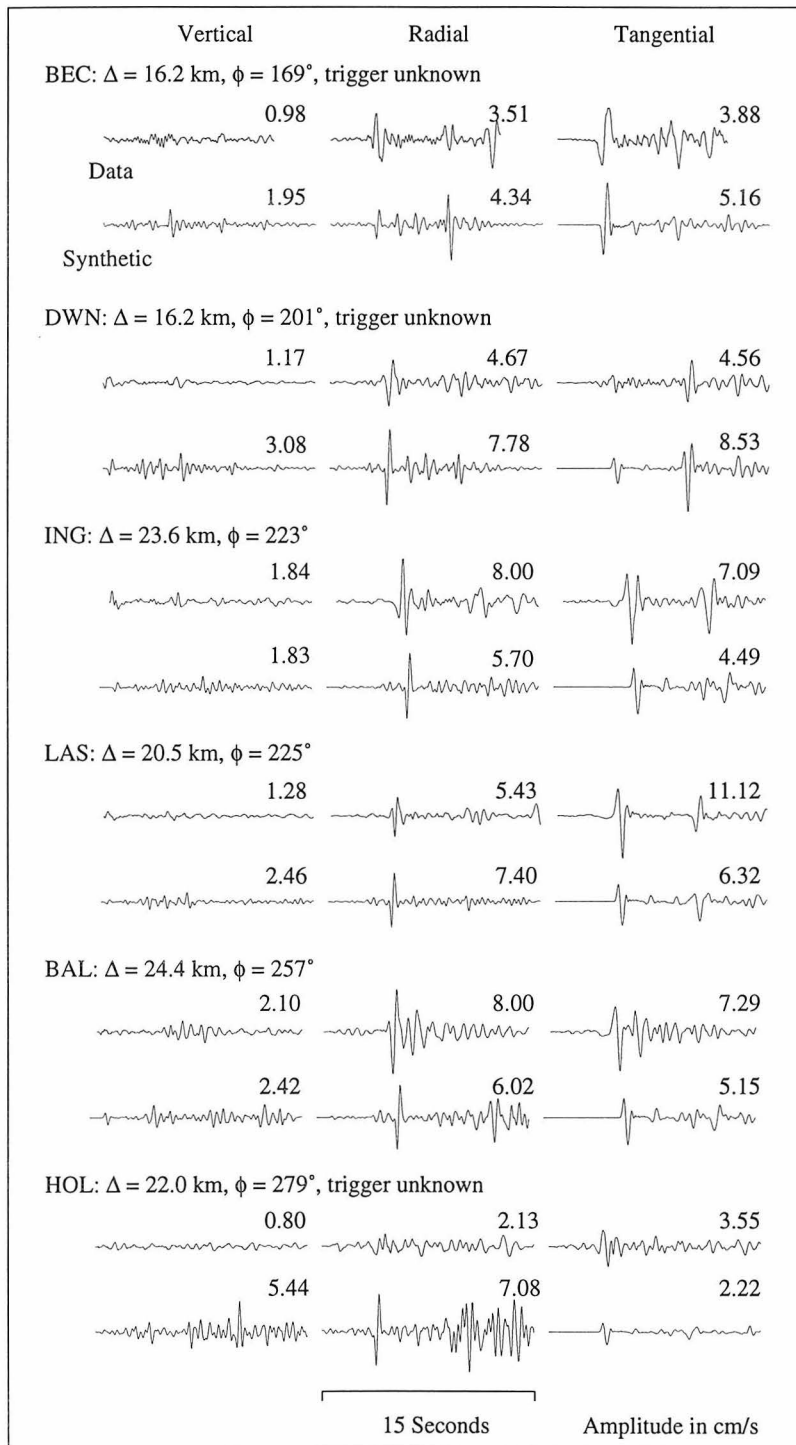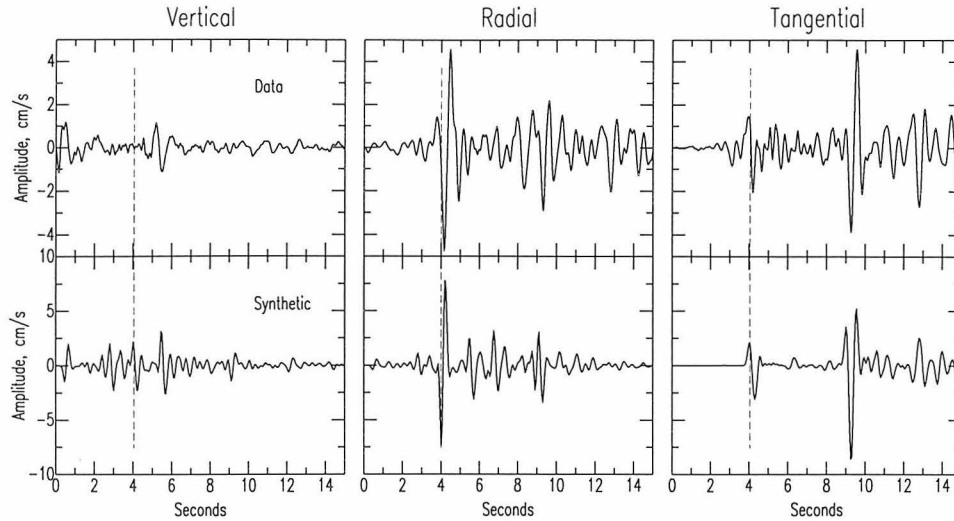
Figure 3.8: Comparison of velocity data and synthetics for station DWN. The amplitude scale for the synthetics is twice as large as the scale for the data. The dashed lines indicate the timing of direct S.

radiation pattern.

The modeling was primarily concerned with matching the tangential component and so it is not surprising that the vertical and radial synthetic waveforms, generated by the P-SV calculation, do not fit the data as well as the tangential component. The timing is still fairly good between different phases, but the absolute amplitudes are less consistent. Also, the relative amplitudes of the phases are not as consistent for the vertical and radial synthetic waveforms.

The model just discussed included only the east edge of the Los Angeles basin. It might be argued that energy propagating across the basin would be reflected back at its west edge and be trapped (Novaro *et al.*, 1990). This would produce a ringing effect that would complicate and lengthen the waveform. When such an edge is included in the model, however, there are almost no changes seen in the synthetic waveforms (Figure 3.9). In the middle of the basin, there is no effect at all on the strong multiple to the direct S phase. Stronger effects can be seen at the west basin edge, but they are still minor. The west basin edge probably produces more significant effects beyond the basin by disrupting surface waves across the basin and by setting up a further set of focused phases in offshore sedimentary basins. Such effects would be consistent

with the results of Vidale and Helmberger (1988).

The Whittier Narrows sequence was unusual because it occurred so close to the edge of the Los Angeles basin. Although concern is increasing about the threat posed by basin-bounding faults, it is also important to see whether the focusing effects modeled above persist for a seismic source farther from the basin. Since the June 28, 1991 Sierra Madre earthquake is along a similar azimuth to the basin as the Whittier Narrows aftershock, it is a useful event to consider. Unfortunately, records from strong motion stations in the Los Angeles basin for the Sierra Madre mainshock are not numerous. There are CDMG records from the DWN, BAL and HOL stations and a record from a Guralp instrument at USC (Figure 3.10). Synthetic waveforms were calculated using the source location and parameters of Dreger and Helmberger (1991), except that a lower moment was used than was found in that study. Helmberger *et al.* (1993) argue that most of the high-frequency energy produced by this event was generated in the area near the hypocenter where there was high stress drop and about 30% of the moment was produced.

Displacement synthetics for the azimuth to the station DWN with the Sierra Madre mainshock source mechanism are shown in Figure 3.11 for two models. The first model shown is simply the Whittier Narrows model extended as a flat-layers back far enough to cover the Sierra Madre source. For receivers over the deep basin, the time for the arrival of the direct S and following phases is obviously longer, but the waveform following the direct S is the same as that of the Whittier Narrows model. We have also included a basin edge near the Sierra Madre source in an attempt to model the effect of the San Gabriel basin on wave propagation into the Los Angeles basin. The direct S and multiples are still unaffected by this additional complexity, but there is a much longer wavetrain at ranges out into the Los Angeles basin. This model does not include the ridge that exists (at least for some azimuths) between the San Gabriel and Los Angeles basin. This would be expected to shorten the wavetrain in the Los Angeles basin (see Vidale and Helmberger, 1988), but not change the initial portion of the synthetic with the strong multiple. Overall, for both models the strong S multiple persists with similar amplitude and timing relative to the direct S arrival
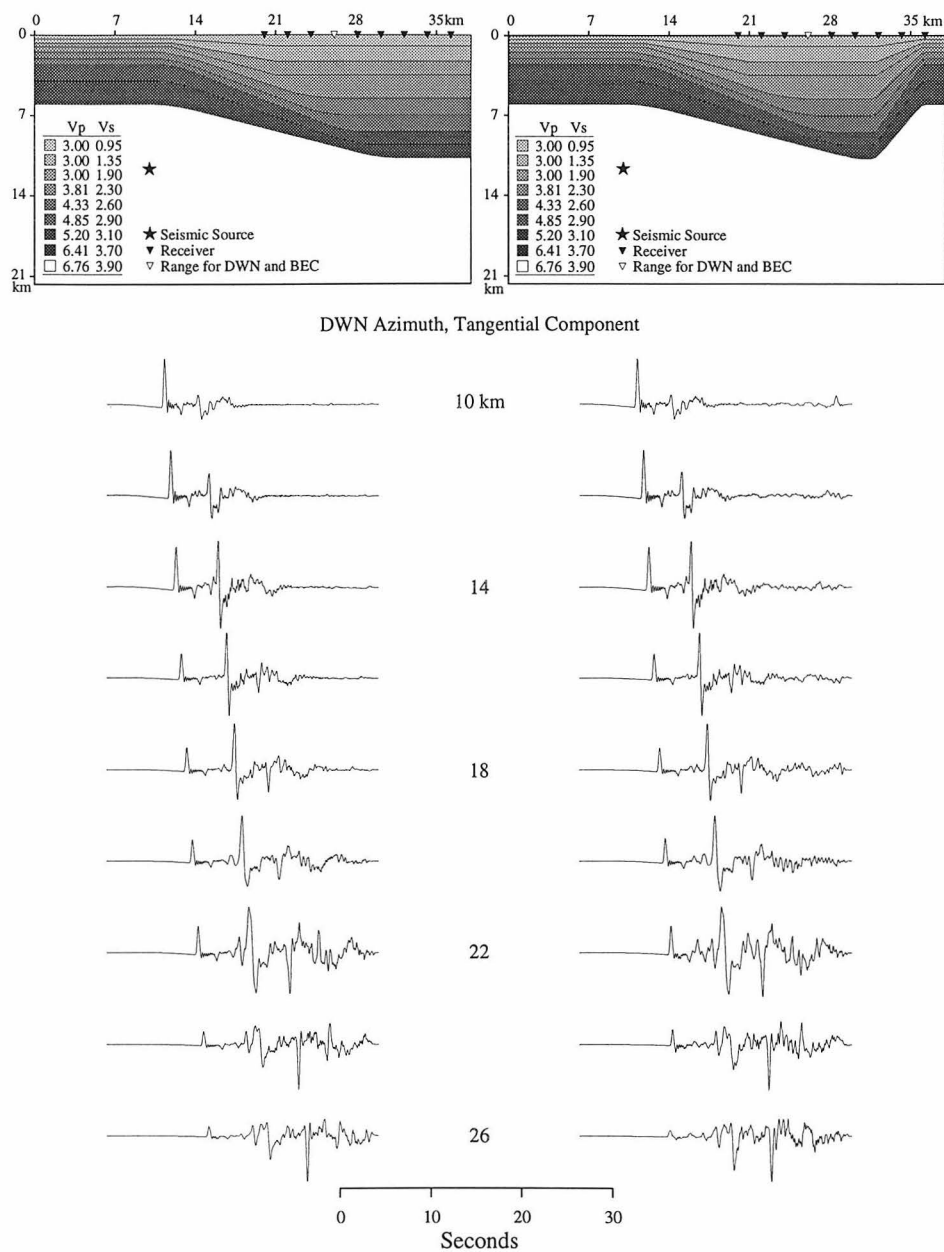
Figure 3.9: Synthetic waveforms of the tangential component for stations along the DWN azimuth for two models. The model on the left is the one used to produce the synthetics in Figures 3.6 and 3.7. In the model on the right, a steep SW edge is included in the basin velocity structure. Only minor variations are produced in the synthetics by this added feature.
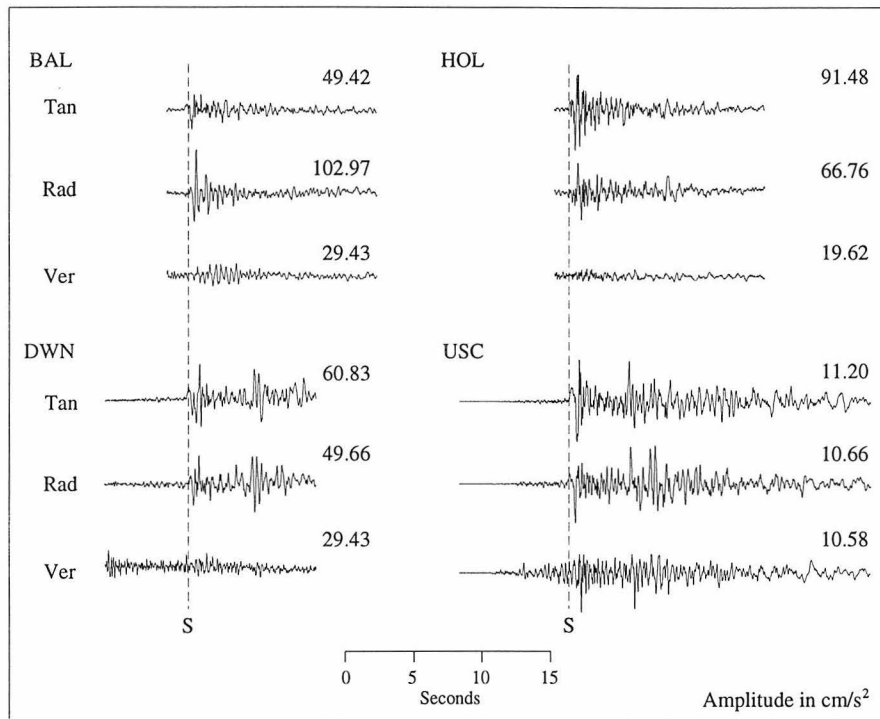
Figure 3.10: Acceleration data for the June 28, 1991 Sierra Madre mainshock at stations BAL, DWN, HOL and USC. All records are shown starting from their initial trigger and lined up on the direct S arrival. The amplitudes are in centimeters per second squared.

as was generated by the Whittier Narrows model.

The Sierra Madre mainshock was not strong enough to be recorded well on many of the CDMG stations in the Los Angeles basin. Records for the stations DWN, BAL and HOL were digitized from the CDMG report (Huang *et al.*, 1991). The tangential component acceleration records from these stations are compared with synthetic waveforms in Figure 3.12. A trigger time for the station HOL is known, so the comparison of data and synthetic can be made in absolute time. This comparison makes it clear that HOL triggered after the direct P. This also appears to be true for BAL, for which no trigger time is available. By comparison, the record for DWN is more complete. The USC record is most complete, with a trigger time well before the direct P and fifteen to twenty seconds of coda recorded after the peak amplitudes. A strong multiple phase is clearly present in the records from stations DWN, HOL and USC, and may be present in the waveform from BAL as well. Neither the amplitude nor the timing is as well matched between data and synthetic for the Sierra Madre mainshock as for the October 4th Whittier Narrows aftershock. The synthetic waveforms have a longer high-amplitude coda than is seen in the data. This may be because the model lacks the ridge between the San Gabriel and Los Angeles basins.

3.5 Discussion

Vidale *et al.* (1991) argue that in the Los Angeles basin strong site resonance effects control the polarization of received energy at frequencies greater than 1 or 2 Hz, and that the resonance direction at a given station tends to remain similar from event to event. The effect of the focal mechanism is not entirely drowned out by the site resonance, however. By taking the ratio of peak accelerations of the October 1 mainshock ($M_L = 5.9$)and the October 4 aftershock for stations over the Los Angeles basin, Vidale (1989) isolated the effect of the radiation pattern. These two studies indicate that at high frequencies the site resonance effects are dominant, but the radiation pattern for an earthquake still has a significant effect on the pattern of
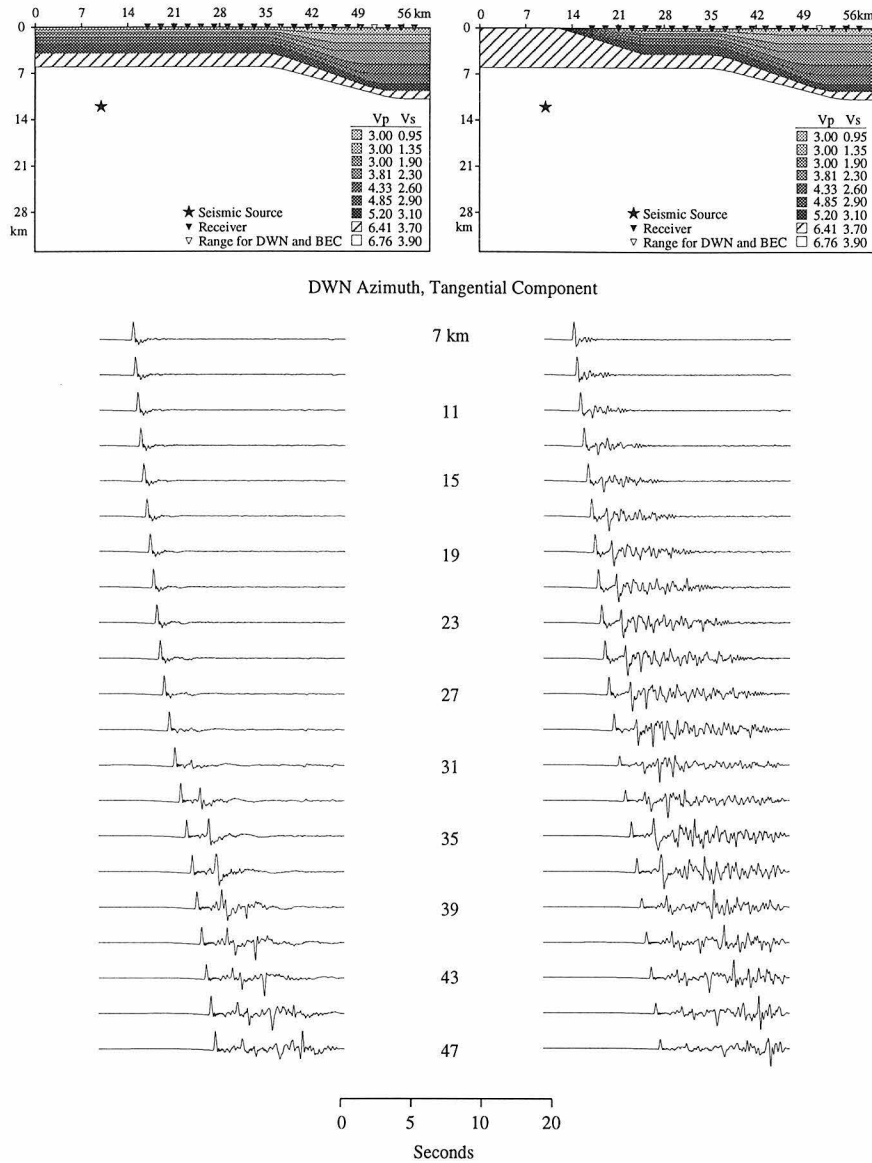
Figure 3.11: Two models for the velocity structure from the source of the Sierra Madre earthquake into the Los Angeles basin. Seismic velocities given in kilometers per second. The model on the left does not include any structure corresponding to the San Gabriel basin to the NE of the Los Angeles basin. The model on the right includes the northern edge of the San Gabriel basin. The source parameters found by Dreger and Helmberger (1991) are used to calculate the synthetic waveforms. The synthetics are displacement waveforms.
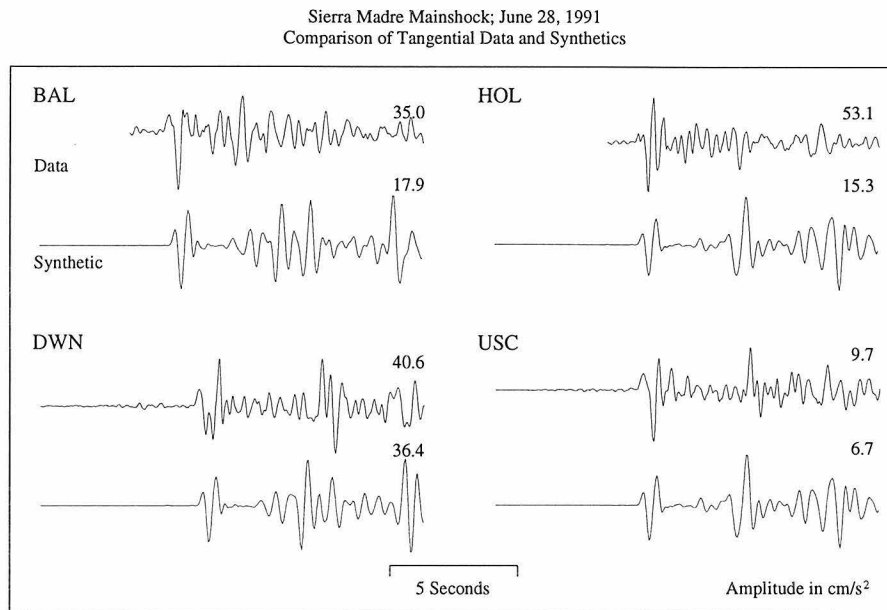
Figure 3.12: A comparison of acceleration data and synthetic waveforms for the tangential component of the Sierra Madre mainshock. The source parameters found by Dreger and Helmberger (1991) are used to calculate the synthetics. They include a moment of one-third of $M_0 = 2.5 \times 10^{24} dyn - cm$ (see text). Both data and synthetics have been bandpass-filtered between 0.1 and 3 Hz. No trigger times are available for BAL and DWN. For these stations, the data and synthetics are lined up by the direct S arrival. Trigger times are available for HOL and USC. The data and synthetic for HOL are compared in absolute time. However, the USC record is shifted 1 second to the left in order to line up the direct S arrivals of the data and synthetic.

peak accelerations.

Strong ground motions are complicated by the competing effects of site response and radiation pattern. Tangential component synthetic waveforms constructed for the October 1 Whittier Narrows mainshock with the focal mechanism of the largest subevent (Bent and Helmberger, 1989) predict that there should be no multiple after the direct S. Recordings from some stations, however, have a clear multiple. It is possible that the effects of the radiation pattern are being averaged by the three-dimensional basin structure. Figure 3.13 shows the variation in the amplitude ratio of the SS and S phases in synthetic waveforms as the focal mechanism is varied. The plots are planes with constant strike, rake and dip, respectively, slicing through the space of possible source parameters. The plots in the left-hand column intersect in this space at the parameters for the October 4 aftershock, and the plots in the right-hand column intersect at the parameters for the October 1 mainshock. The squares drawn in the figures indicate the intersection point for the planes plotted in that column. These plots predict that the majority of focal mechanisms should generate a multiple (SS) with at least half the amplitude of the direct S. Only narrow bands in the parameter space correspond to synthetic waveforms with no multiple. In the real world, it appears that waveforms are generated with a radiation pattern that corresponds to an averaged focal mechanism (Liu and Helmberger, 1985). This can be due to variations in the azimuth of the propagation path as slip progresses along the finite fault length, departures of the fault from a simple planar geometry and multipathing of the energy as it propagates to the receiver. In our case this means that receivers at a similar epicentral distance and overlying a similar velocity structure should have a visible multiple, regardless of the source mechanism.

The vertical radiation pattern for a vertical strike slip fault for the SH system is a constant dependent on the shear velocity in the source region, but the vertical radiation patterns for the other fundamental fault orientations are all dependent on the ray parameter and apparent slowness (Helmberger, 1983). This effect is evident in Figure 3.6. For the strike slip source, the SS phase is clearly developed beyond about 14 km, and, relative to the direct S pulse, its amplitude does not change much. For the

Figure 3.13: (next page) The variation in the amplitude ratio of the SS and S phases in synthetics as the focal mechanism is varied. The black areas have little or no multiple, and the white areas have multiples at least twice as large as the direct S. The synthetics were constructed with the velocity model shown in Figure 3.6, and the range selected, 16 km, is the distance from the epicenters of the October 4th aftershock and the October 1st mainshock of the Whittier Narrows sequence to station DWN. The left-hand column of figures show how the SS/S amplitude ratio changes in the synthetics if one parameter of the October 4 aftershock is held fixed and the other two parameters of the aftershock are allowed to vary. The right-hand column of figures show variation in the SS/S ratio when a parameter of the mainshock is held fixed and the other two parameters for the mainshock are varied. The parameters of the largest subevent of the 1 October Whittier Narrows mainshock (Bent and Helmberger, 1989) are used for this purpose. The squares in the figures indicate the location of the aftershock and mainshock in the parameter space.

Ratio of SS to S in Synthetics as Focal Mechanism Varies

Aftershock

Mainshock

Strike = 150

Strike = 280

Rake = 145

Rake = 100

Dip = 60

Dip = 40
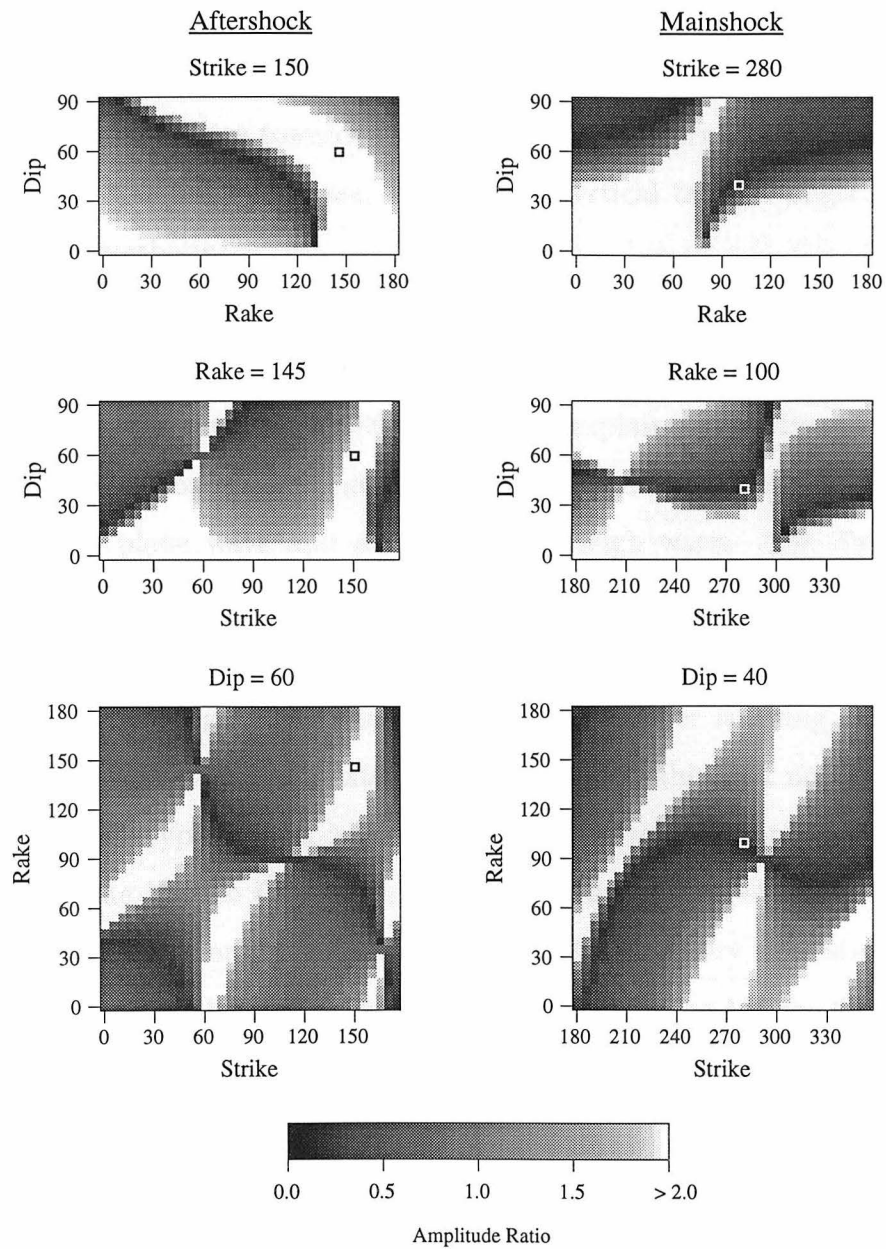
Amplitude Ratio

dip slip source, the SS phase increases in amplitude relative to the direct arrival over the range from 12 to 18 km. Beyond 18 km, the SS phase drops in relative amplitude and a third phase grows to dominate the records. The energy that produces the direct S phase is leaving the source in a nearly horizontal direction. This is a node in the dip slip vertical radiation pattern. By comparison, the multiples are produced by energy propagating upward from the source at angles where the radiation pattern for the dip slip source is stronger. As the range increases, the take-off angle of energy for a particular phase swings towards the horizontal, with correspondingly less radiated energy. A further multiple phase, with a near-vertical take-off angle may begin to dominate the synthetic.

It is commonly mentioned that an effect of sedimentary basins is to lengthen the waveform coda by setting up surface waves that are trapped to bounce back and forth in the basin. Kawase and Aki (1989), in order to explain observations at Mexico City from the 1985 Michoacan earthquake, examined the response of two types of basins to an incident plane wave and an incident Rayleigh wave. The Type 1 basin is a 10 km long and 1 km deep trapezoid, with a single velocity throughout, that is embedded in a homogeneous half-space. The Type 2 basin is a Type 1 basin with a very slow 5 km long and 250 m deep trapezoidal layer covering half its surface. They find that a Type 1 basin extends the coda noticeably, but not as strongly as a Type 2 basin. A Type 2 basin is required to explain the extraordinary duration and amplitude of the Mexico City observations. Sánchez-Sesma *et al.* (1988) have very similar findings. Neither a one-dimensional model with a very slow upper layer nor a two-dimensional deep basin (0.5 km) model can explain the Mexico City observation by themselves. Combining a two-dimensional basin with a thin slow velocity cap is much more successful.

In the present study, a comparison is made between a model with one basin edge and a full basin model. There is virtually no difference between the waveforms for these two models, and there is no significant increase in the duration of the coda. Although they do not find that it is effective enough in lengthening the coda to explain the Mexico City observations, Kawase and Aki (1989) do find that the Type 1 basin

model does significantly extend the coda in comparison to that produced by a one-dimensional model. There are several possible reasons for the difference between the results in this study and that of Kawase and Aki. The full basin model presented here is much deeper than Kawase and Aki's Type 1 basin. Our model has a gradational transition of velocity with depth. The largest impedance contrast between layers in the model is only 1.4, while Kawase and Aki use an impedance contrast of 2.5. Also, the velocity layers in our model do not completely pinch out at the basin edges, and energy leaves the basin over this lip. However, it seems unlikely that this aspect of the basin model is very significant because energy also leaks out of the trailing edges of basins (Vidale and Helmberger, 1988). The reason for this can be seen by considering the cartoon in Figure 1.1 with rays propagating from within the basin toward the basin edge to the left. The same ray geometry that serves to focus energy arriving from outside the basin will defocus rays striking the basin edge from the inside.

Strong motions are often characterized by peak accelerations and coda duration. It is also important, though, to consider the overall envelope and the change in the envelope as the range increases. The Type 1 basin of Kawase and Aki (1989) extends the coda in comparison to one-dimensional models, but only with monotonically decaying amplitudes. The very slow, thin layer over half of the basin is required to get a coda with amplitudes as large or larger than the initial portion of the record. Sánchez-Sesma *et al.* (1988) also needed a very slow capping layer to get a coda of extreme length. Their synthetic waveforms vary greatly in amplitude and duration at different receiver positions on the basin model. Our work indicates that very deep basin structures, without a very slow layer at the surface, can generate S multiples with amplitudes larger than the direct S phase. These synthetic waveforms are not of extremely long duration, but as the range increases further multiples increase in amplitude to dominate the record. As a result, a large event with multiple subevents distributed over a broad fault plane could generate long wavetrains in the Los Angeles basin with significant variations in the waveform envelope from point to point in the basin. Another complication of basin structure not addressed here is the role of attenuation, especially shallow attenuation and scattering. Some discussion of this is

given by Frankel and Vidale (1992), but our strategy is to establish the basic velocity structure and then add these properties later.

3.6   Conclusions

A multiple of the direct S phase, seen in data from the Los Angeles basin stations for the October 4, 1987 Whittier Narrows aftershock, can be forward modeled with a two-dimensional velocity structure. An attempt was made to fit absolute S and P times (when available), S-P times, SS-S times, the relative amplitude of S and SS, and the overall absolute amplitude. These parameters in the data are matched well by the synthetic waveforms, though the phase of the SS pulse is not. The fit is more erratic for stations in the north part of the basin (further off the cross-section azimuth of about N205°E). The cross-section into the basin changes significantly with azimuth from the source of the Whittier Narrows events, and cannot be modeled by a single two-dimensional model.

Basin edge effects are important. Critical angle reflections of energy in the dipping layers at the leading edge of the basin trap energy and turn it sharply back to the receivers. In a section of synthetic waveforms calculated for the October 4 Whittier Narrows aftershock, the amplitude of SS is greatest in the deepest part of the basin, where it is 2 times larger than direct S. The coda duration increases from 8 seconds to more than 20 seconds from the NE to the SW. A full basin model is compared to a model with only a leading basin edge. The full basin model produces no significant increase in coda duration when compared to the model with a single basin edge. At the far edge of the basin, energy leaks out rather than being strongly reflected back into the basin. The basin edge effect is not significantly different if the earthquake is located away from the basin (e.g., the Sierra Madre mainshock) or immediately adjacent to it (e.g., the Whittier Narrows aftershock).

We have achieved some success in deterministic, forward modeling of these strong motion records. Such modeling is useful in predicting strong motions of large events in the region and in preliminary efforts in the construction of three-dimensional models.

That is, it establishes constraints on the structure of two-dimensional slices cutting through the region to be modeled in three-dimensional analysis. Such model slices could place additional constraints on the three-dimensional model beyond what is available from geologic and borehole data alone.

Acknowledgments

Chapter 4

2D Modeling of Two Aftershocks of the Northridge Earthquake

4.1 Abstract

Two aftershocks of the January 17, 1994 Northridge earthquake are analyzed and modeled with 2D finite difference. The event epicenters both lie at the northwest edge of the San Fernando Basin, but the hypocentral depths differ – one is 4 km deep, the other is 16 km deep. Waveforms were recorded by portable instruments deployed across the basin by a number of institutions following the Northridge mainshock. The waveforms are integrated to displacement and examined in the 0.3 to 4 Hz pass band. For the shallow event, distinctive features in the data are (a) a broad direct S phase at stations in the basin, (b) large amplitude surface waves and extended coda at a cluster of stations 8 km into the basin, and (c) a high-frequency, Hilbert transformed ($\pi/2$ advanced in phase) direct S phase at stations beyond the basin, in the Santa Monica Mountains. The deep event is less strongly effected by the basin. For this event, the direct S phase is broad in the basin. Rather than surface waves at the stations 8 km into the basin, there is a discrete multiple to direct S on the tangential component that can be distinguished from the coda. The stations beyond the basin have higher frequency direct S phases, compared to basin stations, but they are not Hilbert transformed. For both events, the vertical waveforms have low amplitudes at all stations, at least two times smaller than the horizontal components. An array analysis was done with the tangential component records from the cluster of stations 8 km into the basin. This analysis indicates that the surface waves generated by the shallow event and the shear wave multiple generated by the deep event are arriving on-

azimuth from the source, and a 2D model can reasonably be applied. These features in the data can be explained by a simple basin model with significant structure below the basin. There is a strong contrast in the basin at about 1 km depth. The lower basin is relatively transparent. The duration of the surface waves generated at the basin edge require a strong vertical gradient just above the shallow source to turn energy up toward basin. The Hilbert transformed direct S phases recorded in the Santa Monica Mountains are modeled as a triplication feature. They can be explained by a moderate vertical gradient at 5.5 to 6.5 km depth. These structures below the basin have little effect on propagation from the deep source. The sensitivity of this model is checked by examining the parameter space around it. Variations of 15% in the velocity contrast across the interface in the upper basin degrade the fit of the surface waves with the data. Moving the interface above the shallow source up 1 km also alters the surface waves. This modeling suggests that a strong velocity contrast is needed within the San Fernando Basin and that the structure below the basin plays a significant role in turning energy up around the basin.

4.2   Introduction

Over 7 weeks following the January 17,1994 Northridge, California mainshock, a deployment of more than 100 portable stations recorded many aftershocks. This deployment generated a data set of high quality, digital waveforms recorded in and around the San Fernando basin (Edelman and Vernon, 1994). This is an opportunity to do a detailed analysis and modeling of the effects of the San Fernando basin on wave propagation. In this study we examine how the interaction of seismic waves with the basin and the background structure differs for a shallow and deep source.

The San Fernando basin is a 4-5 km deep sedimentary basin just north of Los Angeles. The Northridge mainshock nucleated at 16-19 km depth under the southern edge of the San Fernando basin and it ruptured updip to the northeast to about 5 km depth (Wald *et al.*, 1996). The majority of aftershocks were in the shallow region of this fault plane and in a shallow cloud above the fault plane (Hauksson *et al.*,

1995b). Damage due to the mainshock was greatest in the northwest basin, though mitigated by the relatively sparse population in that area. Additional zones of heavy damage were just north of the Santa Monica Mountains in Sherman Oaks, and south of the mountains in Santa Monica and the northern Los Angeles basin. Significant directivity effects amplified ground shaking on the northern side of the basin. The Tarzana site, southwest of the mainshock, recorded horizontal accelerations of 1.8 g, and strong shaking occurred in the Sherman Oaks area to the east. These sites are affected strongly by local site conditions Hartzell *et al.* (1996).

In mainshock ground motions from sites in the San Fernando basin, large-scale basin effects seem to be subdued compared to source effects. Wald *et al.* (1996) modeled the details of the source rupture process with a combined inversion of local strong ground motion, teleseismic, and geodetic data sets. For the local region, they used a 1D velocity model to generate synthetic Green's functions for the inversion. The source model they determined from the first 15-20 seconds of local ground motions alone is consistent with models based on geodetic and teleseismic data sets, and with the inversion of the combined data sets. They found a slip duration of 7 seconds. This is long enough to interfere with the identification of propagation effects from the edges of the San Fernando basin.

Source studies of the Northridge aftershocks to find depth, source parameters, and moment of the events have been done with local and regional data by Hauksson *et al.* (1995b), Thio and Kanamori (1996), and Song and Helmberger (1997). Hauksson *et al.*, from first motion data, and Thio and Kanamori, working with surface wave data, reached different conclusions for a significant number of events. Song and Helmberger inverted broadband data, both P_{nl} and surface waves portions of the waveforms, to resolve the issue. Their results are more consistent with the depth and source parameters found by Hauksson *et al.*. In our study, we use source parameters from Song and Helmberger.

Most of the aftershocks are farther north than the mainshock, in a geometry that is more likely to produce basin-edge effects. Pitarka and Irikura (1996) and Haase *et al.* (1996) calculated synthetic waveforms for 2D models to compare with

waveform data from an aftershock at the north side of the basin, near the epicenter of the 1971 Sylmar earthquake. Pitarka and Irikura's model combines a model of the San Fernando and Los Angeles basins similar to that in Vidale and Helmberger (1988) with a cross-section from the 3D tomographic model of the area by Zhao and Kanamori (1995). With this structure they can explain some secondary arrivals at sites in the San Fernando basin and the Los Angeles basin. Haase *et al.* model data from the same event along a similar cross-section. Their model is a cross-section from an early version of the 3D tomography of the Los Angeles area constructed by Hauksson and Haase (1997). They focus on waveforms recorded in the Los Angeles basin, where the tomographic model is best constrained. With a reduction of the velocity in the top 0.5 km of the model, they match features seen in the data at sites over the deepest portion of the Los Angeles basin.

Haase *et al.* point out that 2D models can potentially be used to refine 3D velocity models. Care has to be taken to avoid over-modeling in 2D, and mapping 3D structure into the 2D model (Frankel, 1993). The advantage of 2D models are that the calculation of synthetics with moderately high frequency content (> 1 Hz) are reasonably fast. Also, 2D models are somewhat easier to work with, so it is straightforward to examine the effect of changes in the structure.

In this study we contrast records from a shallow event and a deep event at the northwest corner of the San Fernando basin (Figure 4.1). The events epicenters are similar, but the hypocenter depths are 3.6 km and 16 km. They are both recorded by the same set of stations including a cluster of three stations about 5 km from the basin edge. Specific features in the waveforms and amplitude distribution distinguish each event. A three-station cluster in the line of stations, and data from these stations can be fed through an array analysis that indicates (among other things) whether or not some waveform features can reasonably be modeled with 2D basin structures. The modeling indicates which waveform features are due to background crustal structure, interaction with the deeper basin, or the effect of near-surface micro-basin and soft soil structures. Finally, the model space around the preferred model is examined to get a sense of the sensitivity of the model to changes in the structure.
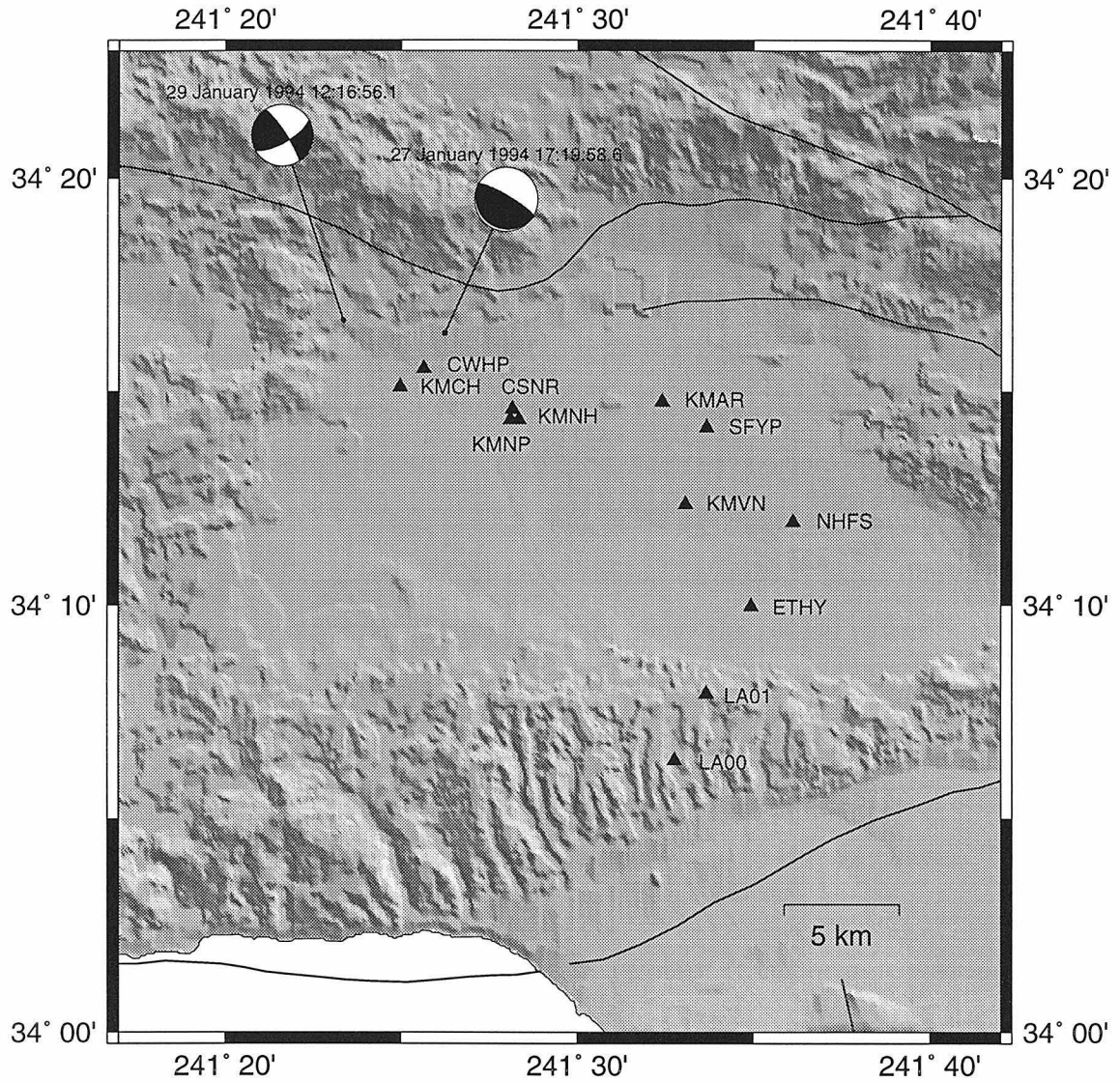
Figure 4.1: Map of San Fernando basin and surrounding topography. Focal mechanisms of the aftershocks analyzed in this study are shown in lower-hemisphere projection. Triangles are seismic receivers used in this study. The thin black lines depict a few of the significant faults in the area.

Date	Time	Strike	Rake	Dip	Moment	Depth
January 29, 1994	12:16:56.08	60	10	70	2.3×10^{22}	3.6
January 27, 1994	17:19:58.58	120	90	10	4.3×10^{22}	16.3

Table 4.1: Events analyzed and modeled in this study. The source parameters of strike, rake, dip, and moment are from Song and Helmberger (1997). The depth is from Hauksson *et al.* (1995b).

4.3 Data

The waveforms analyzed and modeled in this study were recorded during the deployment of portable instruments following the Northridge mainshock. The deployment involved a number of institutions associated with the Southern California Earthquake Center (SCEC) (Edelman and Vernon, 1994). The deployment lasted seven weeks. It included both broadband and short period velocity sensors, and strong motion accelerometers. GPS or Omega clocks were used to maintain timing accuracy at most sites, though a few stations had large timing errors and some deployed instruments had only internal clocks, subject to drift. Over the period it was deployed, the portable network recorded 46 events with magnitude over 4.0.

In this study, we have focused on two events at the northwest corner of the San Fernando basin and a set of stations that recorded both events. These stations run along a cross-section over the basin from the northwest to the southeast. The event parameters are listed in Table 4.1.

The data at all stations were recorded on velocity transducers or strong motion accelerometers. The waveforms were integrated to displacement and bandpass filtered with corners at 0.3 and 4 Hz. The relatively short long period corner of the filter was required for stable integration. The high frequency corner of the filter is controlled by the onset of grid dispersion in the finite difference synthetic waveforms that data are compared against.

Timing of some records was adjusted to account for known timing errors and uncertainties at some stations (Edelman and Vernon, 1994). The timing shifts are listed in Table 4.2. Station CWHP has a timing error of approximately 2 seconds identified

Event	Station	Shift (sec)
January 29, 1994, 12:16:56.08	CWHP	−2.0
	KMCH	0.9
	KMNP	1.2
	KMNH	0.8
	KMAR	1.0
	KMVN	1.2
January 27, 1994, 17:19:58.58	KMNP	−0.8
	KMNH	−0.6

Table 4.2: Time shifts applied to data from the two Northridge aftershocks.

by Edelman and Vernon. The Kinemetrics stations (KMNP, KMNH, KMAR,...) were run on internal clocks and are subject to drift. We applied ad-hoc timing adjustments to these records based on the timing of nearby trusted stations.

Waveforms from the shallow event show indications of strong interaction with the basin. The stations can be grouped by distance into four clusters at < 5 km, 8 km, 14-17 km, and 20-25 km (Figure 4.2). In the first cluster, stations KMCH and CWHP, the direct shear wave on the tangential and radial components is the dominant phase with some coda and possibly a shallow basin multiple 3 seconds behind the direct. The second cluster, stations CSNR, KMNP, and KMNH, has the most obvious basin effects in the record section. On the tangential component there are two or three cycles of basin-generated surface waves that can be correlated across the three traces. Each of these stations is about 300 m from the others. An array analysis of these waveforms is discussed below. The third cluster, stations KMAR, SFYP, and KMVN, is spread across the north-central portion of the basin. The waveforms have relatively little coherence among them. KMVN records a late, large-amplitude pocket of energy starting 3 to 4 seconds after the direct shear wave. The fourth cluster, stations NHFS, ETHY, LA01, and LA00, extends from the center of the basin south across the Santa Monica Mountains. The transition out of the basin, at station LA01, has surprisingly high amplitude and ringing phases after the direct shear wave on the horizontal components. Both LA01 and LA00 have direct shear

waves Hilbert transformed ($\pi/2$ advanced in phase) relative to stations in the basin.

The tangential and radial components of the records of the shallow event have peak displacements 2 to 5 times larger than those of the vertical component. At stations within 10 km of the source, the peak amplitudes on the tangential components are at least twice those on the radial components. Beyond 10 km, the peaks amplitudes on the tangential and radial components are most often about the same. KMVN and LA01 stand out from other stations in their respective clusters as having particularly large peak amplitudes.

Compared to the shallow event, waveforms recorded from the deep event (Figure 4.3) show relatively little effect from the basin. The deep event is approximately 5 km east of the shallow event, so the stations are about 3 km closer to the deep source than they are to the shallow source. In discussing the deep event data, however, the same clustering of stations as before can be used. At all stations the direct shear wave is the strongest arrival. The second cluster of stations has a prolonged coda, but only a single discrete arrival 4 seconds after the direct S that might be a basin-edge-induced multiple. The third station cluster has variable waveform amplitude, as in the case of the shallow source, and station KMVN has a large-amplitude coda that starts 4 seconds after the direct S. In the fourth station cluster, station LA01 again has large-amplitude ringing immediately after the direct S. In this case the ringing was recorded on all three components and particularly vigorously on the radial component. However, the direct S of LA01 and LA00 is not Hilbert transformed relative to stations in the basin.

As was true for the shallow event, for the deep event the peak displacements on the horizontal components are 2 to 5 times larger than those of the vertical component records. In contrast to the shallow event, at stations within 5 km of the source the radial component peak displacements are larger than those on the tangential component. At greater distances the peak displacements are larger on the tangential components. Again KMVN and LA01 stand out with particularly large peak amplitudes.

The comparison of peak amplitudes between stations and across both events is

Figure 4.2: Record section of displacment waveforms for the shallow event, January 29, 1994, 12:16:56.1. Station names are on the left of each trace. Peak amplitudes in cm are on the right. Records are shown in absolute time, where available, with the origin at 5 seconds. Stations with unknown timing are shifted as needed relative to a station with good timing. Waveforms are plotted in absolute amplitude scaled by range from the source. Note that the vertical records have been amplified by a factor of 4 compared to the horizontal components. This was done to improve the visibility of the vertical waveforms.

Figure 4.3: Record section of displacment waveforms for the deep event, January 27, 1994, 17:19:58.6. Plotting conventions are the same as those in Figure 4.2.
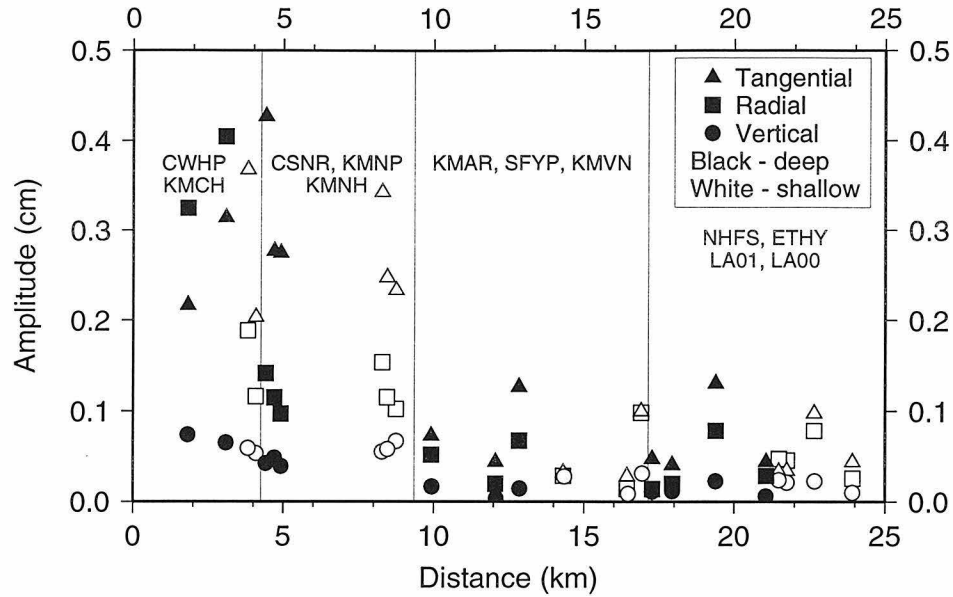
Figure 4.4: Peak amplitudes of the deep and shallow event data plotted against range from the source. Black (white) symbols are values for the deep (shallow) event. The station ranges fall naturally into 4 cluster, indicated by the station names and the thin vertical lines. For comparison with the shallow event, amplitudes from the deep event are normalized for the relative moments of the events and the different distance from source to receiver.

summarized in Figure 4.4. The four clusters of stations described above are indicated by the vertical lines. The horizontal distance from the deep source to the stations is about 3 km less than the horizontal distance from the shallow source to the same station. For comparison sake, the peak amplitudes of the deep event are adjusted for the relative moments of the events (a factor of 2.3/4.3) and for the relative effect of geometrical spreading (a factor of 3.0 at CWHP and of 1.1 at LA00). These two adjustments balance each other at station CSNR.

Despite the waveform comparison that suggests waves from the deep source don't interact strongly with the basin, the pattern of peak amplitudes is quite similar for the two events. In the second cluster, CSNR has the largest horizontal amplitudes for both events and KMNP and KMNH share very similar amplitudes. In the third cluster, SFYP has the smallest and KMVN has the largest amplitudes. In the fourth cluster,

LA01 has the largest amplitudes on all three components. As noted earlier, the waveforms from stations KMVN and LA01 also indicate some local site complexity. The relatively large amplitudes at CSNR are more surprising, given its tight clustering with the other two stations in its cluster.

The cluster of stations CSNR, KMNP, and KMNH (Figure 4.5) is tightly enough spaced that an array analysis based on the coherence of the wave shape can be applied. The results of this analysis are useful because they indicate which portions of the waveform are arriving on-azimuth and can reasonably be modeled with a 2D structure. There is the potential to over-model the data and map 3D structure into the 2D model. Further, this analysis indicates if there are systematic variations in apparent velocity and back azimuth with time. This suggests which portions of the basin control 3D effects.

We use the technique employed by Frankel *et al.* (1991) in the Santa Clara Valley on data from a dense array that recorded aftershocks of the 1989 Loma Prieta earthquake. This involves cross-correlating the waveforms in order to find the back azimuth and apparent velocity of a plane wave that best fits the timing of phases in the waveforms. Unfortunately, stations KMNP and KMNH ran on internal station clocks and the raw timing is inaccurate. We assume that the direct S wave arrives on-azimuth from the source with an apparent velocity of 3 km/s for the shallow event and 4 km/s for the deep event, and set the timing of KMNP and KMNH relative to CSNR. The analysis is applied repeatedly on a narrow, sliding time window. We use a window 1.25 seconds, which is similar to the dominant period of the basin-generated waves. The analysis is applied every 0.5 seconds along the waveforms. Only points for which the correlation is greater than 80% are shown.

The array analysis for tangential component records of the shallow event is shown in Figure 4.6. Apparent velocity (V_{app}), initially constrained to a value of 3 km/s, fluctuates and gradually decays to below 1 km/s. In the first 4 seconds after the direct S phase, spanning the largest amplitude basin reverberations, the back azimuth of arriving energy fluctuates slightly but stays between the station-epicenter back azimuth and north (a 60° range). Further into the records the back azimuth shifts
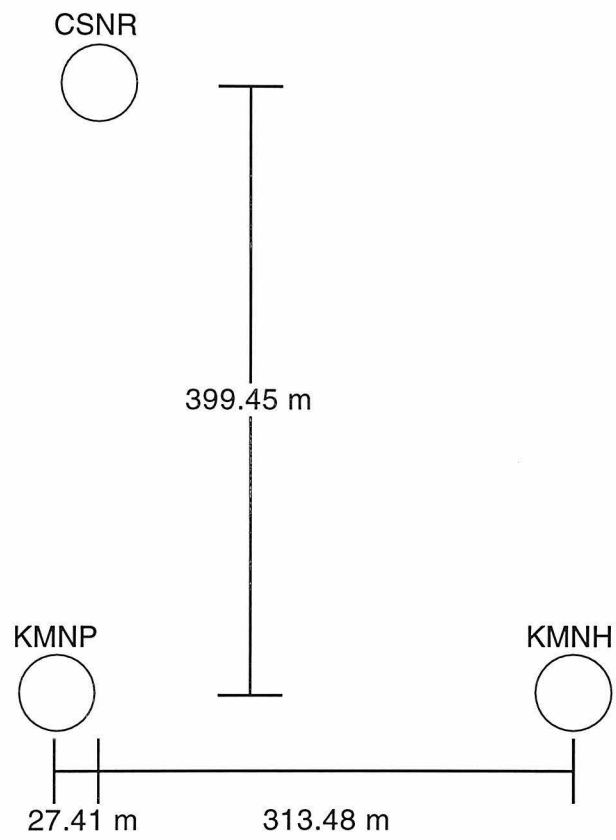
Figure 4.5: Geometry of the cluster of stations used for the array analysis. North is towards the top of the page.

rapidly between arriving on-azimuth, arriving from the south, and arriving from the northeast. The number of windows in which the correlation is high falls towards the end of the records where the waveform amplitudes are low and coda has developed.

The array analysis for tangential records of the deep event is shown in Figure 4.7. Compared to the shallow event analysis, there are fewer time windows with waveform correlations greater than 80%. This indicates that the basin is producing fewer coherent phases with energy to stand out from the coda. Wavefronts from a deep source should be subhorizontal with high V_{app}. Therefore, it is interesting to note that where the back azimuth is nearly on-azimuth, V_{app} tends to be higher. Off-azimuth arrivals are similar to those seen for the shallow event, from the south and from the northeast. Energy arrives from the south with low V_{app} immediately after the direct S wave. This suggests a weak scatterer just south of the station cluster, rather than energy propagating all the way from the south edge of the basin. Energy from the northeast arrives later in the record and could be explained by the main structure of the basin further from the stations.

4.4   Modeling

A forward modeling, trial-and-error approach was taken to studying the data. Synthetic waveforms were calculated for each working model by a two-dimensional finite difference numerical technique (Vidale *et al.*, 1985; Helmberger and Vidale, 1988). The algorithm is a centered-grid scheme, fourth order in space and second order in time, with absorbing boundary conditions Clayton and Engquist (1980). Attenuation is not incorporated in the code. The response for an arbitrary double-couple source can be calculated. For the two events, the source parameters of Song and Helmberger (1997) were used (Table 2.1). They did inversions of regional broadband data with a grid search algorithm. Their source parameters are similar to those found by Hauksson *et al.* (1995b). 0.3 and 0.2 second triangle source time functions were convolved into the waveforms for the shallow event and the deep event, respectively.

After each calculation, the synthetic waveforms were compared with the data

12:16 (CSNR, KMNP, KMNH Cluster)
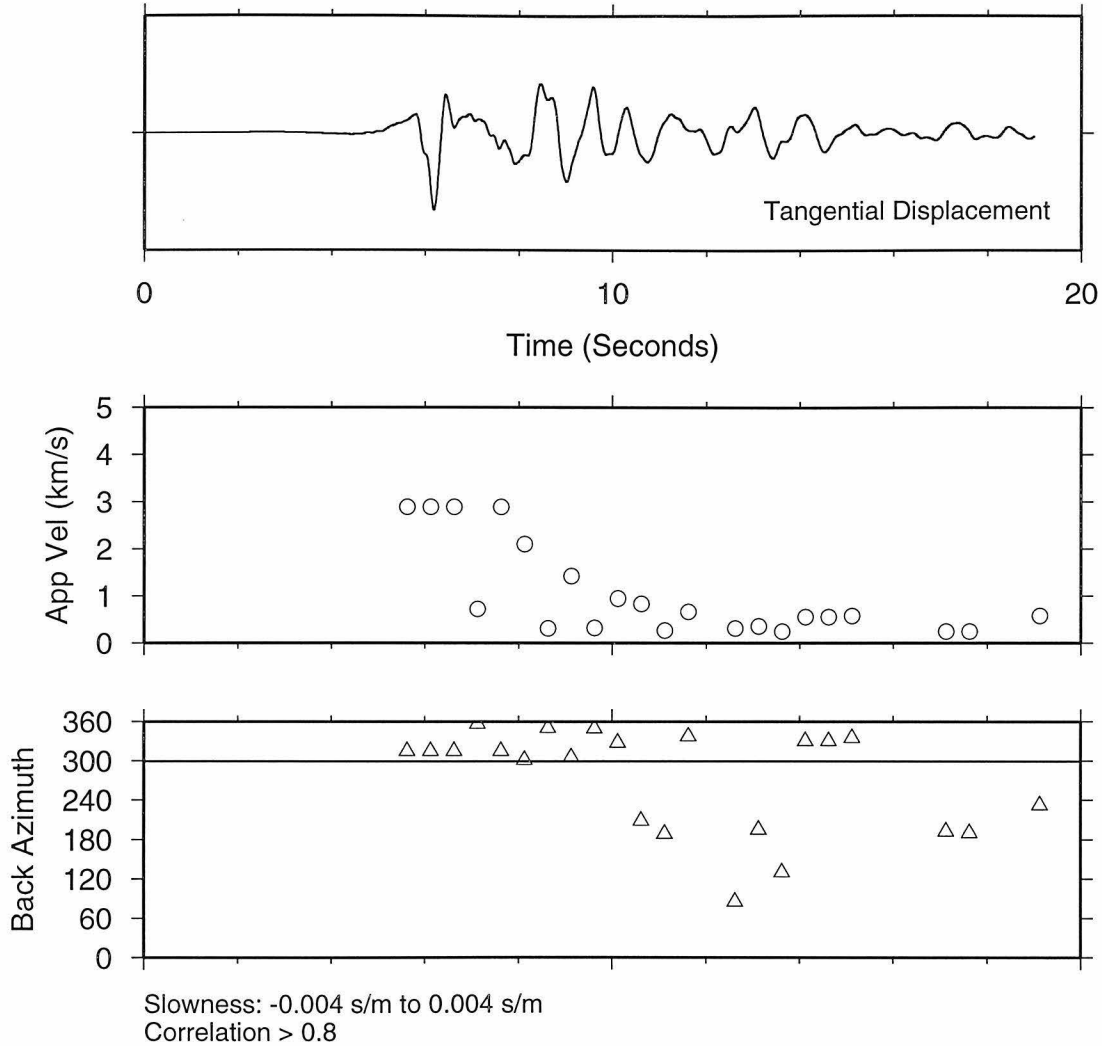
Figure 4.6: Array analysis for the shallow event of the tangential component at station cluster CSNR, KMNP and KMNH. Apparent velocity and back azimuth are determined. The trace from CSNR is shown for reference. The line at 300° indicates the true back azimuth of the stations to the source. Only points from time windows with station cross-correlation greater than 0.8 are shown.

Figure 4.7: Same as Figure 4.6, but for the deep event. The true back azimuth of the cluster is 320°.

waveforms and adjustments were made to the model. The distinctive features in the data discussed above, were the focus of the modeling. Some features suggested a starting point for the modeling. The surface waves 2 seconds after the direct S at CSNR, KMNP and KMNH (and the lack of such phases at KMCH and CWHP) suggest the basin edge starts a few kilometers from the source. The surface waves have 1 second period, and this implies a strong gradient within the basin. The Hilbert t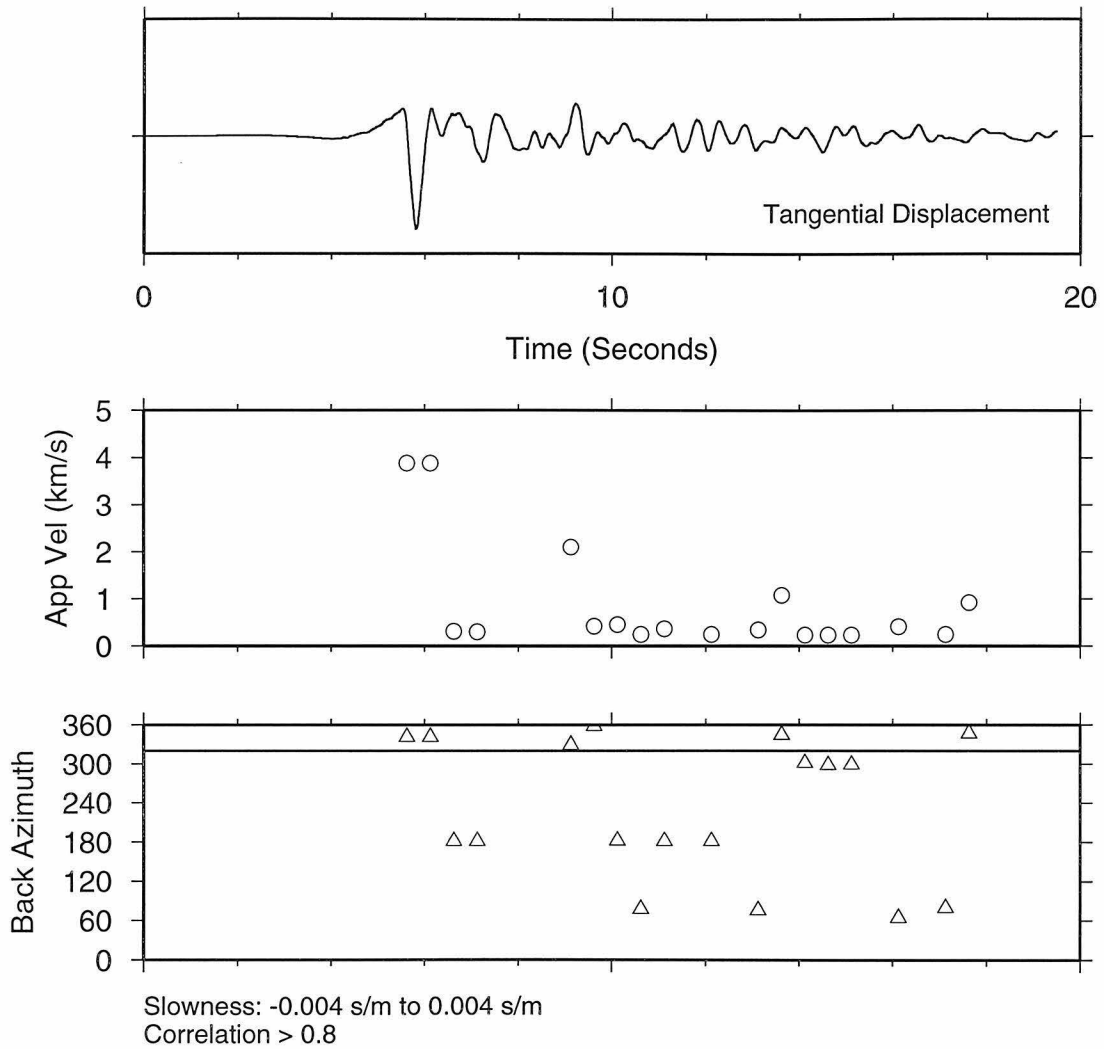ransformed direct S phases at LA01 and LA00 suggest a gradient beneath the basin to generate a triplication effect. The abrupt termination of basin phases from ETHY to LA00 in conjunction with the onset of the Hilbert transformed direct S at LA01 and LA00 place some constraints on the trailing edge of the basin.

Our preferred model for this cross-section through the San Fernando basin is shown in Figure 4.8. The basin is defined by two zones of high velocity contrast. The interface just above the source forms the bottom of the basin. The high contrast interface at about 1 km is a mid-basin gradient that controls critical reflection basin-edge trapping. The bottom of the basin at 3.5 km turns a greater percentage of energy radiated from the source up into the basin-edge structure. This shallow basin-edge structure controls the timing and period of the surface waves. The interfaces 2 to 3 km below the source critically reflect energy 20 to 25 km from the source and from a triplication phase. Turning this energy up sharply around the trailing edge of the basin requires a gradient 1 to 3 km beneath the surface of the Santa Monica Mountains. A shallow dip on the trailing edge of the basin tends to direct basin-trapped energy under the Santa Monica Mountains rather than along the surface (i.e., the tunneling effect reported by Vidale and Helmberger (1988).)

Figure 4.9 is a record section of synthetic waveforms for the shallow event. The variation in waveform along section is fit fairly well. There are multiple cycles in the surface wave group following the direct shear wave at stations CSNR, KMNP and KMNH. The relative amplitude of the surface waves to the direct arrival is correct on the tangential component, though not on the radial and vertical components. Also, the ratio of peak amplitudes of the tangential to radial component is correct. At stations KMAR, SFYP and KMVN the most notable feature is the amplitude
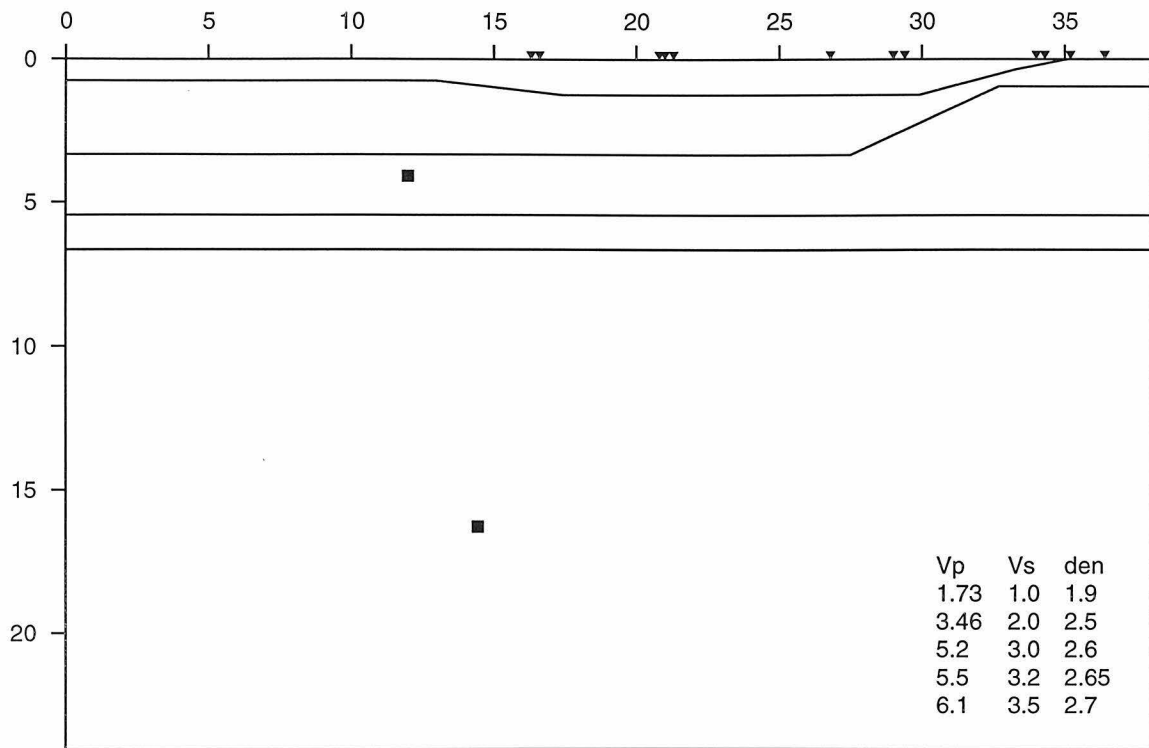
Figure 4.8: 2D model of the Northridge basin used to generate synthetic waveforms. Range and depth in km. Squares indicate the two source locations used in the calculations. Triangles are receiver locations for the stations in this study. Compressional and shear velocities in km/s, and density in g/cm^3.

Figure 4.9: Record section of synthetic displacment waveforms for the shallow event. Plotting conventions are the same as those for Figure 4.2, except that vertical records are scaled up by a factor of 2 rather than 4.

of KMVN relative to the other two stations. On the tangential component this amplitude and waveform variation is fit quite well. However, on the radial and vertical synthetics there is little variation between the stations. Finally, the variation in the direct shear wave between stations NHFS, ETHY, LA00, and LA01 is fit by the triplication structure below the source. The flip in polarity on the tangential component at ETHY is not fit. The extreme variation in ringing phases from NHFS to LA01, in shape, period and amplitude is not fit by this model. We discuss this at more length further on.

Across the three components, the amplitudes of the data at the first pair of stations are poorly fit by the synthetic waveforms. However, the error is not systematic in a

way that suggests a change in the model. The large variation between components at KMCH can be explained by a source SV minima and SH maxima on this azimuth. Synthetics for the second cluster of stations are about half that of the data on the radial and tangential components, but a little high on the vertical component. As mentioned above, at the third cluster of stations the variations among the stations are fit well in waveform and amplitude on the tangential component but not on the other components. The tangential component synthetics for KMAR and SFYP are affected by an SH mode along the azimuth to those stations. In the data, the ringing on KMVN must be explained by some other phenomenon which effects both the SH and P-SV systems. For the last cluster of stations, the high amplitudes in the data on the radial and tangential components of LA01 are not generated by the model. Instead stations LA00 and LA01 have similar amplitudes. The low velocities on the radial and vertical components of the synthetics of these two stations are due to the SV node at this azimuth. The data are insensitive to this node. Overall, the synthetic waveform amplitudes are much more sensitive to nodes in the source radiation pattern than the data and indicate that at stations KMVN and LA01 some additional phenomenon is probably occurring to increase data amplitudes.

The synthetics for the deep event (Figure 4.10) are characterized by simple waveforms dominated by the direct shear wave. Moderately sized multiples (less than 50% of the amplitude of the direct arrival) are generated at sites in the basin. On the tangential component, the largest amplitudes are seen at the second cluster of sites (CSNR, KMNP and KMNH). On the radial component the largest amplitudes are at the first two stations. The vertical waveforms are relatively subdued (note that this component is plotted at twice the amplitude to improve viewing); neither the direct P nor the direct S phase stands out consistently from the coda. These features in the synthetic waveforms are a good match to the data.

In the data, the polarities of the third station cluster on the radial component are problematic. SFYP appears to be flipped, but the synthetics are consistent with the SFYP polarity. This suggests a combination of polarity problems in the data and an inaccurate source mechanism. The shallow event doesn't clarify the problems

Event: 17:19 [Synthetics - 2D v4.1.1.1, 0.2 second Source Time, Bandpass 0.3 to 4 Hz]
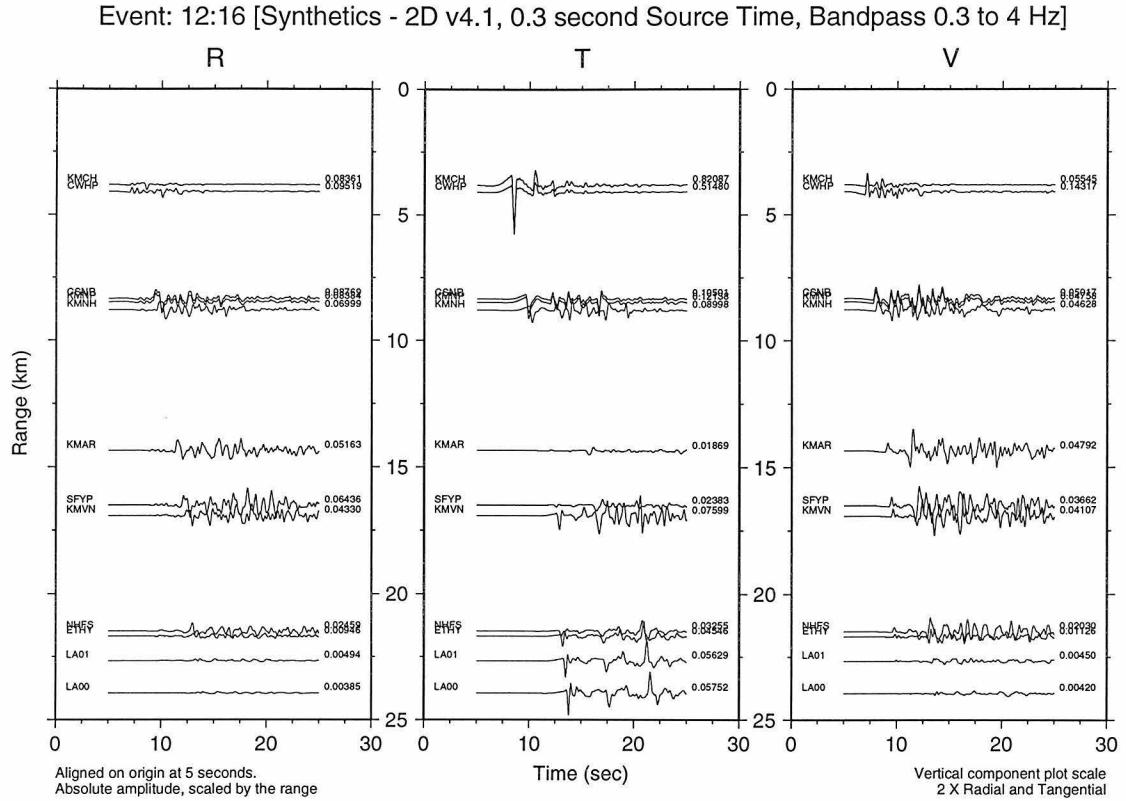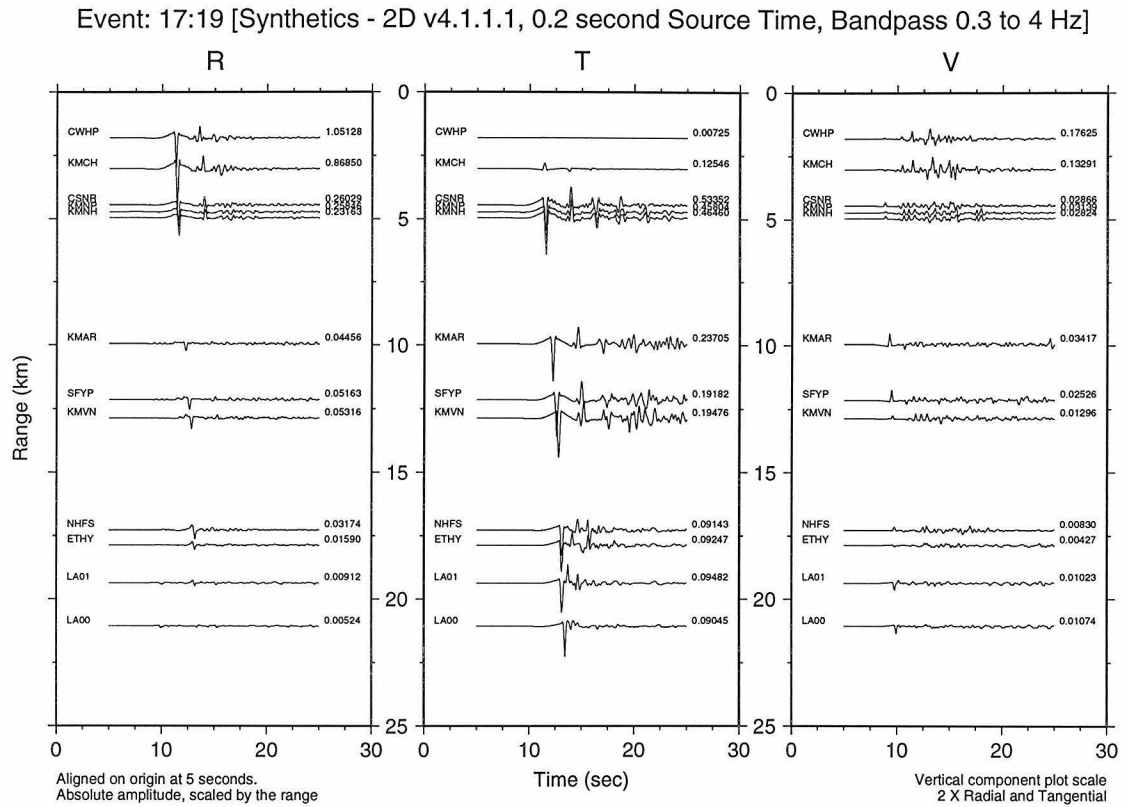

Figure 4.10: Record section of synthetic displacment waveforms for the deep event. Plotting conventions are the same as those in Figure 4.9.

with these stations because of the long-period noise at KMAR and KMVN and the emergent direct S arrival at SFYP. In the fourth station cluster, on the tangential component, the polarity of direct S seems to be flipped at ETHY. This behavior is also seen for the shallow event (compare Figures 4.2 and 4.9).

In the data for both the shallow and deep events, the amplitudes and waveforms at stations KMVN and LA01 appear anomalous. As mentioned above, the contrast of SFYP and KMVN on the tangential component of the shallow event could be explained as a source effect. However, the source mechanism doesn't explain the radial component at these stations or either of the components at station LA01. For the deep event, the source mechanism does not explain the large coda and high peak amplitudes at either KMVN or LA01. The most likely explanation is shallow site response. LA01 is in Sherman Oaks, an area which suffered significant damage in the Northridge mainshock. Hartzell *et al.* (1996), in a study of site response in the San Fernando and northern Los Angeles basins, found strong but variable site effects in Sherman Oaks. They suggest both the amplitude and variation of the effect could be explained by Quaternary deposits of the Los Angeles River. Station KMVN sits in the center of the San Fernando basin on a broad, coarse alluvial surface (Tinsley and Fumal, 1985). The surface geology doesn't immediately differentiate this site from those of surrounding stations. Unlike at LA01, the large coda at KMVN does not start immediately after the direct S arrival. Also, the ringing is lower frequency than at LA01. These factors suggest that the site response at KMVN is due to a somewhat deeper and broader structure.

Peak amplitudes of the synthetic waveforms are shown in Figure 4.11. In the first cluster of stations, the radial component amplitudes are too large for the deep event, and the tangential component amplitudes are too large for the shallow event (in fact, they are off the scale of the plot). The remainder of the amplitudes are closer fits, and the overall decay from cluster to cluster is fit well. The relative amplitudes of KMVN and LA01 to other stations in their clusters are not fit for either event. The grey symbols in Figure 4.11 show the shallow event amplitudes multiplied by the deep event data/synthetic amplitude ratio. This adjustment results in shallow event
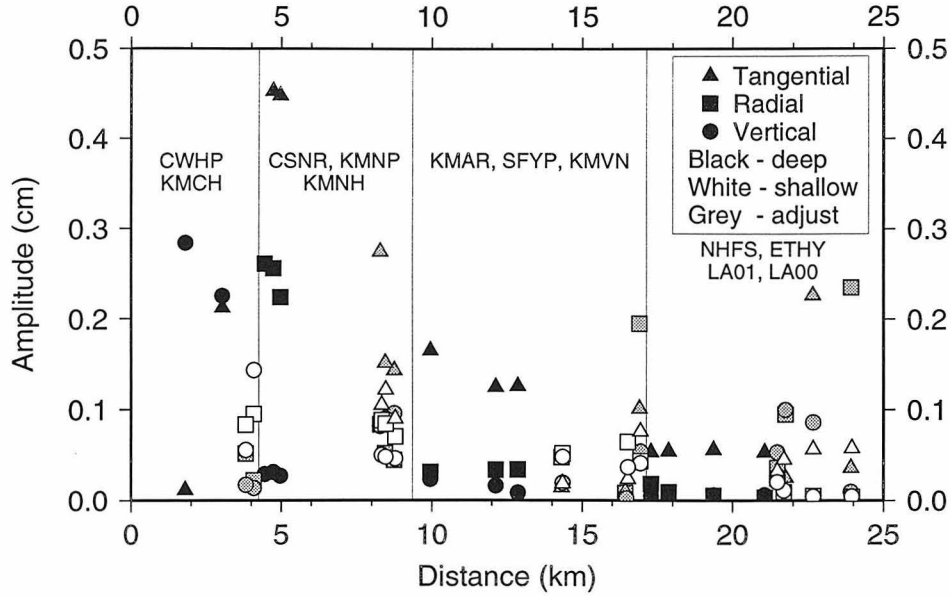
Figure 4.11: Peak amplitudes of the deep and shallow event synthetic waveforms plotted against range from the source. The symbol used are the same as used for the data (Figure 4.4) and the same normalization is applied to the deep event amplitudes. In addition, a set of adjusted amplitudes for the shallow synthetic amplitudes are shown (grey symbols) which have been multiplied by the ratio of the deep event data and synthetic amplitudes.

synthetic amplitudes for KMVN and LA01 that are similar to the data amplitudes. The propagation paths from the two events to the stations is very different, but the amplifications at KMVN and LA01 don't change. This is additional support that the anomalous amplitude of waveforms at KMVN and LA01 are the result of site effects.

4.5 Model Sensitivity

In contrast to full 3D finite difference calculations, 2D finite difference calculations can be done much more rapidly. We take advantage of this feature of 2D modeling to explore the model parameter space. Here we compare synthetic waveforms for models perturbed away from our preferred model (Figure 4.12). We show data and synthetics for the station most strongly effected by that portion of the model. In each case, the waveforms are lined up on the direct shear wave of the data and normalized to the
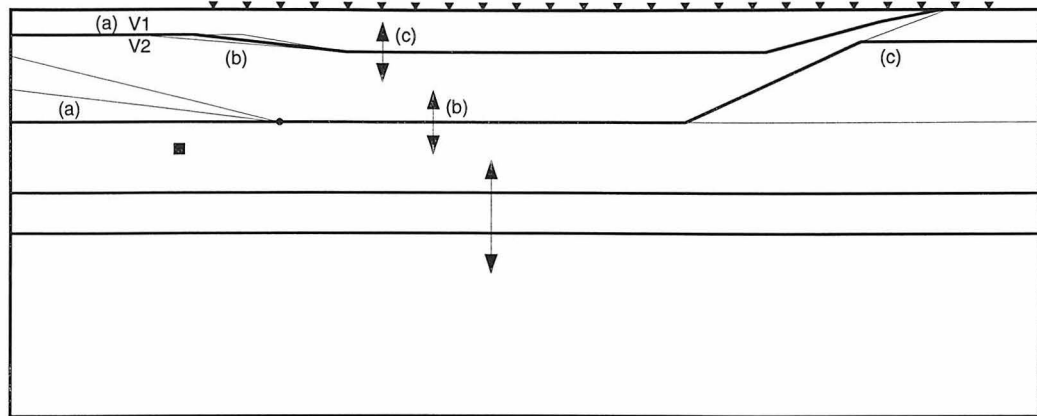
Figure 4.12: Variants of the Northridge basin velocity model for which synthetic waveforms are shown in Figures 4.13 to 4.15. Different cases marked by lowercase letters correspond to subfigures in those figures. Thin lines and arrows indicate how the model is perturbed in each case. Calculations were done for the shallow source location (black square).

same amplitude, to aid in comparison of wave shape. Only the tangential component is shown, and only waveforms from the shallow event.

The upper basin controls the surface waves 2 seconds after the direct shear wave at stations CSNR, KMNP and KMNH. The effect of changes to the velocity contrast at this interface, the point of onset of the basin edge, and the depth to the bottom of the upper basin are shown in Figure 4.13. The propagation is least strongly effected by changes to the point of onset of the basin edge (Figure 4.13b). Altering the velocity contrast across the basin and changing the depth of the basin produce similar, strong effects. The preferred model has a basin that starts at 0.5 km depth and goes down to 1 km depth (Figure 4.13c). Hence dropping the bottom by 0.4 km adds almost 50% to the basin depth, and raising the bottom by the same amount almost completely removes the basin. With a deeper basin, the energy is trapped into a nearly harmonic packet. In comparison to the data, the surface wave packet in this synthetic is a bit short in duration and high in frequency. This waveform is remarkably similar to the synthetic from the model with the original basin depth, but 15% greater velocity contrast across the interface (Figure 4.13a). Clearly a tradeoff can be found between

(a) Velocity contrast

(b) Edge onset and steepness

(c) Depth to bottom
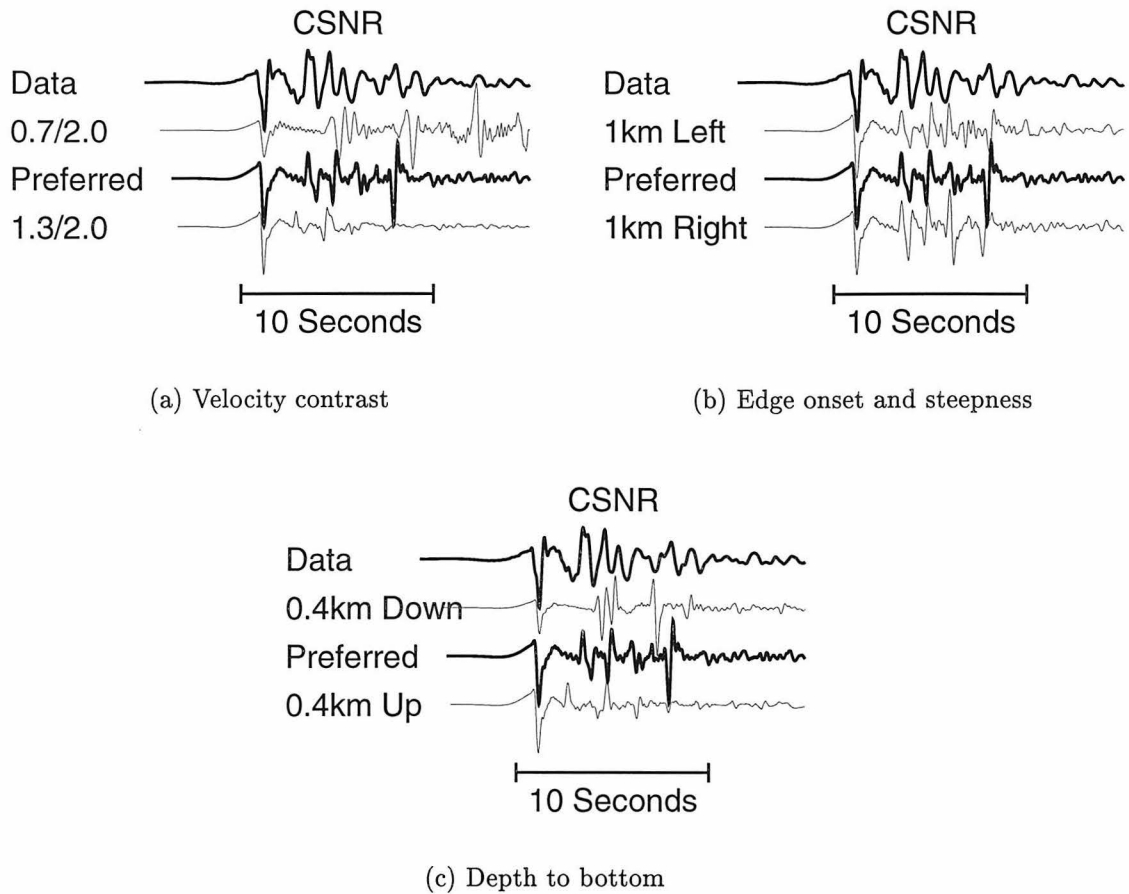
Figure 4.13: Effect on the waveform at CSNR from changes to the structure of the upper basin. Data and synthetic waveforms for the preferred model plotted with heavier lines. All traces are aligned with direct shear wave of the data and plotted the same height.

these basin parameters. Adding 3D effects due to basin curvature would also increase the range of viable models much further. The similarity of synthetics from the very shallow basin and the reduced contrast models indicate conditions in which basin phases are not trapped. The contrast of 1.3 km/s over 2.0 km/s is still fairly high, but the shallow basin structure is not tuned for critical angle reflections and basin resonance with these velocity parameters.

The second interface in the model is effectively the bottom of the lower basin. We examine the impact of variations in this structure at a station in and just beyond

(a) Edge steepness

(b) Depth to bottom

(c) Dip of trailing edge
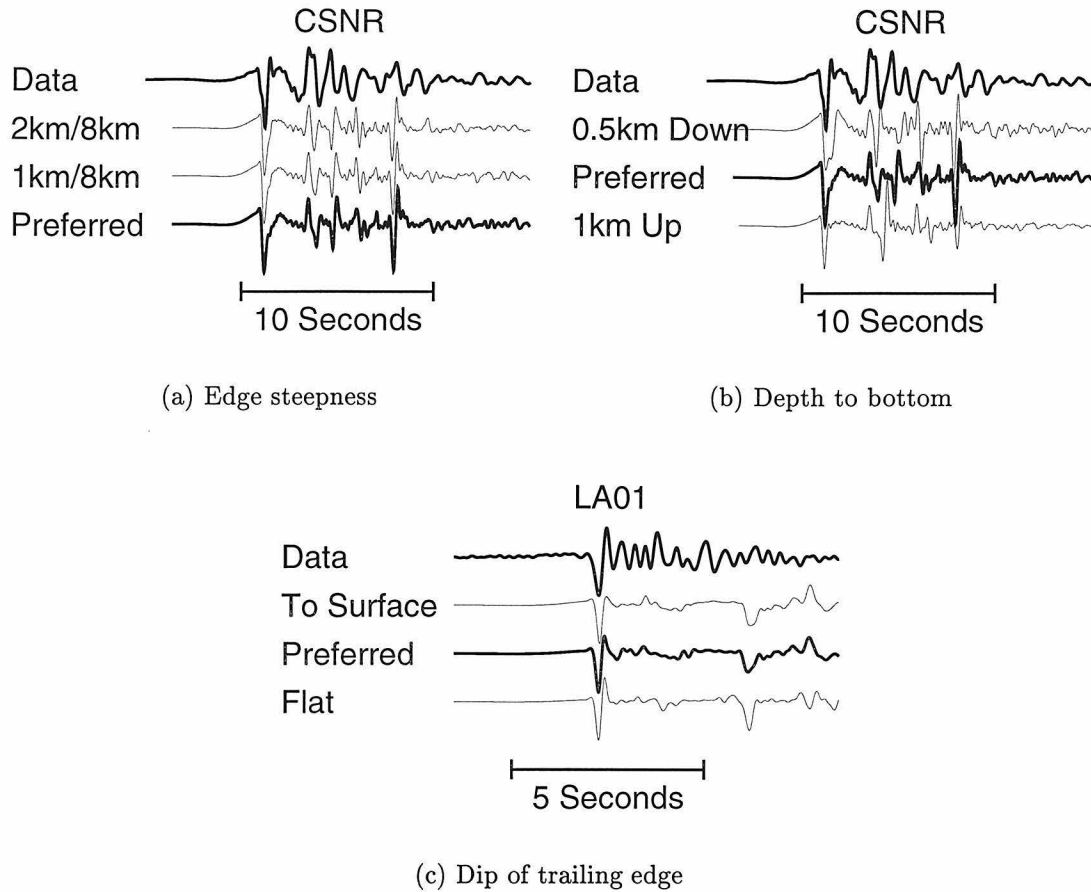
Figure 4.14: Effect on the waveform at CSNR from changes to the structure of the leading edge and center of the lower basin, and the effect on the waveform at LA01 from changes to the trailing edge of the lower basin.

the basin in Figure 4.14. In our final model the basin is flat on the leading edge and ramped up at the trailing edge. Figure 4.14a indicates the insensitivity of source-receiver geometry of this data set to the dip on the leading edge of the deep basin. The model is quite sensitive, however, to the depth of the basin relative to the source (Figure 4.14b). This interface turns energy up from the source into the leading edge of the upper basin. When the basin bottom is moved up away from the source, the amount of energy in the upper basin surface waves is reduced. Also, the duration over which energy enters the upper basin is changed.

The direct shear wave that arrives at the trailing edge of the basin leaves the source

LA01

Data

1km Up

Preferred

1km Down

|——————|
5 Seconds

Figure 4.15: Effect on the waveform at LA01 from changes to the depth of the interfaces below the source.

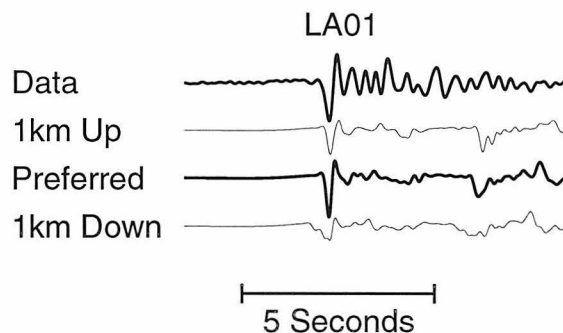as down-going energy and has to turn around the basin to arrive cleanly. The direct S arrival in the records at LA01 and LA00 is Hilbert transformed relative to stations in the basin. In our model we explain this phase shift as a triplication formed by a gradient below the source. This phase is sensitive to the structure just beyond the upper basin because arrivals from two interfaces have to arrive in synch (Figure 4.14c). In particular, the preferred and the flat interface models for the trailing basin edge introduce a phase shift to the first arrival, while the model in which the trailing edge reaches the surface does not. This indicates that a velocity gradient is needed in the Santa Monica Mountains at a few kilometers depth to turn seismic waves around the basin.

Finally, Figure 4.15 suggests the sensitivity of the Hilbert transformed phase to the depth of the interfaces that produce it. This phase should also be sensitive to the velocities across the interfaces. It depends on seismic waves turning at critical angle and reaching sites just beyond the basin. This geometry is fairly tight; the sites involved are just 20 to 25 km from the source.

4.6 Discussion

The cross-section we have modeled runs from the northwest corner of the San Fernando Valley to the southeast and into the central Santa Monica Mountains. Vidale

and Helmberger (1988) modeled data from the 1971 Sylmar earthquake over a cross-section from the northeast corner of the basin, in the 1971 epicentral region, south and west into the Los Angeles basin. Haase *et al.* (1996) and Pitarka and Irikura (1996) modeled a Northridge aftershock along a similar cross-section. These lines pass over a deeper portion of the San Fernando basin, in the northeast, than we sample with our data set. Nonetheless, it is useful to compare our model with these earlier results.

Vidale and Helmberger (1988) based their model on borehole data that constrains the depth and seismic velocities of portions of the basin (Duke *et al.*, 1971). The model has a fairly constant gradient throughout the basin from $V_s = 0.6$ km/s in the top 0.5 km to 1.8 km/s at 4 km. There is a stronger gradient at the bottom of the basin from 1.8 km/s to 3.5 km/s over less than a kilometer. The background model is from Kanamori and Hadley (1975), with $V_s = 4.0$ km/s at about 8 km. We have a similar depth of basin, but with lower contrast across it ($V_s = 2$ km/s to 3 km/s). In the mid-basin we have a stronger contrast at 1 km depth. Below the basin our model is 0.5 km/s slower from 4 to 6 kms. Our model does not include a region with 4 km/s at greater depth.

Haase *et al.* (1996) took their cross-section from a 3D tomographic model of the southern California crust. It was an earlier version of the more recently published 3D model of Hauksson and Haase (1997). The velocities in the top 0.5 km of the original tomographic model were reduced by 50% to account for the insensitivity of the tomographic model to shallow velocities. In the San Fernando basin, this results in a minimum shear velocity of about 1 km/s. The strongest gradient in the model is at about 3 km depth with the velocity rising from 2.5 km/s to 3.3 km/s. Haase *et al.* comment that this gradient may be a residual effect of the starting model in the tomographic inversion, but it is consistent with the depth of basin in our model. This gradient extends across the entire tomographic section, including the Los Angeles basin despite its greater depth. A velocity of about 3.5 km/s extends down as far as 8 km in the San Fernando basin, which seems inconsistent with the structure we need to generate the Hilbert transformed arrival beyond the basin. In the most recent tomographic model of Hauksson and Haase (1997), the depth profile in the

east Ventura basin has a strong gradient in P velocity from 4 to 6 km depth. This is more consistent with the depth of the gradient below the basin in our model.

Pitarka and Irikura (1996) patched together a basin structure similar to that in Vidale and Helmberger (1988) and a cross-section from the 3D tomography of the San Fernando basin from Zhao and Kanamori (1995) for the deeper crustal structure. We have already commented on the basin component of this model. Excluding the top 5 km of the cross-section from Zhao and Kanamori, which are replaced by Vidale and Helmberger, the model has $V_p = 5.6$ to 6.2 km/s and $V_s = 3.2$ to 3.6 km/s down to about 20 km under the San Fernando Valley. This is significantly slower than the background 1D model of Vidale and Helmberger. It is similar to velocities velocities in our model, but lacks the gradient around 5 to 6 km in our model that generates the triplication phase beyond the basin.

In addition to the models used in these 2D studies, 3D calculations for the response of the Los Angeles and San Fernando basins have been done by Olsen *et al.* (1995) and Olsen and Archuleta (1996) with a 3D model by Magistrale *et al.* (1996). Magistrale *et al.* constructed a geology-based 3D velocity model of the Los Angeles area. Their model for the San Fernando basin has since been refined. (personal communication, Magistrale, 1997). The new model has a strong upper basin gradient from $V_s = 1$ km/s to 2 km/s at about 1 km depth, but the deep basin in this model is 1 to 2 km shallower than ours. Outside the basin, shear velocities are about 3 km/s with a slight vertical gradient. The velocity jumps to 3.5 km/s at 5.5 km. This is based on the Hadley and Kanamori (1977) model for the crust in the Transverse Ranges. The depth and velocity contrast of this interface is similar to the gradient producing the triplication in our model.

The variation in background model in the three models described above is fairly large. The waveform modeling in this study indicates that data sets from shallow earthquakes at local distances may have features than can constrain this structure. Of the models discussed here, our model is most consistent with the background structure in the model of Magistrale *et al.* (1996).

The variation among the models of the basin fill structure is significant. Wald

and Graves (1997) compared data from the 1992 Landers earthquake with synthetic waveforms at periods > 2 seconds produced by three 3D models of the Los Angeles, San Fernando, and San Gabriel basins. They looked at the early version of the 3D tomographic model used by Haase *et al.* (1996), at the geology-based model of Magistrale *et al.* (1996) (which included the earlier version of their San Fernando basin model), and at the model of Graves (1996) based on seismic modeling studies. For the San Fernando basin there are significant differences in the models of the basin fill seismic velocities and the effective depth of the San Fernando basin. Of the three models, synthetics based on Graves' model fit wave shape, duration, and amplitude in the San Fernando basin markedly better than the other two. In the San Fernando basin, Graves' model has only a few layers, with a reasonably strong gradient at 0.5 to 1 km depth going from 1 km/s to 1.5-2 km/s, and a strong contrast at the bottom of the basin, which dips below 5 km depth.

Our modeling requires a strong gradient in the upper basin and a moderately deep (4 km) depth of the entire basin. The most recent Magistrale model for the San Fernando Valley and Graves' model have strong gradients in the upper basin. Our depth for the entire basin falls between the two models. However, our depth of basin is constrained primarily relative to the depth of source because it is the tendency of this interface to turn energy up toward the upper basin edge that is reflected in the data.

Hough *et al.* (1995) find large variations in Northridge aftershock waveforms from earthquakes just a few kilometers from each other. One event, about 6 km deep, has large basin-edge generated surface waves. Two others within a few kilometers of the first one, one at 2 km and the other at 10 km, have almost no basin-generated phases. This indicates a strong sensitivity of the waveforms to the source-receiver geometry. They suggest this sensitivity is due to a complex 3D basin edge structure and that near-vertical arrivals deficient in SV energy may be particularly sensitive to this structure and fail to generate Rayleigh waves effectively. However, Figure 4.16 shows the sensitivity of the response of our model to source location. Shifting the source even halfway under the basin edge removes most basin effects on the tangential
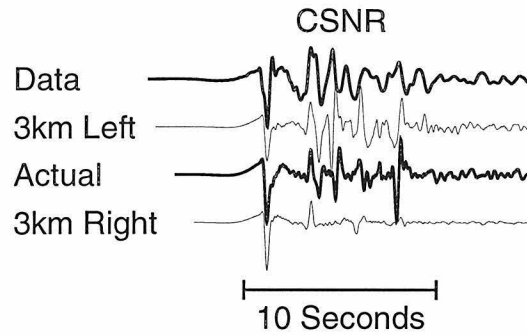
Figure 4.16: Effect on the waveform at CSNR from horizontal shifts in the source location.

component. This demonstrates that simple 2D models are sensitive to source location, and, even in the SH system, the variation can be dramatic. Also, in our study on the aftershock of the 1987 Whittier Narrows earthquake, we point out the sensitivity of basin-edge phases to the vertical radiation pattern of the source (Figure 3.13). Energy in the direct arrival and the basin-generated phases are leaving the source at different take-off angles, particularly when the source is just below the basin. Therefore the vertical radiation pattern of the source can have a significant impact. Of course, the sensitivity of the waveforms to source characteristics is potentially quite useful. Changes in source location and mechanism can illuminate different portions of the basin cross-section.

4.7   Conclusions

A strong contrast is seen in the data from the two Northridge aftershocks. The deep event is mostly insensitive to the basin. The strongest effects are near-receiver ringing and amplifications. Waveforms from the shallow event record large basin-generated surface waves with periods that are explained by strong gradients in the upper basin. The waveforms also indicate interactions of the wavefield with structure below the basin. They also show site response effects similar to those for the deep event. Array analysis of the largest basin surface waves indicate they are on-azimuth from the

source, and can be modeled with a 2D structure.

The data is fit well by a model with a slow upper basin down to 1.5 km, a deeper basin down to 3.5 km, and a gradient in the background model at 5.5 km depth. The velocity contrast between the upper and lower basins needs to be large to generate multiple cycles in the surface waves. The velocity contrast and depth of the upper basin are sensitive parameters of the upper basin, whereas the waveforms are less sensitive to the steepness of the basin edge. The location of the bottom of the deep basin, relative to the source, is an important parameter. The closer this interface is to the source, the more energy from the source is turned up into the basin. The gradient beneath the basin, at 5.5 km depth, reflects energy around the basin and introduces a $\pi/2$ phase advance to the direct arrival. In addition a gradient is needed under the Santa Monica Mountains to turn the energy sharply around the basin.

A comparison has been made with other models that have been used in 2D and 3D waveform simulations. The gradient at 5.5 km depth is also in the background model of Magistrale *et al.* (1996), and is essentially the model of Hadley and Kanamori (1977) for the central Transverse Ranges. Our basin model is bracketed by the most recent San Fernando basin model of Magistrale, and the model from Graves (1996). Both have strong gradients in the upper basin, but the depth of overall basin is shallower and deeper than ours, respectively. 2D modeling may be useful for refining 3D models of sedimentary basin, allowing us to determine points of particular sensitivity in models for a given data set.

Bibliography

Anderson, J. G., P. Bodin, J. N. Brune, J. Prince, S. K. Singh, R. Quaas, and M. Onate, Strong ground motion from the Michoacan, Mexico, earthquake, *Science*, *233*, 1043–1048, 1986.

Bard, P.-Y., and M. Bouchon, The seismic response of sediment-filled valleys: Part 1. the case of incident SH waves, *Bull. Seism. Soc. Am.*, *70*(4), 1263–1286, 1980a.

Bard, P.-Y., and M. Bouchon, The seismic response of sediment-filled valleys: Part 2. the case of incident P and SH waves, *Bull. Seism. Soc. Am.*, *70*(5), 1921–1941, 1980b.

Bent, A. L., and D. V. Helmberger, Source complexity of the October 1, 1987, Whittier Narrows earthquake, *J. Geophys. Res.*, *94*, 9548–9556, 1989.

Boore, D. M., W. B. Joyner, and T. E. Fumal, Equations for estimating horizontal response spectra and peak acceleration from western North American earthquakes: A summary of recent work, *Seism. Res. Lett.*, *68*(1), 128–153, 1997.

Campillo, M., J. C. Gariel, K. Aki, and F. J. Sánchez-Sesma, Destructive strong ground motion in Mexico City: Source, path, and site effects during great 1985 Michoacan earthquake, *Bull. Seism. Soc. Am.*, *79*, 1718–1735, 1989.

Clayton, R. W., and B. Engquist, Absorbing boundary conditions for wave-equation migration, *Geophysics*, *45*(5), 895–904, 1980.

Davis, T. L., J. Namson, and R. F. Yerkes, A cross section of the Los Angeles area: Seismically active fold and thrust belt, the 1987 Whittier Narrows earthquake, and earthquake hazard, *J. Geophys. Res.*, *94*, 9644–9664, 1989.

Devore, J. L., *Probability and Statistics for Engineering and the Sciences*, 2nd ed., Brooks/Cole, Monterey, California, 1987.

Dreger, D., and D. V. Helmberger, Source parameters of the Sierra Madre earthquake from regional and local body waves, *Geophys. Res. Lett.*, *18*, 2015–2018, 1991.

Duke, C. M., J. A. Johnson, Y. Kharraz, K. W. Campbell, and N. A. Malpiede, Subsurface site conditions and geology in the San Fernando earthquake area, *UCLA-ENG 7206*, School of Engineering, UCLA, 1971.

Edelman, A., and F. Vernon, The Northridge portable instrument aftershock data set, *Tech. rep.*, IDA, 1994, http://yin.ucsd.edu/ANZA/portable/nr_rep.html.

Frankel, A., Three-dimensional simulations of ground motions in the San Bernardino Valley, California, for hypothetical earthquakes on the San Andreas fault, *Bull. Seism. Soc. Am.*, *83*(4), 1020–1041, 1993.

Frankel, A., Dense array recordings in the San Bernardino Valley of Landers–Big Bear aftershocks: Basin surface waves, Moho reflections, and three-dimensional simulations, *Bull. Seism. Soc. Am.*, *84*(3), 613–624, 1994.

Frankel, A., and J. Vidale, A three-dimensional simulation of seismic waves in the Santa Clara Valley, California, from a Loma Prieta aftershock, *Bull. Seism. Soc. Am.*, *82*(5), 2045–2074, 1992.

Frankel, A., S. Hough, P. Friberg, and R. Busby, Observations of Loma Prieta aftershocks from a dense array in Sunnyvale, California, *Bull. Seism. Soc. Am.*, *81*(5), 1900–1922, 1991.

Graves, R. W., Modeling three-dimensional site response effects in the Marina District basin, San Francisco, California, *Bull. Seism. Soc. Am.*, *83*(4), 1020–1041, 1993.

Graves, R. W., Preliminary analysis of long-period basin response in the Los Angeles region from the 1994 Northridge earthquake, *Geophys. Res. Lett.*, *22*(2), 101–104, 1995.

Graves, R. W., Simulating seismic-wave propagation in 3D elastic media using staggered-grid finite-difference, *Bull. Seism. Soc. Am.*, *86*(4), 1091–1106, 1996.

Graves, R. W., and R. W. Clayton, Modeling path effects in three-dimensional basin structures, *Bull. Seism. Soc. Am.*, *82*, 81–103, 1992.

Haase, J. S., E. Hauksson, F. Vernon, and A. Edelman, Modeling of ground motion from a 1994 Northridge aftershock using a tomographic velocity model of the Los Angeles basin, *Bull. Seism. Soc. Am.*, *86*(1), S156–S167, 1996.

Hadley, D., and H. Kanamori, Seismic structure of the Transverse Ranges, California, *Geol. Soc. Am. Bull.*, *88*, 1469–1478, 1977.

Hartzell, S., A. Leeds, A. Frankel, and J. Michael, Site response for urban Los Angeles using aftershocks of the Northridge earthquake, *Bull. Seism. Soc. Am.*, *86*(1), S168–S192, 1996.

Hauksson, E., Earthquakes, faulting and stress in the Los Angeles basin, *J. Geophys. Res.*, *95*, 15365–15394, 1990.

Hauksson, E., and J. S. Haase, Three-dimensional V_p and V_s velocity models of the Los Angeles basin and central Transverse Ranges, California, *J. Geophys. Res.*, *102*(B3), 5423–5453, 1997.

Hauksson, E., K. Hutton, K. Kanamori, L. Jones, J. Mori, S. Hough, and G. Roquemore, Preliminary report on the 1995 Ridgecrest earthquake sequence in eastern California, *Seism. Res. Lett.*, *66*(6), 54–60, 1995a.

Hauksson, E., L. M. Jones, and K. Hutton, The 1994 Northridge earthquake sequence in California: Seismological and tectonic aspects, *J. Geophys. Res.*, *100*(B7), 12335–12355, 1995b.

Helmberger, D., R. Stead, P. Ho-Liu, and D. Dreger, Broadband modelling of regional seismograms: Imperial Valley to Pasadena, *Geophys. J. Int.*, *110*, 42–54, 1992.

Helmberger, D., D. Dreger, R. Stead, and H. Kanamori, Impact of broadband seismology on the understanding of strong motions, *Bull. Seism. Soc. Am.*, *83*, 830–850, 1993.

Helmberger, D. V., Theory and application of synthetic seismograms, in *Earthquakes: Observation, Theory and Interpretation*, edited by H. Kanamori, pp. 173–222, Soc. Italiana di Fisica, Bologna, Italy, 1983.

Helmberger, D. V., and J. E. Vidale, Modeling strong motions produced by earthquakes with two-dimensional numerical codes, *Bull. Seism. Soc. Am.*, *78*, 109–121, 1988.

Ho-Liu, P., and D. V. Helmberger, Modeling regional Love waves: Imperial Valley to Pasadena, *Bull. Seism. Soc. Am.*, *79*(4), 1194–1209, 1989.

Hough, S. E., C. Dietel, G. Glassmoyer, and E. Sembera, On the variability of aftershock ground motions in the San Fernando Valley, *Geophys. Res. Lett.*, *22*(6), 727–730, 1995.

Huang, M., *et al.*, CSMIP strong-motion records from the Sierra Madre, California earthquake of 28 June 1991, *Report OSMS 91-03*, California Strong Motion Instrumentation Program, 1991.

Kanamori, H., and D. Hadley, Crustal structure and temporal velocity change in southern California, *Pageoph*, *113*, 257–280, 1975.

Kawase, H., and K. Aki, A study on the response of a soft basin for incident S, P, and Rayleigh waves with special reference to the long duration observed in Mexico City, *Bull. Seism. Soc. Am.*, *79*, 1361–1382, 1989.

Liu, H. L., and D. V. Helmberger, The 23:19 aftershock of the 15 October 1979 Imperial Valley earthquake: More evidence for an asperity, *Bull. Seism. Soc. Am.*, *75*, 689–708, 1985.

Magistrale, H., K. McLaughlin, and S. Day, A geology-based 3D velocity model of the Los Angeles Basin sediments, *Bull. Seism. Soc. Am.*, *86*(4), 1161–1166, 1996.

Mueller, C., C. Dietel, G. Glassmoyer, T. Noce, E. Sembera, P. Spudich, and J. Watson, Digital recordings of aftershocks of the 1 October 1987 Whittier Narrows, California, earthquake, *Open File Report 88-688*, U.S. Geological Survey, 1988.

Novaro, O., T. H. Seligman, J. M. Alvarez-Tostado, J. L. Mateos, and J. Flores, Two-dimensional model for site-effect studies of microtremors in the San Fernando Valley, *Bull. Seism. Soc. Am.*, *80*, 239–251, 1990.

Olsen, K. B., and R. J. Archuleta, 3-dimensional simulation of earthquakes on the Los Angeles fault system, *Bull. Seism. Soc. Am.*, *86*(3), 575–596, 1996.

Olsen, K. B., R. J. Archuleta, and J. R. Matarese, Three-dimensional simulation of a magnitude 7.75 earthquake on the San Andreas fault, *Science*, *270*, 1628–1632, 1995.

Pitarka, A., and K. Irikura, Basin structure effects on long-period strong motions in the San Fernando Valley and the Los Angeles basin from the 1994 Northridge earthquake and an aftershock, *Bull. Seism. Soc. Am.*, *86*(1B), S126–S137, 1996.

Qu, J., T. L. Teng, and J. Wang, Modeling of short-period surface-wave propagation in southern California, *Bull. Seism. Soc. Am.*, *84*(3), 596–612, 1994.

Rial, J. A., The anomalous seismic response of the ground at the Tarzana hill site during the Northridge 1994 southern California earthquake - a resonant, sliding block, *Bull. Seism. Soc. Am.*, *86*(6), 1714–1723, 1996.

Rogers, A. M., J. C. Tinsley, and R. D. Borcherdt, Predicting relative ground response, in *Evaluating Earthauke Hazards in the Los Angeles Region– An Earth-Science Perspective*, no. U.S. Geological Survey, Professional Paper 1360, pp. 221–247, 1985.

Saikia, C. K., Estimated ground motions in Los Angeles due to $M = 7$ earthquake on the Elysian thrust fault, *Bull. Seism. Soc. Am.*, *83*, 780–810, 1993.

Saikia, C. K., Modified frequency-wavenumber algorithm for regional seismograms using Filon-quadrature method – modeling of L_g waves in eastern North America, *Geophys. J. Int.*, *118*(1), 142–158, 1994.

Sánchez-Sesma, F., S. Chavez-Perez, M. Suarez, M. A. Bravo, and L. E. Perez-Rocha, The Mexico earthquake of September 19, 1985 on the seismic response of the Valley of Mexico, *Earthquake Spectra*, *4*, 569–589, 1988.

Shakal, A. F., M. J. Huang, C. E. Ventura, D. L. Parke, T. Q. Cao, R. W. Sherburne, and R. Blazquez, CSMIP strong-motion records from the Whittier, California earthquake of 1 October 1987, *Report OSMS 87-05*, California Strong Motion Instrumentation Program, 1987.

Somerville, P. G., N. F. Smith, and R. W. Graves, The effect of critical Moho reflections on the attenuation of strong motion from 1989 Loma Prieta earthquake, in *The Loma Prieta, California, Earthquake of October 17, 1989 – Strong Ground Motion*, no. U.S. Geological Survey, Professional Paper 1551-A, pp. A67–A75, 1994.

Song, X., and D. V. Helmberger, Northridge aftershocks, a source study with TERRAscope data, submitted to BSSA.

Spudich, P., M. Hellweg, and W. H. K. Lee, Directional topographic site response at Tarzana observed in aftershocks of the 1994 Northridge, California, earthquake - implications for mainshock motions, *Bull. Seism. Soc. Am.*, *86*(1), S193–S208, 1996.

Teng, T. L., and J. Qu, Long-period ground motions and dynamic strain field of Los Angeles basin during large earthquakes, *Bull. Seism. Soc. Am.*, *86*(5), 1417–1433, 1996.

Thio, H. K., and H. Kanamori, Source complexity of the 1994 Northridge earthquake and its relation to aftershock mechanisms, *Bull. Seism. Soc. Am.*, *86*(1), S84–S92, 1996.

Tinsley, J. C., and T. E. Fumal, Mapping quaternary sedimentary deposits for areal variations in shaking response, in *Evaluating Earthquake Hazards in the Los Angeles Region– An Earth-Science Perspective*, no. U.S. Geological Survey, Professional Paper 1360, pp. 101–125, 1985.

Vidale, J., D. V. Helmberger, and R. W. Clayton, Finite-difference seismograms for SH waves, *Bull. Seism. Soc. Am.*, *75*(6), 1765–1782, 1985.

Vidale, J. E., Complex polarization analysis of particle motion, *Bull. Seism. Soc. Am.*, *76*, 1393–1405, 1986.

Vidale, J. E., Influence of focal mechanism on peak accelerations of strong motions of the Whittier Narrows, California, earthquake and an aftershock, *J. Geophys. Res.*, *94*, 9607–9613, 1989.

Vidale, J. E., and D. V. Helmberger, Elastic finite-difference modeling of the 1971 San Fernando, California earthquake, *Bull. Seism. Soc. Am.*, *78*, 122–141, 1988.

Vidale, J. E., O. Bonamassa, and H. Houston, Directional site resonances observed from the 1 October 1987 Whittier Narrows earthquake, *Earthquake Spectra*, *7*, 107–125, 1991.

Wald, D., and R. W. Graves, Modeling ground motions in the Los Angeles basins from the 1992 Landers earthquake, in preparation.

Wald, D. J., T. H. Heaton, and K. W. Hudnut, The slip history of the 1994 Northridge, California, earthquake determined from strong-motion, teleseismic, GPS, and leveling data, *Bull. Seism. Soc. Am.*, *86*(1), S49–S70, 1996.

Wen, L., and D. V. Helmberger, Propagational corrections for basin structure: Landers earthquake, *Bull. Seism. Soc. Am.*, *87*(4), 782–787, 1997.

Yerkes, R. F., T. H. McCulloh, J. E. Schoellhamer, and J. G. Vedder, Geology of the Los Angeles basin, California: an introduction, *Professional Paper 420-A*, U. S. Geological Survey, 1965.

Zhao, D., and H. Kanamori, The 1994 Northridge earthquake: 3-D crustal structure in the rupture zone and its relation to the aftershock locations and mechanisms, *Geophys. Res. Lett.*, *22*(7), 763–766, 1995.

Zhao, L., and D. V. Helmberger, Source estimation from broadband regional seismograms, *Bull. Seism. Soc. Am.*, *84*(1), 91–104, 1994.

Zhu, L., and D. V. Helmberger, Advancement in source estimation techniques using broadband regional seismograms, *Bull. Seism. Soc. Am.*, *86*(5), 1634–1641, 1996.